Probing High Energy Levels of Lanthanide Ions

Experiment and Theory

Cover photograph taken by the author

PROBING HIGH ENERGY LEVELS OF LANTHANIDE IONS

EXPERIMENT AND THEORY

METING VAN HOGE ENERGIENIVEAUS VAN LANTHANIDE IONEN
EXPERIMENT EN THEORIE

(met een samenvatting in het Nederlands)

PROEFSCHRIFT

ter verkrijging van de graad van doctor aan de Universiteit Utrecht op gezag van de Rector Magnificus, prof. dr. W. H. Gispen, ingevolge het besluit van het College voor Promoties in het openbaar te verdedigen op woensdag 8 september 2004 des middags te 14.30 uur

door

PAUL SEBASTIAAN PEIJZEL

geboren op 2 december 1976, te Ermelo

Promotor: Prof. dr. A. Meijerink

Debye Instituut
Universiteit Utrecht

Verbe égal au Très-Haut, notre unique espérance,
Jour éternel de la terre et des cieux,
De la paisible nuit nous rompons le silence,
Divin Sauveur, jette sur nous les yeux!

Répands sur nous le feu de ta grâce puissante,
Que tout l'enfer fuie au son de ta voix,
Dissipe le sommeil d'une âme languissante,
Qui la conduit à l'oubli de tes lois!

O Christ, sois favorable à ce peuple fidèle,
Pour te bénir maintenant rassemblé,
Reçois les chants qu'il offre à ta gloire immortelle,
Et de tes dons qu'il retourne comblé!

— *Jean Racine*

CIP-GEGEVENS KONINKLIJKE BIBLIOTHEEK, DEN HAAG

Peijzel, Paul Sebastiaan

Probing high energy levels of lanthanide ions – theory and experiment
(Onderzoek aan hoge energieniveaus van lanthanide ionen – theorie en experiment) /
Paul Sebastiaan Peijzel. - Utrecht: Universiteit Utrecht,
Faculteit Scheikunde, Debye Instituut.
Proefschrift Universiteit Utrecht. Met samenvatting in het Nederlands.
ISBN 90-393-3750-0

Contents

Chapter 1

Introduction

Lanthanide ions have unique properties and have been studied extensively in the past. The knowledge on the spectroscopic properties of lanthanide ions still increases. Since their discovery many pieces of the puzzle have fallen into place. The research described in this thesis fills in one of the open spaces left.

1.1 Lanthanide ions

In this thesis the spectroscopy of lanthanide ions is described. The lanthanide ions occupy a special place in the periodic table of the elements. They are situated at the bottom, one row above the actinides. The word 'lanthanide' has a Greek origin ($\lambda\alpha\nu\vartheta\alpha\nu\epsilon\iota\nu$) which means "to lie hidden". This is a very appropriate name since it took more than a century to discover all the lanthanides.

1.1.1 The discovery of the lanthanides

The first report on lanthanide ions dates from 1788. B. Geijer [1] reported the analysis of a stone found near Ytterby, Sweden. This mineral was called yttria and its composition was analyzed by Gadolin and Arrhenius [2]. It took several scientists and more than a century to discover all 15 lanthanide ions, not only in yttria, but also in ceria, a mineral found in 1803 by Klaproth [3].

Promethium is the only lanthanide that does not occur in nature in a stable form. Only radioactive isotopes are known, and promethium was made artificially in 1941 by irradiating praseodymium and neodymium with neutrons, deuterons and alpha particles [4].

At the moment of their discovery there was still the problem where to put those new elements in the periodic table of Mendeleev. All elements had about the same mass and chemical properties were nearly identical.

At the beginning of the twentieth century, when Bohr developed a new periodic table, the 15 lanthanides were placed in a separate row at the bottom of the table.

1.1.2 Properties of lanthanide ions

The trivalent state is common for all lanthanide ions. Going from La^{3+} to Lu^{3+} the 4f–shell, which is situated inside the 5s– and 5p–orbitals, is being filled from 0 to 14 electrons. Since the 4f–electrons are shielded by the 5s– and 5p–electrons they do not play a role in chemical bonding. The chemical properties of the lanthanides are therefore much alike. The $4f^0$ (empty f–shell), $4f^7$ (half–filled f–shell) and $4f^{14}$ (filled f–shell) configurations are most stable. Therefore, besides the trivalent state some ions also occur in divalent and tetravalent states. Examples are Ce^{4+} ($4f^0$), Eu^{2+} and Tb^{4+} ($4f^7$) and Yb^{2+} ($4f^{14}$).

The lanthanides are obtained industrially by treating their ores monazite and bastnästite with caustic soda and hydrochloric acid [5]. The resulting aqueous solutions of chlorides of the lanthanide ions are then subjected to column chromatography separating them according to decreasing atomic number, and the ions are eluted in the order Lu^{3+} to La^{3+}.

The purity of the isolated lanthanides depends on the length of the column used. However, it is not possible to obtain 100% pure compounds and the starting materials used to

prepare lanthanide doped compounds contain traces of neighboring ions. Spectroscopic investigation of one specific ion is often impaired by traces of other ions present.

1.1.3 Applications of rare earth ions

Three modern household applications that use lanthanide ions to generate light are the fluorescent tube, the cathode ray tube in televisions and monitors, and the plasma display panel. In these applications lanthanide ions are used to convert high–energetic radiation into visible light.

A fluorescent tube is a low pressure discharge lamp. It consists of a glass tube filled with a noble gas at a pressure of 400 Pa and 0.8 Pa of mercury [6]. When a voltage is applied over the two electrodes, a discharge is generated. Electrons collide with the mercury atoms, promoting them to an excited state. Upon return to the ground state, the mercury atoms emit radiation mainly in the ultraviolet (about 85% at 254 nm and 12% at 185 nm) and a few lines in the visible part of the spectrum. The inside of the tube is coated with a luminescing material, a so–called phosphor. These phosphors absorb the ultraviolet radiation and emit light in the visible.

In the first commercially available luminescent tubes a mixture of $MgWO_4$ (blue emission) and $(Zn,Be)_2SiO_4$:Mn^{2+} (green to red emission) was used. The combined emission of the two phosphors is perceived as white light. The beryllium is extremely toxic and therefore in 1948 the phosphors were replaced by the halophosphate $Ca_5(PO_4)_3(F,Cl)$: Sb^{3+},Mn^{2+} [7]. Sb^{3+} ions emit blue light and the Mn^{2+} ions emit orange light. In the 1970s a new generation of phosphors was developed. The so–called tricolor lamp contains three phosphors based on lanthanide ions, emitting in the red, green and blue, resulting in white light [8, 9]. These phosphors are still used nowadays and are $BaMgAl_{10}O_{17}$:Eu^{2+} (blue), $GdMgB_5O_{10}$: Ce^{3+},Tb^{3+} or $LaPO_4$:Ce^{3+},Tb^{3+} (green) and Y_2O_3:Eu^{3+} (red).

In cathode ray tubes the pixels containing a red, green or blue emitting phosphor are excited using a beam of electrons. Only the red phosphor (Y_2O_2S:Eu^{3+}) is based on lanthanide ions. For green and blue the phosphors ZnS:Cu^{+},Au,Al and ZnS:Cl^{-},Ag^{+} are used, respectively.

Plasma display panels (PDPs) are another application of lanthanide ions. Due to their flatness plasma display panels offer a good alternative for cathode ray tubes. A plasma display panel consists of a matrix of xenon discharge cells. Each cell can be addressed individually. The inside and back of each cell is coated with a phosphor. When a voltage is applied a xenon discharge occurs, generating vacuum ultraviolet (VUV) radiation of 147 nm (Xe monomer line) and 172 nm (Xe dimer band) with a ratio depending on the xenon pressure. The phosphors absorb the VUV radiation and convert it into red, green or blue light. The phosphors of fluorescent tubes show good absorption at the mercury emission wavelengths. For application in PDPs there is a need for different phosphors that have good absorption in the VUV. The blue phosphor is the same as in fluorescent

tubes, although it suffers from degradation under VUV excitation. The green phosphor Zn_2SiO_4:Mn^{2+} emits a very saturated green, but has an afterglow due to the forbidden character of the manganese emission. This becomes visible when displaying fast moving objects. Y_2O_3:Eu^{3+} has a lower absorption in the VUV and is therefore replaced by (Y,Gd)BO_3:Eu^{3+}. Unfortunately the emission of this phosphor is more to the orange, making it more difficult to display deep–red images. The phosphors that are currently being applied in mercury based luminescent tubes are less efficient upon excitation with a xenon discharge. A solution for this efficiency problem may be the use of quantum cutting phosphors, which are discussed in more detail in section 1.2.3.

1.2 Spectroscopy of lanthanides

At the beginning of the twentieth century, Becquerel performed absorption measurements of salts of lanthanide ions [10]. He observed sharp absorption lines at low temperatures. It was not until 1930 that the reason for the sharpness of these lines was discovered by Bethe, Kramers and Becquerel [11–13].

The lines were attributed to intraconfigurational $4f^n$–$4f^n$ transitions. Since the $4f^n$–orbitals are shielded by the filled 5p– and 5s–orbitals and do not participate in bonding orbitals, the 4f–electrons hardly experience interaction from electrons of the ligand atoms. The spectra of the lanthanide ions therefore show sharp lines and resemble the spectra of free ions or atoms.

A $4f^n$–$4f^n$ transition is parity forbidden. The initial and final state have the same parity, and the odd–parity electric dipole operator cannot induce a transition between these two states. However, electric dipole transitions were observed for lanthanide ions. An explanation was given by Van Vleck in 1937 [14] who showed that admixture of opposite–parity configurations like $4f^{n-1}5d$ and charge transfer states makes these transitions partially allowed. From that point onwards the history of the spectroscopy of lanthanide ions develops rapidly.

1.2.1 UV/Vis and IR spectroscopy

The energy levels of a free ion arise from interactions between the $4f^n$ electrons, like Coulomb repulsion and spin–orbit coupling. When the ion is incorporated in a crystal, the electric field of the ligand ions produce a so–called crystal field which splits the multiplets in crystal–field levels (or Stark levels, in the physics community). The pattern of the splitting is caused by the strength of the crystal field and the symmetry for the site of the lanthanide ion. Since the interaction between the $4f^n$ electrons and the crystal field is low, only a small splitting of a few hundred cm^{-1} occurs.

Taking into account the interactions between the electrons, it is possible to calculate

the free–ion levels for all lanthanide ions. Together with parameters for the crystal field splitting, an energy level diagram can be created for each $4f^n$ configuration. With the aid of optical spectroscopy, the weak $4f^n$–$4f^n$ transitions from the ground state to the various higher energy levels of the ion under investigation can be measured and compared to the calculations.

Reports by Dieke *et al.* [15, 16] and Carnall *et al.* [17] provide us with an enormous amount of spectroscopic information and energy level calculations. Dieke was the first to create a scheme with all energy levels measured so far in $LaCl_3$, which is nowadays still referred to as the 'Dieke–diagram' (see figure 1.1). Carnall and coworkers studied lanthanide ions in LaF_3, and extended this diagram up to 50 000 cm^{-1}.

At even higher energies, usually in the UV and VUV a second type of transition can be observed: a $4f^n$ to $4f^{n-1}5d$ transition. One electron is excited from the $4f^n$ orbitals to one of the 5d orbitals. In contrast to the intraconfigurational $4f^n$–$4f^n$ transitions, these transitions are parity–allowed and therefore more intense than $4f^n$–$4f^n$ transitions. Due to the interaction of the 5d–electrons with the ligand ions the bonding strength changes upon 4f–5d excitation, giving broad absorption and emission bands instead of lines.

1.2.2 VUV spectroscopy

The vacuum ultraviolet (VUV) region of the electromagnetic spectrum covers the region between 50 and 200 nm (200 000 to 50 000 cm^{-1}). Research on the VUV energy levels of lanthanide ions has been very limited until recently. Two decades ago, VUV absorption spectra were reported for Ho^{3+} [18] and Er^{3+} [19]. A few f–f transitions in the VUV were observed, but at that time no further research investigating $4f^n$–$4f^n$ transitions of other lanthanide ions was performed. One reason for this was the absence of good experimental facilities for VUV spectroscopy. Especially for studies on the parity–forbidden intraconfigurational $4f^n$–$4f^n$ transitions the use of an intense tunable source for VUV radiation like a synchrotron makes it possible to record spectra with a better resolution and signal–to–noise ratio in comparison with spectra measured using the more conventional deuterium lamp.

The stronger and parity–allowed $4f^n$–$4f^{n-1}5d$ transitions were experimentally more accessible and reports on the positions of f–d absorption bands of all lanthanides in CaF_2 by Loh [20] date from 1966. Synchrotron radiation was used to study the fine structure in the f–d absorption spectra of the trivalent lanthanides in CaF_2 by Szczurek and Schlesinger [21]

Another reason for the low number of reports on VUV spectroscopy was the absence of applications that require knowledge on VUV levels of these ions. This has changed with the need for new phosphors in for instance plasma display panels and mercury free fluorescent tubes. At the end of the 1990s Wegh *et al.* reported on the VUV spectroscopy of Gd^{3+} [22], Er^{3+} [23, 24] and Nd^{3+}, Sm^{3+}, Eu^{3+}, Dy^{3+} and Ho^{3+} ions [25]. Together

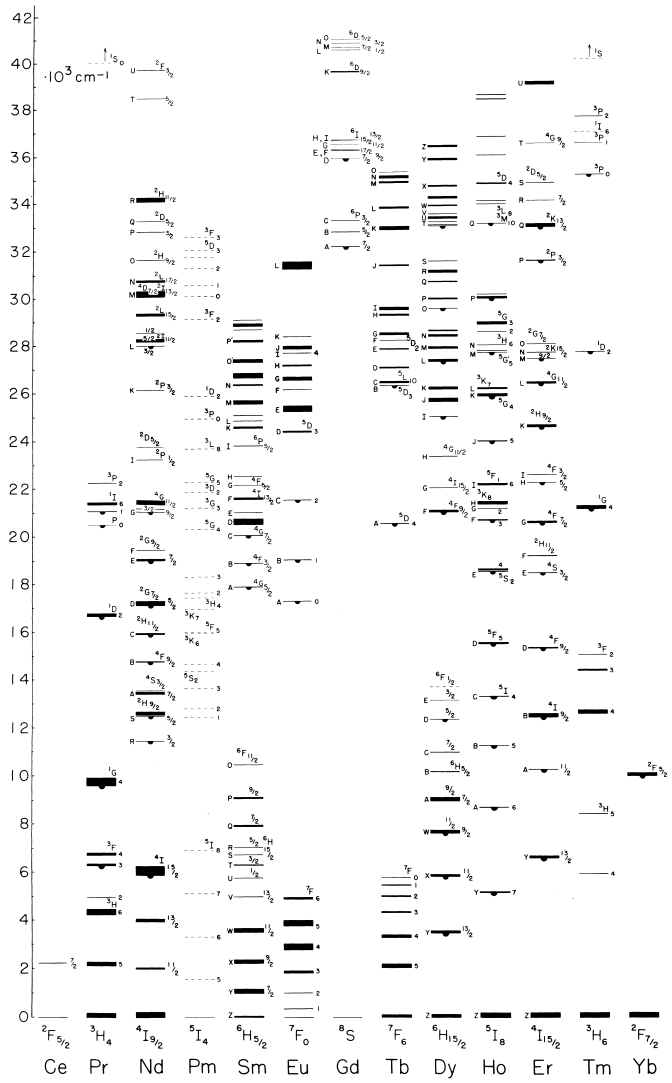

Figure 1.1: Dieke's diagram of all observed $4f^n$ energy levels for trivalent lanthanide ions in $LaCl_3$ [4]. Levels from which emission was observed are indicated by a filled semicircle.

with calculations of the VUV levels of lanthanide ions, the Dieke diagram was extended into the VUV up to about 68 000 cm^{-1} (see figure 1.2).

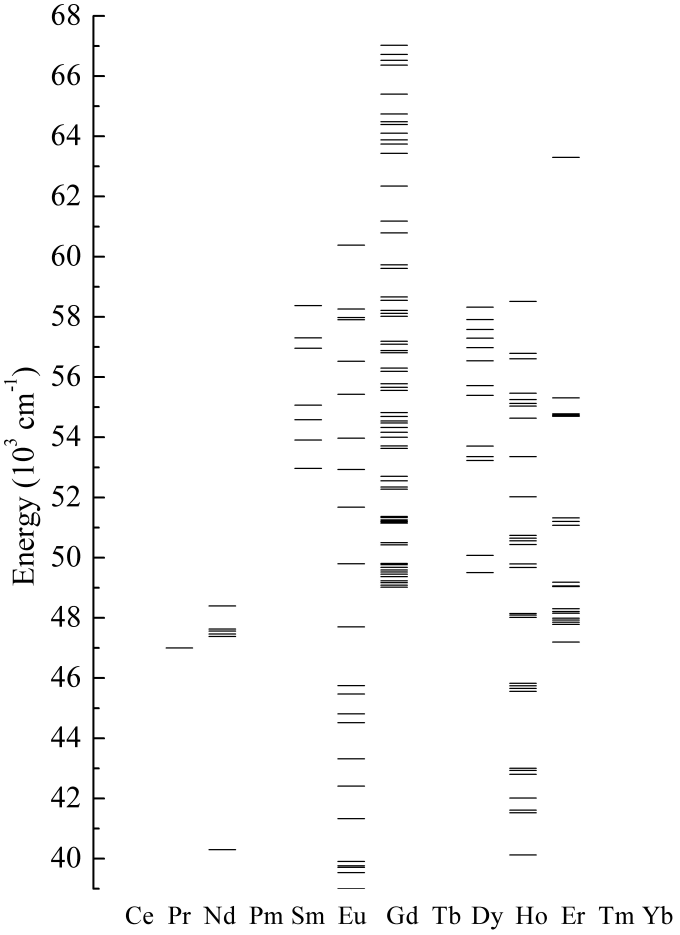

Figure 1.2: Energy level diagram of all observed $4f^n$ energy levels for trivalent lanthanide ions in the region 40 000 - 70 000 cm^{-1}.

1.2.3 Quantum cutting

An alternative for the mercury discharge is a fluorescent tube with a xenon discharge as described in section 1.1.3. From an environmental point of view the replacement of mercury by xenon is an improvement. Another advantage of the xenon discharge is that there is no startup time, since xenon is a gas at room temperature while mercury is a liquid.

The overall energy efficiency of a discharge lamp depends on the efficiency of the discharge, the (V)UV absorption of the phosphor, the energy loss involved in the conversion

of a (V)UV photon into a visible photon, and the quantum efficiency of the phosphors used.

The xenon discharge has an energy efficiency of about 65% [26], which is lower than the 75% efficiency of the mercury discharge. More importantly, converting a 254 nm photon into a visible photon gives an energy loss of about 50% while the conversion of a VUV photon of 172 nm into a visible photon corresponds to an energy loss of approximately 65%. The quantum efficiencies of the phosphors in fluorescent tubes is about 90%. In order to compete with the overall efficiency of a mercury–based fluorescent tube, the phosphors of a xenon discharge fluorescent tube should have a quantum efficiency well above 100%. This is possible, since the energy of a VUV photon is more than twice the average energy of a visible photon. The process in which one photon is absorbed and two visible photons are emitted is called quantum cutting.

One option for quantum cutting is photon cascade emission. After absorption of a (V)UV photon, one ion emits a visible photon, followed by emission of a second visible photon. This was observed for Pr^{3+} in YF_3 [27–29]. Upon VUV excitation first $^1S_0$ to $^1I_6$ emission at 407 nm occurs, followed by relaxation to the $^3P_0$ level and emission from $^3P_0$ to ^3H_J and ^3F_J levels. The quantum efficiency is about 140%, but YF_3:Pr^{3+} cannot be used for lighting applications since the $^1S_0$ emission at 407 nm lies in the violet which lowers the color rendering index [30].

The maximum quantum efficiencies for visible quantum cutting via a photon cascade have been calculated for Pr^{3+} and Tm^{3+} using Judd–Ofelt theory [31]. It was found that quantum cutting can be expected, but not with a quantum efficiency exceeding unity for useful visible wavelengths. Only the known levels up to 50 000 cm^{-1} were used in these calculations and therefore the validity of the conclusions on the maximum quantum efficiency is limited.

A second option for efficient quantum cutting is the so–called downconversion process. This process involves different lanthanide ions. By resonant (two step) energy transfer between lanthanide ions efficient quantum cutting from a high energy starting level of one of the ions can be achieved. A successful example has been described by Wegh *et al.* [32]. In $LiGdF_4$:Eu^{3+} upon VUV excitation the gadolinium ion shows cross relaxation with the europium ion, leaving both the gadolinium and europium in an excited state. The europium ion emits a visible photon. In addition energy is being transferred from the gadolinium ion to another europium ion. Next, the europium ion emits a visible photon. The estimated quantum yield that can be achieved for this system is 190%.

1.2.4 Two–photon absorption processes

The recent work on the VUV spectra of lanthanide ions using synchrotron radiation has resulted in a wealth of new information and many new energy levels were identified. However, the resolution of synchrotron measurements is not high enough to resolve the

individual crystal field levels of the VUV energy levels. Tunable lasers have been used successfully for high–resolution measurements of visible and UV levels of several lanthanides. Unfortunately, there are still no high–resolution tunable VUV lasers available nowadays. To overcome this problem, two spectroscopic techniques involving two photons can be used: two–photon excitation (TPE) and excited state absorption (ESA). The two processes are depicted in figure 1.3.

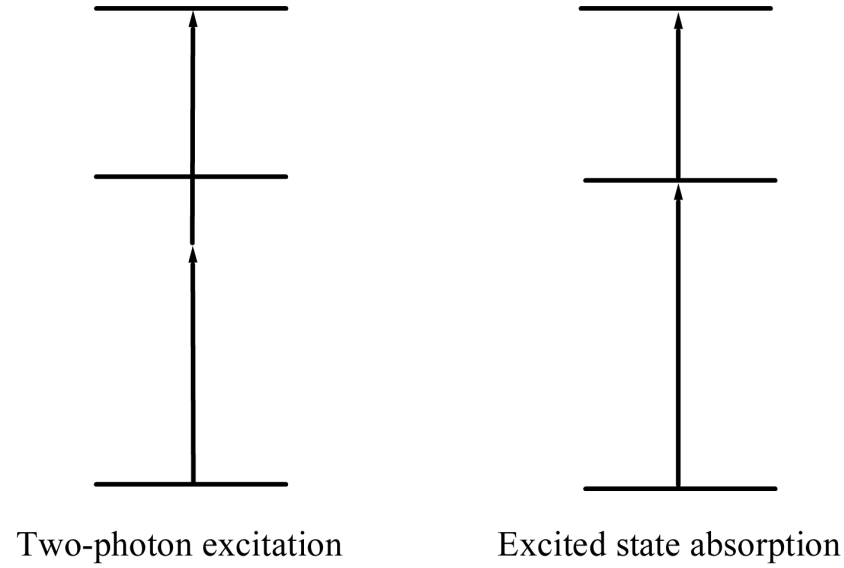

Figure 1.3: Two–photon excitation and excited state absorption.

TPE With two photon excitation two photons are absorbed simultaneously promoting an ion from the ground state to an energy level situated at the sum of the energies of the photons absorbed. This process involves a virtual intermediate state, and it was predicted in 1931 by Maria Göppert–Mayer [33]. The transition probability is about a million times lower than a 4f–4f one photon transition and the observation of two–photon excitation requires an intense light–source. Therefore it was not possible to obtain experimental confirmation of two–photon excitation processes until the invention of the laser in the early 1960s. Kaiser and Garrett were the first to demonstrate two–photon absorption for CaF_2:Eu^{2+} using a ruby laser [34].

With TPE the parity selection rule inverts, so $4f^n$–$4f^n$ transitions become parity allowed and $4f^n$–$4f^{n-1}5d$ transitions are parity–forbidden in TPE. This creates a possibility to investigate $4f^n$ levels situated at the same energy as the $4f^{n-1}5d$ bands and which are

unaccessible with one photon absorption measurements.

Since two photon excitation is much less probable than (resonant) one photon absorption, it is not possible for ions that have energy levels at the energy of one of the photons used. This is valid not only for the ion under investigation, but also the presence of impurities may hamper the observation of two photon excitation. Two–photon excitation is a nonlinear (second order) process and thus the excitation probability depends quadratically on the excitation intensity.

ESA In contrast with two–photon excitation, excited state absorption involves two consecutive transitions. First, the ion is excited to one specific excited state. Next, a second photon is absorbed, promoting the ion to an even higher excited state. The first transition is at a fixed energy, that specifically excites the ion under investigation. Therefore, impurities are less of a problem compared to two–photon excitation measurements. The second photon can be varied in energy when a tunable excitation–source like a dye–laser is used. The transition probabilities for excited state absorption are not as low as those for two photon excitation, as it is a sequence of two resonant $4f^n$–$4f^n$ transitions.

1.3 Calculations

With the availability of fast computers it is possible nowadays to calculate the energy levels of lanthanide ions with a fairly high accuracy. A parameterized Hamiltonian can be constructed, which takes into account Coulomb interactions between the $4f^n$ electrons, spin–orbit coupling and the influence of a crystal field. All possible electronic configurations are being evaluated, resulting in linear combinations of wavefunctions describing all energy levels of a $4f^n$ configuration.

Experimentally obtained values for the positions of one or more energy levels can then be used to perform a least–squares fit, where the parameter values are being varied until the best agreement with the experimental data is found [5]. When the wavefunctions of all energy levels have been constructed, it is also possible to evaluate the so–called reduced matrix elements for transitions between different multiplets in order to calculate the transition probabilities for all possible absorptions and emissions. The calculated transition probabilities can be used to simulate absorption spectra and emission spectra. An extended version of the calculations includes parameters for the 5d–electrons. This enables the calculation of $4f^n$–$4f^{n-1}5d$ absorptions and emission from the $4f^{n-1}5d$ states [35].

1.4 Summary of the thesis

This thesis deals with UV and VUV energy levels of lanthanide ions. One and two–photon techniques are used to probe these levels, and computer programs are used to calculate

the energy levels. A general overview of the discovery and luminescence properties of lanthanide ions is given in chapter 1.

In most luminescent lights, televisions screens and flat plasma display panels the light is generated using lanthanide ions. For the new developments in the field of lighting and displays, a detailed knowledge of the luminescence properties of the lanthanide ions is required. More knowledge on the positions of energy levels of these ions is essential in finding new phosphors. Especially the (vacuum) ultraviolet is a region of the electromagnetic spectrum that has gained interest in the past decades.

The energy–level structure of lanthanide ions can also be calculated using models [5]. Taking into account the various types of interactions between the electrons and the influence of a crystal field, energy levels and transition probabilities can be calculated. In chapter 2 a general description of the model for the calculation of the $4f^n$ energy–level structure is given. Using this model we calculated the complete $4f^n$ energy level scheme of all trivalent lanthanide ions, extending the Dieke diagram up to about 200 000 cm^{-1}. The impressive diagram is compared with the high energy levels that have been observed in the last decade using VUV spectroscopy. A good agreement between calculation and experiment was found. The diagram can also be used to predict future regions of interest for VUV spectroscopy of lanthanide ions.

From energy–level calculations the possibility for emission originating from the $^3P(1)_2$ level situated at about 63 000 cm^{-1} was predicted, as the energy gap to the next lower level is too large to be bridged non–radiatively. Chapter 3 describes the VUV and UV/Vis spectroscopy of the trivalent holmium ion in several fluoride host–lattices. Emission from the $^3P(1)_2$ level was indeed observed in YF_3 since the $4f^95d$ level is situated at higher energies than the $^3P(1)_2$ level in that host lattice. In $LiYF_4$ the position of the $^3P(1)_2$ level is situated above the onset of the intense $4f^95d$ absorption band and therefore emission originating from the $^3P(1)_2$ level was not observed.

The parameter values for the energy level calculations in LaF_3 are based on fits to experimentally observed energies. For most ions many of the energy levels have been measured accurately and the resulting parameter values can be used to accurately describe the energy level structure. For Gd^{3+} ions this is not the case, since the fits are based on a relatively small number of UV levels. Most energy levels of Gd^{3+} are situated in the VUV region of the electromagnetic spectrum, and only a few of the VUV energy levels are reported in literature. High–resolution measurements of the VUV levels are required to improve parameter values in order to give a better agreement in the VUV. Two–photon excitation and excited state absorption measurements on the trivalent gadolinium ion are described in chapter 4. Excited state absorption is shown to be a good method to measure the VUV energy levels with a resolution far better than with synchrotron radiation. The energy levels measured were used to improve the parameter values of the energy level calculations, and a better agreement between calculation and experiment was found in the

high–energy region of the spectrum.

The calculation model for $4f^n$ configurations can be extended to calculate $4f^{n-1}5d$ configurations [35]. Recently it was shown that the energy level structure calculated using this model can explain the fine structure in the high–resolution $4f^n \rightarrow 4f^{n-1}5d$ excitation spectra. In chapter 5 high–resolution $4f^{n-1}5d \rightarrow 4f^n$ emission spectra are reported. The spectra of Ce^{3+}, Pr^{3+}, Nd^{3+}, Er^{3+} and Tm^{3+} in $LiYF_4$ and YPO_4 are discussed and the measured emission spectra are compared to simulated emission spectra. For these calculations we refitted the parameter values for the calculation of the ground states using energies reported in the literature. The positions of the zero–phonon lines and their relative intensities as observed in the experiment are well reproduced by the calculations.

In recent years there has been a search for a sensitizer for the Gd/Eu quantum cutting couple in order to improve the absorption of VUV radiation. A good VUV sensitizer for the Gd/Eu couple is crucial for making a commercial VUV phosphor with a quantum efficiency close to 200%. Thulium shows a good absorption in the VUV and may be applied as a sensitizer for the Gd/Eu quantum cutting couple. This possibility is investigated in chapter 6. It is shown that upon $4f^{12} \rightarrow 4f^{11}5d$ excitation in the VUV the Tm^{3+} ion can be used for energy transfer to the high energy ^6G level of Gd^{3+}. Unfortunately, a cross–relaxation process between thulium and gadolinium ions was found, which is more efficient than the downconversion process of the Gd/Eu couple. Thulium can therefore not be applied as a sensitizer for Gd/Eu–based quantum cutting phosphors.

Photon cascade emission is another way of achieving a visible quantum yield over 100%. Er^{3+} has several high energy levels in the (V)UV from which a cascade emission yielding two visible photons is possible but (cascade) emission processes resulting in the emission of UV and IR photons compete with the desired cascade emission. From a qualitative analysis of previously recorded emission spectra upon VUV excitation it was concluded that it is not expected to have a visible quantum efficiency exceeding unity for Er^{3+}. In chapter 7 the transition probabilities for photon cascade emission of the erbium ion are calculated using Judd–Ofelt theory. The maximum visible quantum efficiency upon VUV excitation was determined, and it was found that there is no possibility for an efficient quantum cutting phosphor based on erbium alone. In theory a quantum efficiency in the visible above 100% is possible but the maximum visible quantum efficiency of 112% is not high enough to make the overall energy efficiency for a xenon–based luminescent tube higher than for the presently used tubes. A higher visible quantum efficiency may be achieved if the UV emission can be converted into visible light.

References

[1] B. Geijer, *Annalen für die Freunde der Naturlehre* **9** (1788), 229.

[2] A. G. Ekeberg, *Annalen für die Freunde der Naturlehre* **32** (1799), 63.

[3] A. P. Vink, *Electron-phonon coupling and pair interactions of transition metal ions.*, Thesis (2000), Chapter 1.

[4] D. R. Lide, *Handbook of Chemistry and Physics, 74^{th} edition*, CRC press: Boca Raton (1994).

[5] C. E. Housecroft and A. G. Sharpe, *Inorganic Chemistry*, Pearson Education: Harlow (2001), 627.

[6] J. Becquerel, *Phys. Z.* **8**, (1908), 632.

[7] H. G. Jenkins, A. H. McKeag and P. W. Ranby, *J. Electrochem. Soc.* **96** (1949), 1.

[8] W. A. Thornton, *J. Opt. Soc. Am.* **61** (1971), 1155.

[9] M. Koedam and J. J. Opstelten, *Light. Res. Technol.* **3**(1971), 205.

[10] J. Becquerel, *Phys. Z.* **8**, (1908), 632.

[11] H. Bethe, *Z. Physik* **60** (1930), 218.

[12] H. A. Kramers, *Proc. Acad. Sci. Amsterdam* **32** (1930), 1176.

[13] J. Becquerel, *Z. Physik* **58**, (1929), 205.

[14] J. H. van Vleck, *J. Chem. Phys.* **41** (1937), 67.

[15] G. H. Dieke and H. M. Crosswhite, *Appl. Opt.* **2** (1963), 675.

[16] G. H. Dieke, *Spectra and energy levels of rare earth ions in crystals*, Interscience Publishers, New York (1968).

[17] W. T. Carnall, G. L. Goodman, K. Rajnak and R. S. Rana, *A Systematic Analysis of the Spectra of the Lanthanides Doped into Single Crystal LaF_3* Argonne National Laboratory, Argonne Illinois (1988).

[18] A. A. Vlasenko, L. I. Devyatkova, O. N. Ivanova, V. V. Mikhailin, S. P. Chernov, T. V. Uvarova and B. P. Sobolev, *Sov. Phys. Dokl.* **30** (1985), 395.

[19] K. M. Devyatkova, O. N. Ivanova, K. B. Seiranyan, S. A. Tamazyan and S. P. Chernov, *Sov. Phys. Dokl.* **35** (1990), 40.

[20] E. Loh, *Phys. Rev.* **147** (1966), 332.

[21] T. Szczurek and M. Schlesinger, *Proceedings of the International Symposium on Rare Earth Spectroscopy*, edited by B. Jezowska-Trebiatowska, J. Legendziewicz and W. Stręk, World Scientific: Singapore (1985), 309.

[22] R. T. Wegh, H. Donker, A. Meijerink, R. J. Lamminmäki and J. Hölsä, *Phys. Rev. B* **56** (1997), 13841.

[23] R. T. Wegh, H. Donker and A. Meijerink, *Phys. Rev. B* **57** (1998), R2025.

[24] R. T. Wegh, E. V. D. van Loef, G. W. Burdick and A. Meijerink, *Molecular Physics* **101** (2003), 1047-1056.

[25] R. T. Wegh, A. Meijerink, R. J. Lamminmäki and J. Hölsä, *J. Lumin.* **87-89** (2000), 1002.

[26] F. Volkommer and L. Hitzschke (Patent-Treuhand-Gesellschaft für elektrische Glühlampen mbH), WO–A 94/23442 (1994)

[27] J. L. Sommerdijk, A. Bril and A. W. de Jager, *J. Lumin.* **8** (1974), 341.

[28] J. L. Sommerdijk, A. Bril and A. W. de Jager, *J. Lumin.* **9** (1974), 288.

[29] W. W. Piper, J. A. DeLuca and F. S. Ham, *J. Lumin.* **8** (1974), 344.

[30] T. Jüstel, H. Nikol and C. Ronda, *Angew. Chem. Int. Ed.* **37** (1998), 3084.

[31] F. Pappalardo, *J. Lumin.* **14** (1976), 159.
[32] R. T. Wegh, H. Donker, K. D. Oskam and A. Meijerink, *Science* **283** (1999), 663.
[33] M. Göppert-Mayer, *Anw. Phys.* **9** (1931), 273.
[34] W. Kaiser and C. G. B. Garrett, *Phys. Rev. Lett.* **7** (1961), 229.
[35] M. F. Reid, L. van Pieterson, R. T. Wegh and A. Meijerink, *Phys. Rev. B.* **62** (2000), 14744.

Chapter 2

A complete $4f^n$ energy–level diagram for all trivalent lanthanide ions

We describe the calculations of the $4f^n$ energy levels, reduced matrix elements for $4f^n$–$4f^n$ transitions and the simulation of absorption and emission spectra. A complete $4f^n$ energy–level diagram is calculated for all trivalent lanthanide ions in LaF_3. The calculated energy levels are compared with experimentally obtained energies. For Ce, Pr, Nd, Eu, Gd, Ho, Er, Tm and Yb many, and in some cases all, energy levels have been observed. This work provides a starting point for future investigation of as yet unobserved VUV energy levels.

2.1 Introduction

Extensive measurements of energy levels of the 4f^n configurations of lanthanide ions in various host lattices were carried out in the 1950s and 1960s. Much of this work was carried out by Dieke and co-workers and the data summarized in his 1968 book [1] (published posthumously). The energy-level diagram for trivalent lanthanide ions presented in that book is commonly referred to as a "Dieke diagram". These diagrams are useful because the energies of the J multiplets vary by only a small amount in different host crystals. The diagram allows rapid identification of the energy levels in new hosts, and has been a crucial tool in the design of materials suitable for phosphors or lasers.

As this diagram developed in the 1960s there was a fruitful interplay between measurements, theoretical models, and computational modelling of energy levels. Two– and three–body operators representing configuration interaction corrections to the Coulomb interaction were found to be necessary to accurately reproduce the observed spectra [2–4]. Anomalies in the crystal-field splitting were also noted, but the modelling of correlation effects on the crystal-field levels were not performed until the late 1970s [5, 6].

Dieke's experimental data were largely gathered using the $LaCl_3$ host. The high–symmetry (C_{3h}) sites in this crystal mean that only a small number of crystal–field parameters (four) are required to fit the spectra, which made it attractive for early studies. However, other hosts with better optical properties, especially in the UV region, were sought. The LaF_3 host lattice has the advantage of being optically transparent up into the VUV, and the chemical stability in air makes it easy to handle.

An important legacy of the work by Bill Carnall and his co–workers was a detailed study of the spectra of trivalent lanthanide ions in LaF_3. They compared the absorption spectra of all lanthanides in LaF_3 with calculated energies for C_{2v} site symmetry, which is a good approximation of the actual C_2 site [7]. For configurations with an odd number of 4f–electrons each multiplet with quantum number J splits into J+1/2 crystal field levels in any symmetry lower than cubic. In the absence of a magnetic field the energy levels are doubly degenerate due to Kramers' degeneracy. For configurations with an even number of 4f–electrons, the symmetry must be lower than D_3 in order to split up into the maximum number of $2J$+1 crystal–field levels. The LaF_3 host lattice is very suitable for comparison of calculations and measurements of energy levels as the C_2 site symmetry in LaF_3 [8] causes all multiplets to split up completely for lanthanide ions with an even number of 4f–electrons.

In 1977 Carnall, Crosswhite, and Crosswhite published the "Blue Report" [9], which, curiously, contains no date and no report number. This was an important guide to workers in the late 70s and 80s for the analysis of spectra in other hosts, and the matrix elements were used by many workers in their analysis of transition intensities.

A decade later the report by Carnall*et al.* [10] and the subsequent paper [11] provided what is arguably still the most thorough study of the energy levels of the entire series

of lanthanide ions in a host crystal. An important feature of this work was the detailed comparison between the computational modelling and the experimental data, with the analysis directed by the requirement for the Hamiltonian parameters to vary smoothly across the series. The parameters derived in that work have been widely used as starting points for analysis of other systems, and the data have been used to test extensions to the models, such as the inclusion of correlation crystal–field effects, see, for example, Li and Reid [12].

The experimental data used by Carnall and co–workers rarely extended above 40 000 cm^{-1}. Parameter values were optimized by least squares fitting of energy level calculations to experimentally obtained energies. Since the absorption spectra recorded concern the energy region up to about 40 000 cm^{-1}, calculations are expected to be less accurate in the VUV region, especially for gadolinium which has 1716 (doubly degenerate) energy levels, where the parameters were obtained by fitting to only the lowest 70 levels measured by Carnall [11]. While there was some work in the 1970 and 80s using synchrotron radiation [13, 14], and multi-photon spectra have been used to probe a few levels, it is only relatively recently that extensive, detailed, high–resolution spectra have become available. We are now in the process of extending Carnall's energy–level diagram for trivalent lanthanide ions in LaF_3 by assembling and analyzing data from synchrotron-radiation measurements [15–17], and laser techniques, including two–photon absorption and excited state absorption [18]. This chapter reports preliminary results of comparisons between calculations based on Carnall's parameters and the new experimental data. We show that the model is capable of providing a good description of the new experimental measurements, and comment on some of the technical issues involved in the calculations.

2.2 Description of the calculations

This section describes the energy level calculations using programs written by Reid and co–workers [19, 20], based on the model of Carnall [10] and Crosswhite and Crosswhite [21]. Besides energy level calculations the program also offers the possibility to calculate transition intensities and reduced matrix elements for transitions between multiplets and it is possible to simulate absorption and emission spectra. Recently Edvardsson and Åberg [22] reported the complete energy level diagram of all actinides, using a similar calculation program.

The free–ion energy level calculation uses a matrix containing all allowed electronic states for a certain $4f^n$ configuration. The matrix elements are

$$\langle \Psi_{l^n[\tau SL]J} | \mathcal{H} | \Psi_{l^{n'}[\tau' S' L']J'} \rangle,$$

where $\Psi_{l^n[\tau SL]J}$ and $\Psi_{l^{n'}[\tau' S' L']J'}$ are basis functions for the $4f^n$ configuration and $\mathcal{H}$ is the parameterized Hamiltonian. This expression is valid only for free-ion calculations,

where J is a good quantum number. $[\tau SL]$ are "nominal" identifiers for states, as τ, S and L are not good quantum numbers, where τ (sometimes designated as α) is seniority, and S and L are spin and angular momentum quantum numbers, respectively. In a crystalline lattice, the non-spherical elements of the crystal field intermix states of different J and M_J, and the only good quantum number is the group theoretical irreducible representation ("irrep") of the site symmetry, Γ and the corresponding basis functions are $\Psi_{l^n[\tau SLJM_J]\Gamma}$.

Calculation of the angular part of the matrix elements can be done exactly following the methods of Crosswhite and Crosswhite [21]. The radial parts of the matrix elements are included in the calculation parameters.

The full Hamiltonian $\mathcal{H}_{\rm full}$ has separable contributions from the "free–ion" terms and from the crystal field.

$$\mathcal{H}_{\rm full} \;=\; \mathcal{H}_{\rm free-ion} \;+\; \mathcal{H}_{\rm CF}. \tag{2.1}$$

The expression for $\mathcal{H}_{\rm free-ion}$ is:

$$\begin{aligned}\mathcal{H}_{\rm free-ion} \;=\;& E_{\rm AVG} \;+\; \sum_{k=2,4,6} F^k f_k \;+\; \zeta(4{\rm f}) A_{\rm SO} \\ &+ \alpha L(L+1) \;+\; \beta G(G_2) \;+\; \gamma G(R_7) \\ &+ \sum_{i=2,3,4,6,7,8} T^i t_i \;+\; \sum_{k=2,4,6} P^k p_k \;+\; \sum_{j=0,2,4} M^j m_j. \end{aligned} \tag{2.2}$$

The spherically symmetric part of the perturbations of the free ion and the crystal field are represented together by $E_{\rm AVG}$. The value of $E_{\rm AVG}$ shifts the energy of the entire 4f^n configuration, and represents the energy difference between the ground state energy and the configuration center of gravity (barycenter).

Coulomb repulsion between the 4f^n electrons is parameterized by F^k parameters (k=2,4,6), which are the radial electrostatic integrals. The angular part of the electrostatic interaction is represented by f_k. F^4/F^2 and F^6/F^2 ratios approximate those of the hydrogenic wavefunctions, which are 0.668 and 0.495 respectively [10]. However, in a crystalline lattice, actual parameter values may be reduced significantly from free–ion values [23].

The spin–orbit coupling is caused by interaction of the spin magnetic moment of the electron and the magnetic field originating from the movement of the electron around the nucleus. In the Hamiltonian it is described by $\zeta(4{\rm f})A_{\rm SO}$, where $A_{\rm SO}$ represents the angular part of the spin–orbit interaction and $\zeta(4{\rm f})$ is the spin–orbit coupling constant. For trivalent lanthanides in LaF_3 $\zeta(4{\rm f})$ increases from about 650 cm^{-1} for Ce^{3+} to 2930 cm^{-1} for Yb^{3+} [11].

The expression for the two–body correlation parameterized by α, β and γ is $\alpha L(L+1) \;+\; \beta G(G_2) \;+\; \gamma G(R_7)$, with L being the total orbital angular momentum and $G(G_2)$ and $G(G_7)$ are Casimir's operators for the groups G_2 and R_7, respectively [2].

For three or more electrons three–body interaction is taken into account with three–body operators t_i and parameters T^i (i = 2, 3, 4, 6, 7, 8) that were introduced by Judd [3, 4]. Hansen *et al.* [24] listed the matrix elements for three body operators t_i up to i=18, but our calculations do not extend beyond second order perturbations and thus only the elements for t_2 up to t_8 are necessary.

Spin–spin and spin–other–orbit corrections are applied in the form $M^h m_h$, where M^h (h=0, 2, 4) stands for the Marvin integrals [25] and the corresponding operator is m_i. The two-body magnetic correction is added in the form $P^k p_k$ (k=2, 4, 6).

Diagonalization of the energy matrix yields eigenvectors describing the free ion levels, and eigenvalues of the matrix are the multiplet energies. At this point, reduced matrix elements for transition intensities between J–multiplets can be calculated. These $\left(U^{(\lambda)}\right)^2$ reduced matrix elements can be used in Judd–Ofelt calculations [26] for transition intensities and branching ratios.

The crystal–field Hamiltonian is parameterized by $\mathcal{H}_{\mathrm{CF}}$ and is expressed in Wybourne notation as [27]

$$\mathcal{H}_{\mathrm{CF}} \;=\; \sum_{k,q} B_q^k C_q^{(k)}, \tag{2.3}$$

where B_q^k parameters define the radially dependent part of the one–electron crystal–field interaction, and $C_q^{(k)}$ are the many–electron spherical tensor operators for the 4f^n configuration. For 4f-electron configurations the values of k are restricted to 2, 4 and 6. The applicable values of q depend on the site symmetry of the lanthanide ion in the host lattice. For the C_{2v} effective site symmetry used for LaF_3 the restrictions are: q = even and $0 \leq q \leq k$.

The crystal field splits each multiplet into individual Stark components. Eigenvectors obtained from diagonalization of the full Hamiltonian are used to obtain dipole strengths for transitions between individual crystal field levels.

Diagonalization of the matrix containing the complete Hamiltonian yields all states of the 4f^n configuration. The gadolinium wavefunction matrix has a size of 3432 x 3432 (which can be block-diagonalized into smaller submatrices), all other energy matrices are smaller. In table 2.1 the number of electrons, SL states, SLJ multiplets and SLJM energy levels are listed for the trivalent lanthanide ions. The number of energy levels in the table does not take Kramers' degeneracy into account, as in the absence of a magnetic field all energy levels of configurations with an odd number of 4f-electrons are doubly degenerate.

With the current computer systems it is no longer necessary to perform "truncated" calculations, where only energy levels up to a certain energy are included in the calculation and the complete set of wavefunctions are not used. In order to keep the calculations manageable, Carnall *et al.* [11] used truncation for configurations where the Hamiltonian matrices were greater than 200 x 200. This truncation may not only have a significant impact upon reported wavefunctions, but also may produce shifts in the calculated energies

Table 2.1: Number of electrons, SL states, SLJ multiplets and SLJM energy levels for all trivalent lanthanide ions. Configurations with 14–n electrons (listed in parentheses) have the same number of states as configurations with n electrons.

	Ce (Yb)	Pr (Tm)	Nd (Er)	Pm (Ho)	Sm (Dy)	Eu (Tb)	Gd
n	1	2	3	4	5	6	7
SL	1	7	17	47	73	119	119
SLJ	2	13	41	107	198	295	327
SLJM	14	91	364	1001	2002	3003	3432

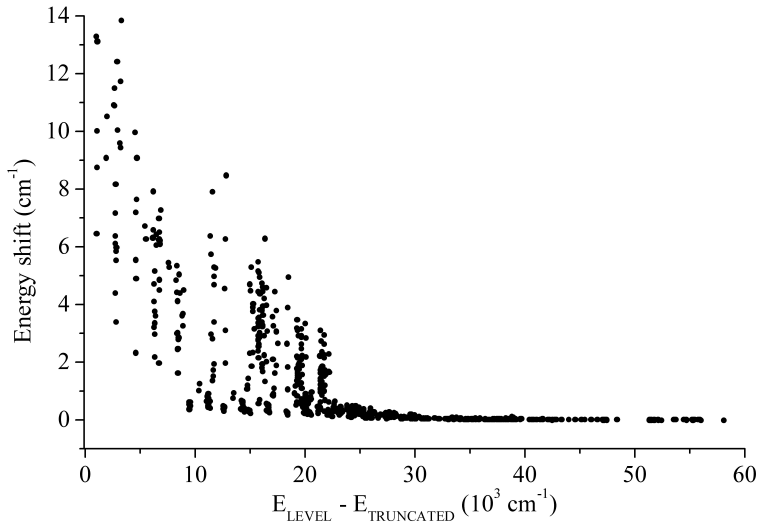

Figure 2.1: Energy shifts for energy levels up to 51 000 cm^{-1} due to truncation of the wavefunctions at different energies.

when compared to a full energy level calculation. We performed energy level calculations for the $4f^7$ energy levels of Gd^{3+} in LaF_3 up to 51 000 cm^{-1}, which is the energy range studied by Carnall *et al.* [10] using truncation at different energies. Figure 2.1 shows the energy shift for each level caused by truncation of the calculation as a function of the difference in energy between the calculated level and the truncation energy. From this figure it can be concluded that in order to have no significant effect on the calculated energies the truncation should be at least 30 000 cm^{-1} above the highest energy level of interest.

For modern computers with a high clock speed and a large amount of memory there is no longer a need for truncation when calculating the $4f^n$ levels of lanthanides. Another speed improving factor is the use of a "relatively robust" tridiagonalization routine [28], which for large matrices can result in a factor of 20 increase in speed. On our 2 GHz computer system with 1 Gbyte of 333 MHz memory the diagonalization of the 1716 x 1716 two-block matrices for gadolinium is reduced from 1100 to 63 seconds using this routine. Especially in calculations where multiple diagonalizations are used this 20-fold increase in speed is important.

If a sufficient number of experimentally obtained values for energy levels is known, a least squares fitting routine can be used to adjust some or all of the parameters to give a better agreement between calculation and experiment. Care has to be taken using this procedure to ensure that the set of parameters giving the best agreement yields physically reasonable parameter values. The standard deviation σ is used as a measure for the quality of this fit.

$$\sigma = \sqrt{\frac{\sum (E_{exp} - E_{calc})^2}{N - P}} \tag{2.4}$$

In this formula E_{exp} and E_{calc} are the experimental and calculated energies for the energy levels. N is the number of experimental levels and P is the number of parameters being varied. A parameter set giving a value of σ smaller than 20 cm^{-1} is considered to be a good fit [29].

After calculation of the crystal field levels a simulated absorption or emission spectrum may be plotted that is based on the calculated transition energies and intensities that takes into consideration the temperature and spectral linewidths. This simulated spectrum may be directly compared with experimental traces, and may help to facilitate interpretation of the experimental results.

2.3 Results and Discussion

Using the parameter values published by Carnall *et al.* [11] we calculate the complete $4f^n$ energy level diagram for all lanthanide ions in LaF_3 and compare the calculations with the recent extension of the Dieke diagram with experimentally observed energy levels up to 70 000 cm^{-1}. The highest level calculated was the $^1S(1)_0$ level of terbium at approximately 193 000 cm^{-1}. The complete $4f^n$ energy level diagram is depicted in figure 2.2.

Figure 2.3 shows the energy levels calculated in the region 39 000 up to 75 000 cm^{-1}. This is the region that is experimentally accessible using VUV spectroscopy. In this figure the calculated absorption energies of the lowest $4f^n \rightarrow 4f^{n-1}5d$ transitions in LaF_3 are indicated.

It is now well understood that for configurations with more than 7 4f–electrons there exist so–called low–spin and high–spin $4f^{n-1}5d$ states [30]. For example, the trivalent

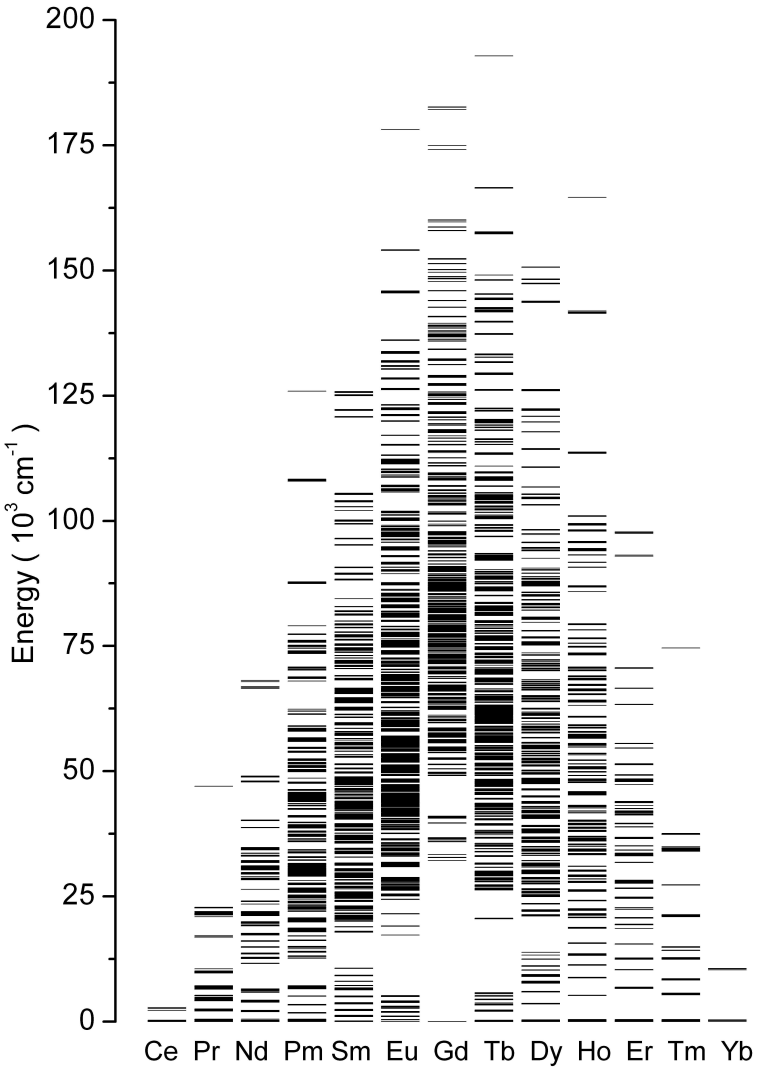

Figure 2.2: Complete 4f^n energy–level diagram for the trivalent lanthanides in LaF_3 calculated using parameters reported by Carnall [10].

terbium ion has 8 4f–electrons. When one of the 4f–electrons is promoted to a 5d–orbital, the remaining 4f^7 core has all spins parallel and the spin multiplicity is 8. There are two possibilities for the orientation of the spin of the d–electron with this 4f^7 core. In the case of a parallel spin of the d–electron, a high–spin configuration is formed, with a spin-multiplicity of 9 which is lower in energy than the low–spin configuration with

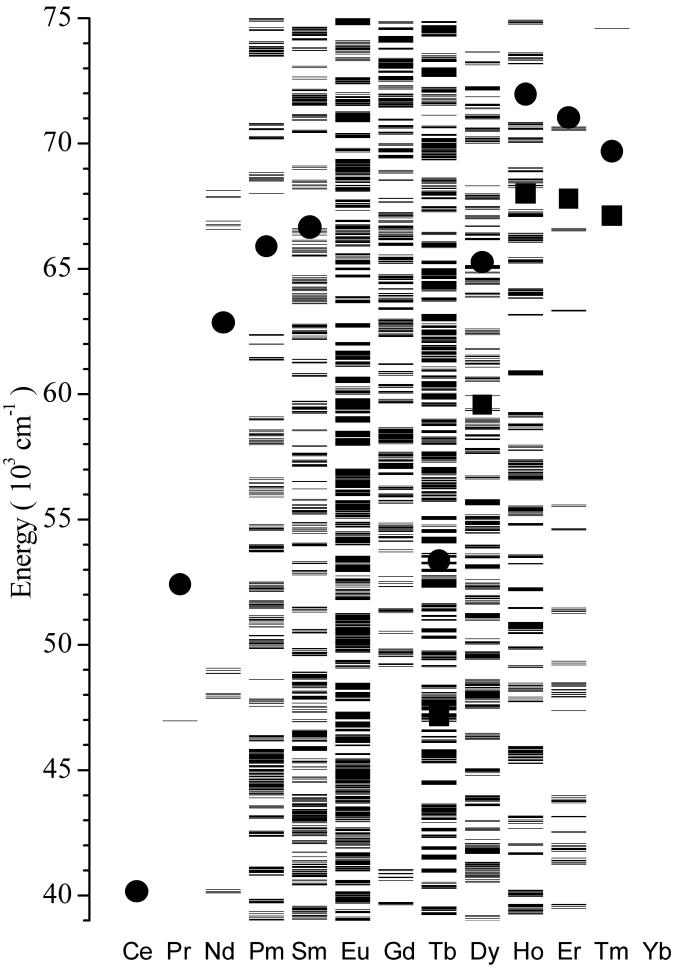

Figure 2.3: Energy–level diagram for the lanthanides in LaF_3 in the region 39 000–75 000 cm^{-1} calculated using parameters reported by Carnall [10]. The calculated lowest positions of the low–spin and high–spin $4f^{n-1}5d$ states in LaF_3 are indicated with filled circles and squares, respectively.

the spin of the d–electron opposite to the parallel 4f–electrons giving a spin multiplicity of 7. Transitions from the ground state to the low–spin state do not change the spin of the electrons, and are thus "spin–allowed" and therefore more intense than the "spin–forbidden" transitions to the high–spin states. Dorenbos [31] reviewed the position of the $4f^{n-1}5d$ states in many host–lattices and showed that the position of the first $4f^{n-1}5d$ absorption band in a host–lattice could be estimated if the position is known for one of the

lanthanide ions. In figure 2.3 the calculated positions of spin–allowed and spin–forbidden 4f^{n-1}5d absorptions for Ln^{3+} in LaF_3 are indicated with circles and squares, respectively.

Not all 4f^n–levels in figure 2.3 are expected to be observed. The first reason for this is that the relatively weak 4f^n–4f^n transitions are obscured by intense 4f^n–4f^{n-1}5d absorptions that occur in this energy region. Another reason for the fact that not all energy levels can be observed is the occurrence of transitions to energy levels with a change in J of more than six with respect to the ground state. Transitions to these states are "forbidden" and tend not to be seen. A large number of energy levels in this region have been observed using excitation with synchrotron radiation [15, 16], an overview of these energy levels is given in figure 2.4. If emission has been observed from this level this is indicated with a semicircle. Emission originating from a certain energy level can occur when the energy gap to the next lower level is more than four or five times the maximum phonon energy of the host-lattice. If the energy gap is smaller, then multi–phonon relaxation dominates and emission is no longer seen. In LaF_3 the maximum phonon energy is about 350 cm^{-1} and emission can be expected from energy levels with an energy gap of 1800 cm^{-1} or more to the next lowest level.

For Ce^{3+} [32, 33] and Pr^{3+} [34, 35] all 4f^n levels have been observed. As can be seen when comparing figure 2.3 with figure 2.4 there are a few levels of Nd^{3+} around 68 000 cm^{-1} that have not been measured as they are situated within the 4f^{2}5d absorption band. Downer *et al.* [36] successfully applied two-photon excitation to investigate the 4f^7 energy levels of Eu^{2+} in CaF_2 that are situated within the 4f^{6}5d absorption band. Since Nd^{3+} shows resonant one–photon absorption at approximately 34 000 cm^{-1}, two–photon excitation from the ground state is not probable. Two–photon absorption from an excited state of Nd^{3+} may be used to measure the position of the VUV levels. Pm^{3+} is a radioactive ion, with a lifetime of about 2.5 years. As far as we know there are no reports on the VUV energy levels of Pm^{3+}. Below the energy level calculated at 61 000 cm^{-1} there is an energy gap of more than 2000 cm^{-1} and this indicates the possibility for emission from this level in LaF_3. However, as Pm^{3+} decays to Sm^{3+} (β decay), the Sm^{3+} eventually becomes a dopant in the crystal, and we expect efficient $Pm^{3+} \rightarrow Sm^{3+}$ energy transfer to occur, quenching the Pm^{3+} emission. For Sm^{3+} some energy levels have been measured between 52 000 and 58 000 cm^{-1}, and there are many levels that still have to be measured [15]. Many of the Eu^{3+} levels in the VUV have been identified, but above 60 000 cm^{-1} a charge transfer transition hampers the observation of Eu^{3+} excitation lines.

The VUV levels of Gd^{3+} have been measured up to 68 000 cm^{-1}and most of the calculated multiplets have been observed. Recently, high–resolution excited state absorption measurements showed differences between calculated and experimental energies of up to 150 cm^{-1} for the levels probed [18]. This is not unexpected as the parameter values calculated by Carnall *et al.* [10] are based on 70 levels in the UV region of the spectrum with only a few VUV levels included in the fit. The observation of the 4f^8 levels of

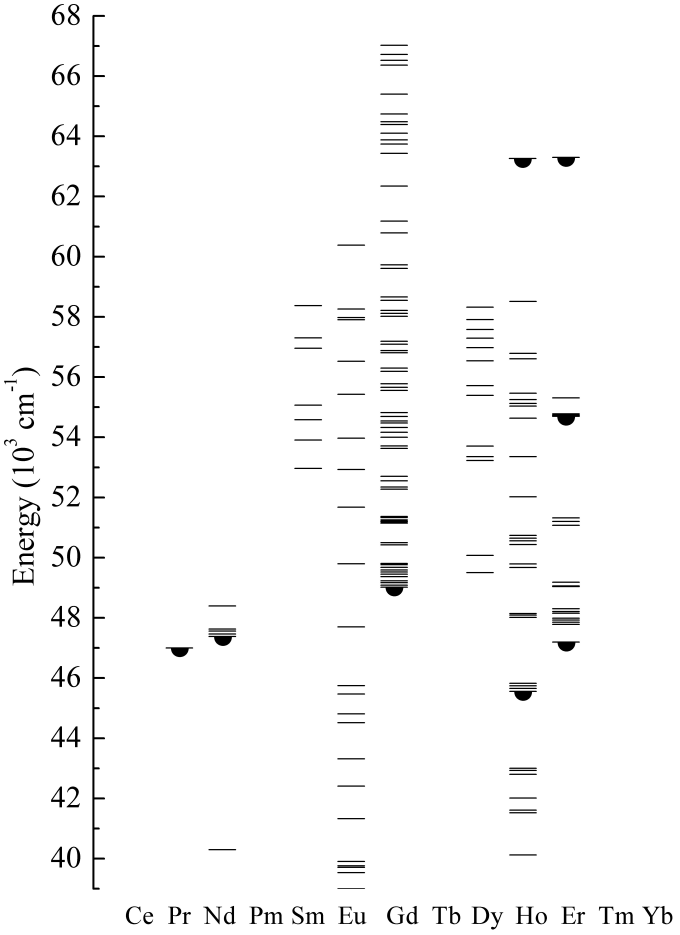

Figure 2.4: Energy–level diagram showing all experimentally observed $4f^n$ energy levels for the trivalent lanthanides in the range 39 000 – 70 000 cm^{-1}. Levels from which emission is observed are marked with a semicircle.

Tb^{3+} in the VUV region of the spectrum is not possible using one photon techniques as the $4f^75d$ bands start absorbing in the UV. We expect that two-photon excitation can be used to probe these levels, in analogy with the Eu^{2+} experiments described by Downer *et al.* [36]. Not all $4f^9$ levels of Dy^{3+} have been observed yet and for this ion the $4f^85d$ bands start to absorb at 58 000 cm^{-1}. Many of the $4f^{10}$ levels of Ho^{3+} have been measured and recently emission from the $^3P(1)_2$ level of Ho^{3+} situated at 63 000 cm^{-1} has been observed in YF_3 [17].

Nearly all energy levels of Er^{3+} have been measured. The $^2F(2)_{5/2}$ level situated at

63 000 cm^{-1} is the highest emitting level observed for Er^{3+} in LaF_3 [16]. In figure 2.3 the $^2G(2)_{7/2}$ level is situated around 66 500 cm^{-1}, just below the calculated position of the high–spin 4f–5d absorption. This position is, however, the maximum of the f–d absorption band so the onset will be at lower energy and therefore the $^2G(2)_{7/2}$ cannot be observed. Three multiplets situated at even higher energies, the $^2G(2)_{9/2}$, $^2F(1)_{5/2}$ and $^2F(1)_{7/2}$ are calculated at 70 000, 93 000 and 97 800 cm^{-1}, respectively. For Tm^{3+} the $^1S_0$ level is the only energy level that has not been observed yet. It is calculated at approximately 73 000 cm^{-1} and is situated above the onset of the 4f^{11}5d absorption bands. Finally, Yb^{3+} has no 4f–levels in the VUV.

2.4 Conclusions

The Hamiltonian parameters for trivalent lanthanide ions derived by Carnall and co–workers for the LaF_3 host are a valuable starting point for the analysis of the VUV levels of the 4f^n configurations. Advances in computer technology now allow routine calculations for complete 4f^n configurations. We have generated a complete 4fn energy–level diagram and begun the process of analyzing the available experimental data in the VUV region. Comparison of the calculated energy level scheme with experimentally obtained energies allows identification of many 4f^n levels that have been measured using synchrotron radiation, and predicts regions where high energy levels of various lanthanides that have not been observed yet may be probed by one– or two–photon spectroscopy. Using the extensive VUV data it should now be possible to further refine the parameter values.

References

[1] G. H. Dieke, *Spectra and energy levels of rare earth ions in crystals*, Interscience Publishers, New York (1968).

[2] K. Rajnak and B. G. Wybourne, *Phys. Rev.* **132** (1965), 280.

[3] B. R. Judd, *Phys. Rev.* **141** (1966), 4.

[4] H. Crosswhite, H. M. Crosswhite and B. R. Judd, *Phys. Rev.* **174** (1968), 89.

[5] B. R. Judd, *J. Chem. Phys.* **66** (1977), 3163.

[6] M. F. Reid, *J. Chem. Phys.* **87** (1987), 2875.

[7] Y. Y. Yeung and M. F. Reid, *J. Less-Common Met.* **148** (1989), 213.

[8] A. Zalkin, D. H. Templeton and T. E. Hopkins, *Inorg. Chem.* **5** (1966), 1466.

[9] W. T. Carnall, H. Crosswhite and H. M. Crosswhite, *Energy Level Structure and Transition Probabilities of the Trivalent Lanthanides in LaF$_3$*, Argonne National Laboratory, Argonne Illinois (1977).

[10] W. T. Carnall, G. L. Goodman, K. Rajnak and R. S. Rana, *A Systematic Analysis of the Spectra of the Lanthanides Doped into Single Crystal LaF_3* Argonne National Laboratory, Argonne Illinois (1988).

[11] W. T. Carnall, G. L. Goodman, K. Rajnak and R. S. Rana, *J. Chem. Phys.* **90** (1989), 3443.

[12] C. L. Li and M. F. Reid, *Phys. Rev. B* **42** (1990), 1903.

[13] L. R. Elias, W. S. Heaps and W. M. Yen, *Phys. Rev. B* **8** (1973), 4989.

[14] T. Szczurek and M. Schlesinger, *Proceedings of the International Symposium on Rare Earth Spectroscopy*, edited by B. Jezowska-Trebiatowska, J. Legendziewicz and W. Stręk, World Scientific: Singapore (1985), 309.

[15] R. T. Wegh, A. Meijerink, R. J. Lamminmäki and J. Hölsä, *J. Lumin.* **87-89** (2000), 1002.

[16] R. T. Wegh, E. V. D. van Loef, G. W. Burdick and A. Meijerink, *Mol. Phys.* **101** (2003), 1047.

[17] P. S. Peijzel, R. T. Wegh, A. Meijerink, J. Hölsä and R. J. Lamminmäki, *Optics Communications* **204** (2002), 195.

[18] P. S. Peijzel, P. Vermeulen, W. J. M. Schrama, G. W. Burdick, M. F. Reid and A. Meijerink, manuscript to be submitted to *Phys. Rev. B*.

[19] M. F. Reid and F. S. Richardson, *J. Chem. Phys.* **79** (1983), 5735.

[20] M. F. Reid and F. S. Richardson, *J. Phys. Chem.* **88** (1984), 3579.

[21] H. M. Crosswhite and H. Crosswhite, *J. Opt. Soc. Am. B* **1** (1984), 246.

[22] S. Edvardsson and D. Åberg, *Comp. Phys. Comm.* **133** (2001), 396.

[23] H. A. Weakliem, *Phys. Rev. B* **6** (1972), 2743.

[24] J. E. Hansen, B. R. Judd and H. Crosswhite, *Atomic Data and Nuclear Data Tables* **62** (1996), 1.

[25] H. H. Marvin, *Phys. Rev.* **71** (1947), 102.

[26] C. Görller-Walrand and K. Binnemans, *Handbook on the Physics and Chemistry of Rare Earths*, Elsevier, Amsterdam (1998) vol 25, p 126.

[27] B. G. Wybourne, *Spectroscopic Properties of Rare Earths*, Interscience Publishers (1965), New York.

[28] P. Bientinesi, I. S. Dhillon and R. A. van de Geijn, *UT CS Technical Report TR-03-26*, Univesity of Texas at Austin (2003), 1.

[29] C. Görller-Walrand and K. Binnemans, *Handbook on the Physics and Chemistry of Rare Earths*, Elsevier, Amsterdam (1996) vol 23 p 164.

[30] R. T. Wegh and A. Meijerink, *Phys. Rev. B* **60** (1999), 10820.

[31] P. Dorenbos, *J. Lumin.* **91** (2000), 91.

[32] R. A. Buchanan, H. E. Rast and H. H. Caspers, *J. Chem. Phys.* **44** (1966), 4063.

[33] H. Gerlinger and G. Schaak, *Phys. Rev. B* **33** (1986), 7438.

[34] C. D. Cordero-Montalvo and N. Bloembergen, *Phys. Rev. B* **30** (1984), 438; Erratum, *Phys. Rev. B.* **31** (1985), 613.

[35] C. G. Levy, T. J. Glynn and W. M. Yen, *J. Lumin.* **31/32** (1984), 245.

[36] M. C. Downer and A. Bivas, *Phys. Rev. B.* **28** (1983), 3677.

Chapter 3

High energy levels and high–energetic emissions of the trivalent holmium ion in $LiYF_4$ and YF_3

The luminescence of $LiYF_4$ and YF_3 doped with Ho^{3+} was investigated using synchrotron radiation. In the excitation spectra transitions to previously unidentified $4f^{10}$ levels were observed thus extending the energy level diagram of Ho^{3+} into the (vacuum) ultraviolet region of the electromagnetic spectrum. Some high energy emissions were observed and could be attributed to spin forbidden $4f^9 5d \rightarrow 4f^{10}$ emissions in YF_3 and $LiYF_4$. For YF_3 doped with Ho^{3+} emission from the $^3P(1)_2$ level (situated at 63000 cm^{-1}) was observed. Furthermore, several photon cascade emission processes were observed in which one VUV photon is converted into two or three UV/Vis photons, albeit with a low efficiency.

3.1 Introduction

Spectroscopy of rare–earth ions in the vacuum ultraviolet (VUV, $\lambda < 200$ nm) has recently gained interest because of the increasing number of applications requiring VUV excitation. For generating light in the visible region of the spectrum rare–earth ions are applied widely nowadays in for instance fluorescent tubes and fast scintillators [1]. For plasma displays and mercury–free luminescent tubes the VUV emission from a xenon discharge may be used. However, the phosphors that are used in fluorescent tubes nowadays are not optimized for VUV excitation. The efficiency of excitation in the VUV region is low and the phosphors suffer from degradation due to the high-energetic radiation. Therefore new types of phosphors should be developed [2, 3]. These phosphors should also have a visible quantum efficiency above unity [4]. It was shown recently that it is possible to obtain a visible quantum efficiency of about 190% with the Gd^{3+}/Eu^{3+} quantum cutting couple [5]. For the further development of quantum cutting phosphors and for the possible application of rare–earth ions as sources of UV and VUV laser radiation, the energy levels of the other lanthanide ions in the VUV region have to be known accurately.

In the last years a lot of research has been performed on the elucidation of the high energy levels of rare–earth ions. This was also stimulated when more high intensity VUV excitation sources like synchrotron radiation became available. For example for Gd^{3+} the VUV levels within the $4f^7$ configuration have been elucidated [6]. In the literature only a few publications report on high energy levels of the trivalent holmium ion. The high energy transmission spectrum of $BaHo_2F_8$ has been reported by Vlasenko *et al.* [7], but it was recorded with a rather low resolution. Still about fifteen absorption peaks in the (V)UV region of the spectrum were observed and assigned to (groups of) multiplets. In this article we report on the VUV excitation and emission spectra of Ho^{3+} in $LiYF_4$ and YF_3 extending the energy level diagram of holmium into the VUV region. In addition emission from high energy Ho^{3+} levels is reported and discussed.

3.2 Experimental

Powders of $LiYF_4$ and YF_3 doped with 1% Ho^{3+} were obtained by melting stoichiometric amounts of the fluorides with a Philips PH 1006/13 high–frequency furnace, using a modified vertical Bridgman method. The reactants were mixed in a vitreous carbon crucible. In order to remove water and air the sample was heated overnight at 450°C in a flow of ultrapure nitrogen. Subsequently the temperature was raised to 550°C and SF_6 was let into the reaction chamber for 30 minutes to remove the last traces of water and oxygen. During the rest of the synthesis a nitrogen atmosphere was maintained. Next the temperature was raised gradually until melting of the sample was observed. The melt was kept at this temperature for 30 minutes, followed by cooling down by slowly reducing the

emitted power of the high frequency generator. The sample thus obtained was a nearly oxygen–free crystal or crystalline powder and an X–ray diffraction pattern was recorded to confirm the structure and phase purity of the sample.

Low resolution excitation and emission measurements were performed on a SPEX 1680 spectrofluorometer equipped with 0.22 m double monochromators. The spectral resolution of these spectofluorometers is about 0.5 nm. For VUV/UV excitation a D_2–lamp (Hamamatsu L1835, 150W) fitted with a MgF_2 window was used. The excitation monochromator contained VUV–gratings blazed at 150 nm (1200 lines/mm) and Al mirrors coated with MgF_2. Excitation spectra were recorded in the range 140–350 nm and were corrected for lamp intensity using sodium salicylate excitation spectra as reference. To avoid absorption of VUV radiation by oxygen, the lamp housing, excitation monochromator and sample chamber were flushed with nitrogen for at least 2 hours prior to measurements. The emission monochromator was equipped with gratings blazed at 500 nm (1200 lines/mm). The signal was detected with a cooled Hamamatsu R928 photomultiplier tube, with which emission in the range of 250–800 nm could be measured. Emission spectra recorded with the R928 photomultiplier tube were corrected for the monochromator and for the detector response using correction spectra provided by the manufacturer. The sample temperature could be varied between liquid helium and room temperature. For the low temperature measurements an Oxford Instruments liquid helium flow cryostat, equipped with MgF_2 windows was used.

High resolution excitation spectra and low resolution VUV/UV/Vis emission spectra and decay times were measured at the HIGITI setup of the HASYLAB Synchrotron–strahlungslabor at DESY in Hamburg. For a detailed description of this setup, see Ref. [6]. The excitation monochromator consisted of a Wadsworth 1m monochromator with a holographic MgF_2–coated Al grating blazed at 150 nm (1200 lines/mm), providing an ultimate resolution of 0.3 Å. Excitation was possible in the range 80 – 400 nm. Low resolution VUV/UV emission measurements were carried out using a Hamamatsu 1645U–09 channelplate detector attached to a 0.4 m Seya–Namioka monochromator with a holographic MgF_2–coated grating blazed at 150 nm (1200 lines/mm). For low resolution emission measurements in the UV/Vis region two detectors were available. Emission spectra in the range of 250–1080 nm were recorded using a Tektronix CCD array attached to a monochromator with a 150 lines/mm and a 1200 lines/mm grating. Emission could also be measured in the region 300–700 nm using a cooled Hamamatsu R943–02 photomultiplier tube. The spectral resolution of both detection systems is about 1 nm. Decay times were measured using a TAC (time to amplitude converter) on a 20 ns and a 200 ns scale. The temperature of the sample could be varied between liquid helium temperature and room temperature. The pressure in the sample chamber was maintained below 10^{-8} mbar.

3.3 Results and discussion

3.3.1 $LiYF_4$:Ho^{3+}

In figure 3.1 the high–resolution excitation spectrum is presented of a $LiYF_4$:Ho^{3+} 2% single crystal while monitoring all visible emissions. Most of the lines could be attributed to transitions from the ground state to high energy 4f ^{10} levels of holmium and are listed in table 3.1.

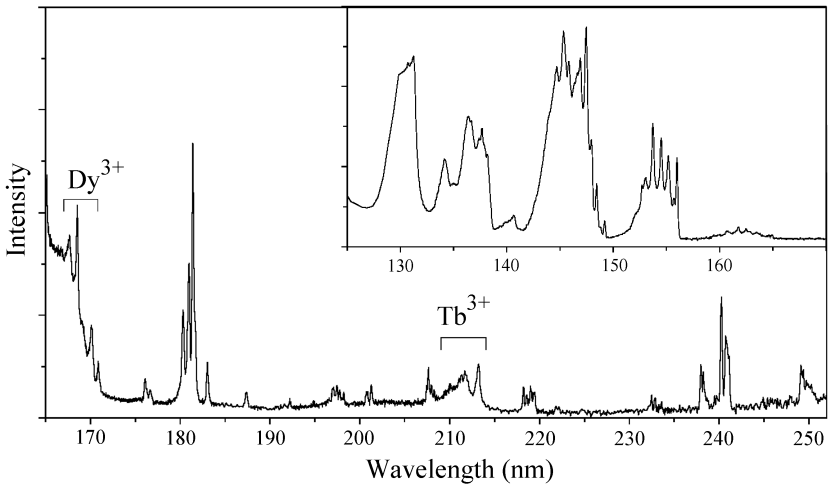

Figure 3.1: Excitation spectrum of $LiYF_4$:Ho^{3+} 2% single crystal while monitoring all visible emissions at 10 K. The inset shows the excitation spectrum of $LiYF_4$:Ho^{3+} 1% powder monitoring all visible emission at 10 K

Excitation lines due to impurities are indicated in the figure. To identify the excited states energy level calculations were performed and the assignments are included in table 3.1. The parameters used for the energy level calculations (from Ref. [8]) are given in table 3.2.

In the excitation spectrum of $LiYF_4$:Ho^{3+} about 30 sharp lines corresponding to Ho^{3+} f–f transitions can be identified. In addition spin–allowed f–d excitation bands of the impurities Tb^{3+} and Dy^{3+} are observed. The rapid increase at the short–wavelength side of the spectrum is due to the onset of the f–d absorption of Ho^{3+}. In the inset of figure 3.1 the f–d absorption region of Ho^{3+} in $LiYF_4$ is presented.

In table 3.1 the lowest and highest calculated crystal field level for each calculated multiplet, or group of multiplets in case of overlapping multiplets, is given. The $^{2S+1}\mathrm{L}_J$ terms given in table 3.1 are the ones with the largest weight content, since at high energies

Table 3.1: Experimentally observed and calculated energy levels for $LiYF_4$:Ho^{3+} in the range 40 000–63 000 cm^{-1}

λ_{exp}(nm)	E_{exp} (cm^{-1})	Multiplets	E_{calc} (cm^{-1})	No. of levels
249.2	40 128	$^5D_1$ $^5D_3$	39 924–40 202	7
240.8	41 528			
240.3	41 615	$^5D_4$ $^5D_2$	41 524–41 869	11
238.0	42 017			
		$^5D_0$	42 460	1
233.6	42 803			
232.9	42 933	$^3F(2)_3$ $^5D_1$	42 616–43 069	7
232.5	43 005			
		$^1D(3)_2$	45 166–45 196	4
219.5	45 558			
219.0	45 660	$^3M_8$ $^3H(2)_6$ $^3H(2)_4$	45 324–45 384	30
218.6	45 744			
218.2	45 825			
		$^3F(3)_3$	47 584–47 817	5
208.3	48 017			
207.9	48 093	$^3H(2)_5$	47 927–48 269	8
207.7	48 149			
		$^1D(2)_2$	48 954–49 028	4
201.3	49 677	$^1H(1)_5$	49 696–49 756	8
200.8	49 796			
198.3	50 441			
197.8	50 564	$^1K_7$ $^1G(4)_4$	50 278–50 925	18
197.4	50 648			
197.1	50 743			
		$^3G(1)_3$	51 215–51 251	5
192.2	52 026	$^3G(1)_4$	51 909–52 070	7
		$^3F(4)_2$	52 995–53 058	4
187.4	53 362	$^3H(2)_6$	53 315–53 428	10
183.0	54 636	$^3F(2)_4$	54 542–54 735	7
181.7	55 039			
181.4	55 124	$^3K(1)_8$ $^3G(1)_5$	54 957–55 317	21
181.0	55 255			
180.3	55 469			
176.7	56 609			
176.1	56 792	$^3H(3)_6$ $^1N_{10}$ $^3F(2)_3$	56 294–57 306	31
		$^3F(3)_2$	57 525–57 885	4
170.4	58 517	$^3K(1)_7$	58 435–58 716	11
		$^3K(1)_6$	58 851–59 066	10
		$^3H(3)_4$ $^3H(3)_5$	60 542–60 830	15
		$^3P(1)_2$	62 970–63 048	4

Table 3.2: Free–ion and crystal–field parameters used for the energy level calculation of $LiYF_4$:Ho^{3+} (in cm^{-1}) [8]

Parameter	Value (cm^{-1})
F^0	47 870
F^2	96 460
F^4	67 728
F^6	47 656
α	16.1
β	–529
γ	1800
T^2	400
T^3	37
T^4	107
T^6	–264
T^7	316
T^8	336
ζ	2148
B_0^2	–558
B_0^4	–710
B_4^4	942
B_0^6	23
B_4^6	–860

mixing of states occurs, especially for levels with the same J number. It is therefore not always possible to assign an absorption to one particular multiplet. The energy levels were calculated using parameters obtained from the literature. With these parameters a good agreement between the calculated and measured positions for energy levels is obtained. The presently measured new levels in the VUV may also be used to improve the parameters obtained in Ref˙ [8] which are based on fits involving a smaller number of experimental levels.

The experimentally observed levels listed in table 3.1 correspond well with the regions in which energy levels are calculated. In addition to that, in regions where energy gaps with no $4f^{10}$ levels are calculated, e.g. 43 100 – 45 100 cm^{-1}, no f–f transitions are observed.

Usually when an energy gap is less than five times the maximum phonon energy of the host lattice, non–radiative decay becomes more probable than emission from that level and no or weak emission is observed. In the case of an energy gap that cannot be bridged

by five or less phonons, emission can be observed. The maximum phonon energy of $LiYF_4$ is about 500 cm^{-1} (Li–F vibration) [9] and the energy of Y–F or Ho–F vibrations is about 400 cm^{-1}. The coupling of transitions within the $4f^n$ configuration of lanthanide ions with the Li–F vibration is relatively weak due to the larger distance, and thus for gaps of 2 000 cm^{-1} or larger emission can be expected. The energy gap between the $^1D(3)_2$ level at 45 166 cm^{-1} and $^5D_1$ at 43 069 cm^{-1} is about 2100 cm^{-1} and is thus expected to be large enough for emission from the $^1D(3)_2$ level to be observed. The energy gaps between the other levels in the region 40 000 – 60 000 cm^{-1} are significantly smaller, which makes multiphonon relaxation more probable than emission from those levels.

In figure 3.2 the emission spectra recorded upon excitation into the $4f^95d$ states are presented for $LiYF_4$:Ho^{3+}. Figure 3.2a shows the UV emission spectrum at low temperature measured at the synchrotron and figure 3.2b gives the UV/visible spectrum of $LiYF_4$:Ho^{3+} recorded at room temperature using the spectrofluorometer.

In the UV region of the spectrum transitions from the $^1D(3)_2$ level to nearly all states from $^5I_8$ to $^5F_4$ are present. In addition to that, emissions from the $^3D(1)_3$ ($\sim$33 100 cm^{-1}), $^5F_3$ ($\sim$20 600 cm^{-1}) and $^5S_2$ ($\sim$18 400 cm^{-1}) levels are observed, which is in agreement with the presence of energy gaps of 2 000 cm^{-1} or more below these levels.

Quantum cutting via the sequential emission of two visible photons starting from the $^1D(3)_2$ level is possible, but only giving a small increase in the visible quantum efficiency since the $^1D(3)_2$ emissions are very weak and the strongest lines are situated in the UV.

3.3.2 YF_3:Ho^{3+}

In $LiYF_4$ the onset of the $4f^95d$ band (60 600 cm^{-1}) is situated below the position calculated for the $^3P(1)_2$ level (62 970 cm^{-1}). The energy level calculations in table 3.1 show that the energy between the $^3P(1)_2$ level and the next lower $^3H(3)_5$ levels is over 2 000 cm^{-1}. Thus emission from the $^3P(1)_2$ level can possibly be observed for Ho^{3+} in a host lattice where the onset of the $4f^95d$ levels is situated at higher energies than the $^3P(1)_2$ level.

In figure 3.3 the excitation spectrum of YF_3:Ho^{3+} (1%) at 10 K monitoring $^3D_3 \rightarrow {}^5I_7$ emission at 357 nm is presented. In the excitation spectrum the onset of the spin forbidden and spin allowed $4f^{10} \rightarrow 4f^95d$ transitions are situated at 155 and 148 nm, respectively.

For $LiYF_4$:Ho^{3+} the onset of the spin forbidden and spin allowed $4f^{10} \rightarrow 4f^95d$ transition are reported by Wegh *et al.* [10] to be 165 and 156 nm respectively. The situation for Ho^{3+} in YF_3 and $LiYF_4$ is schematically depicted in figure 3.4.

As a result of the high energy position of the lowest $4f^95d$ band, emission from the $^3P(1)_2$ level may be observed for YF_3. The $^3P(1)_2$ level was calculated by Hölsä *et al.* [11] to be at 62 970 cm^{-1} (159 nm) and is thus situated just below the spin forbidden $4f^95d$ band in YF_3 and is overlapped by the spin forbidden $4f^95d$ band in $LiYF_4$.

In figure 3.5 the VUV/UV emission spectra of YF_3 and $LiYF_4$ doped with 1% Ho^{3+}

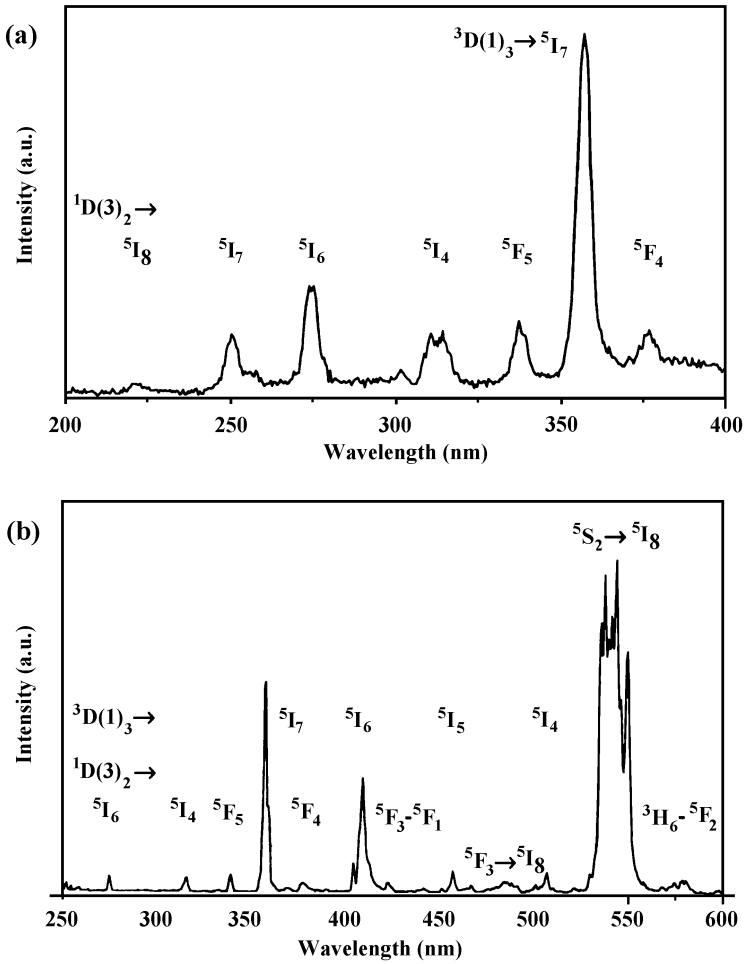

Figure 3.2: (a) UV emission spectrum of $LiYF_4$:Ho^{3+} 2% upon $^5I_8 \rightarrow 4f^9 5d$ excitation (156 nm) at 7 K. (b) UV/visible spectrum of $LiYF_4$:Ho^{3+} 2% upon $^5I_8 \rightarrow 4f^9 5d$ excitation (154 nm) at 300 K.

are shown upon $4f^9 5d$ excitation at 130 nm at 10K. Both spectra show emission peaks which originate from the $^1D(3)_2$ and $^3D(1)_3$ levels of holmium at very similar wavelengths. In addition there are several emissions marked with an arrow, which only occur in the YF_3 sample and can be attributed to emissions from the $^3P(1)_2$ level. In table 3.3 an overview of assignments is given for the emissions observed in the UV region of the spectrum.

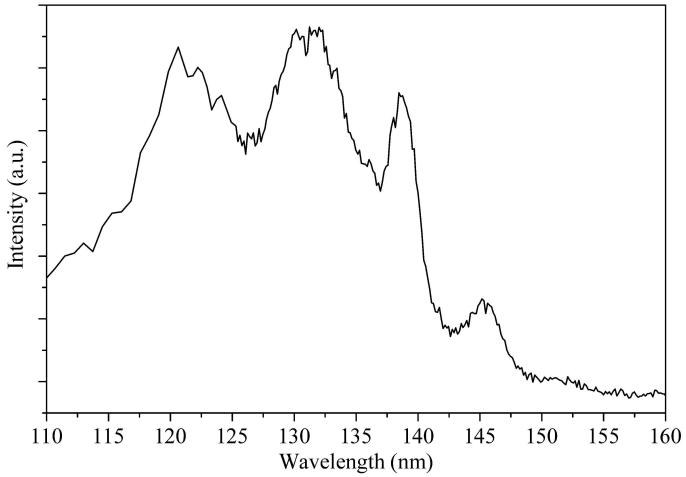

Figure 3.3: Excitation spectrum of YF_3:Ho^{3+} (1%) at 10 K monitoring $^3D_3 \rightarrow {}^5I_7$ emission at 357 nm.

Table 3.3: UV emissions of Ho^{3+} in YF_3 and $LiYF_4$ upon $4f^9$5d excitation (130 nm).

Wavelength (nm)	Energy (cm^{-1})	Assignment
210.2	47 578	$^3P_2 \rightarrow {}^5F_5$
223.5	44 743	$^1D_2 \rightarrow {}^5I_8$
239.1	41 824	$^3P_2 \rightarrow {}^3K_8$
244.4	40 917	$^3P_2 \rightarrow {}^5F_1$
251.0	39 841	$^1D_2 \rightarrow {}^5I_7$
269.4	37 120	$^3P_2 \rightarrow {}^5G_4$
274.9	36 377	$^1D_2 \rightarrow {}^5I_6$
282.2	35 436	$^3P_2 \rightarrow {}^3H_6$
302.6	33 047	$^3P_2 \rightarrow {}^3K_6$
315.0	31 746	$^1D_2 \rightarrow {}^5I_4$
332.5	30 075	$^3P_2 \rightarrow {}^3D_3$
338.6	29 533	$^1D_2 \rightarrow {}^5F_5$
357.0	28 011	$^3D_3 \rightarrow {}^5I_7$
377.0	26 525	$^1D_2 \rightarrow {}^5F_4/{}^5S_2$

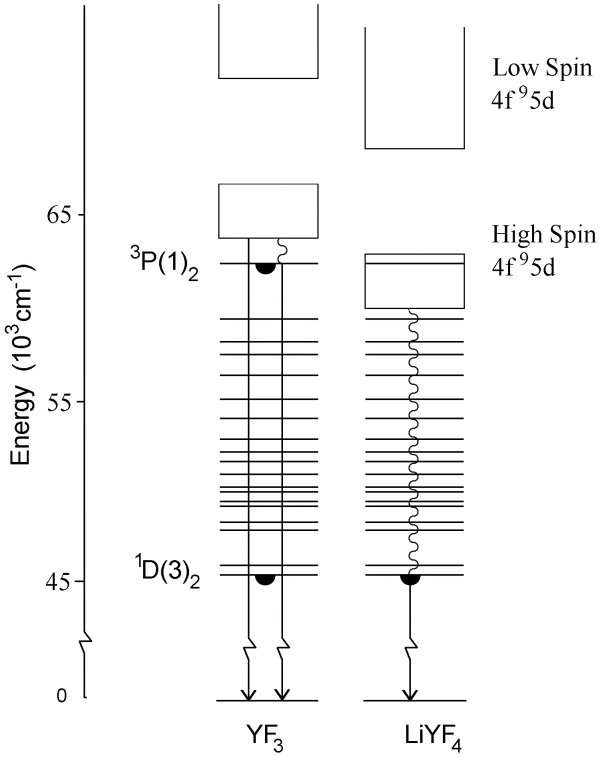

Figure 3.4: Position of the $^3P(1)_2$ level with respect to the 4f ^{9}5d band in YF_3 and $LiYF_4$ (note the break in the energy scale).

For holmium also two weak emissions in the VUV region of the spectrum were observed, at 158 nm in YF_3 and at 167 nm in $LiYF_4$ (see figure 3.5). These emissions may be attributed to spin forbidden 4f^{9}5d emissions to the ground state. For the 158 nm emission in YF_3 the decay time was measured and a decay time of 2 ns was determined. The decay curve is shown in figure 3.6. Although it is a spin forbidden transition, the decay time is short due to the fast nonradiative relaxation to the $^3P(1)_2$ level. The decay time of the 167 nm emission in $LiYF_4$ has not been measured.

3.3.3 Photon Cascade Emission

In figure 3.7 the emission spectrum upon 4f^{9}5d excitation at 10K of YF_3:Ho^{3+} in the visible part of the spectrum is shown. Assignments for the transitions are tabulated in table 3.4. For comparison see also the emission spectrum of $LiYF_4$:Ho^{3+} (figure 3.2).

The most intense emissions are those that originate from the $^3D(1)_3$ and the $^5S_2$ level.

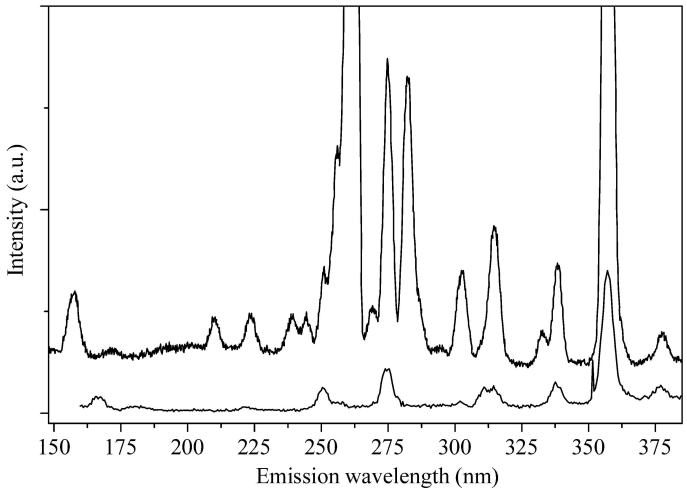

Figure 3.5: Emission spectra of YF_3 (upper trace) and $LiYF_4$ (lower trace) doped with 1% Ho^{3+} upon excitation at 130 nm at 10 K. Emissions originating from the $^3P(1)_2$ level are indicated with arrows. The off–scale peak at 260 nm is a second order peak.

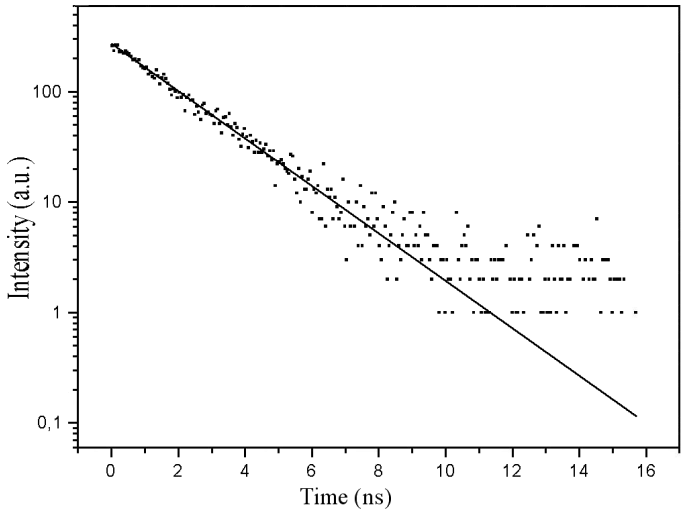

Figure 3.6: Decay curve for the 158 nm emission in YF_3 at 10 K (λ_{exc} = 130 nm).

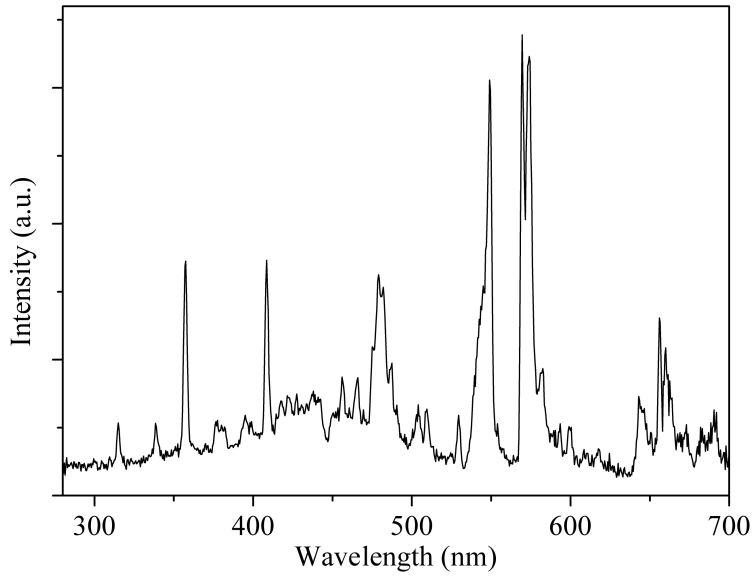

Figure 3.7: Emission spectrum of YF_3:Ho^{3+} upon $4f^9$5d excitation (130 nm) at 10K.

Combining the data from tables 3.3 and 3.4 and the emission spectra shows that photon cascade emission on holmium is possible. There is, however, no combination of two intense visible emissions possible, so only quantum cutting with a low visible quantum yield is observed. Examples of multi–photon emission processes are: $^3P(1)_2 \rightarrow {}^3D(1)_3$ (332.5 nm), followed by $^3D(1)_3$ emissions (357, 409, 456, 503, 570 nm), or $^3P(1)_2 \rightarrow {}^5G_4$ (269 nm) followed by $^5G_4$ emissions (487, 582 nm). There is even a three photon emission process converting one VUV photon into three UV/Vis photons albeit with an estimated quantum efficieny below 0.5% : First $^3P(1)_2 \rightarrow {}^3D(1)_3$ (332.5 nm), followed by $^3D(1)_3 \rightarrow {}^5F_5$ (570 nm) and finally $^5F_5 \rightarrow {}^5I_8$ (650 nm).

3.4 Conclusions

The high energy levels of the Ho^{3+} ion were calculated and measured for Ho^{3+} in $LiYF_4$ and YF_3, extending the energy level diagram into the VUV region. Some high energy emissions that have not been previously reported were observed for the trivalent holmium ion. They could be attributed to spin forbidden $4f^9$5d $\rightarrow$ 4f ^{10} emission in YF_3 and $LiYF_4$. Emissions from the $^3P(1)_2$ level (situated around 63 000 cm^{-1}) were observed in YF_3 only, where the $^3P(1)_2$ level is situated below the $4f^9$5d band onset. Furthermore, several photon cascade emission processes on the holmium ion are observed including a three step

Table 3.4: UV/Vis emissions of Ho^{3+} in YF_3 and $LiYF_4$ upon $4f^9 5d$ excitation (130 nm).

Wavelength (nm)	Transition
357.3	$^3D(1)_3 \rightarrow {}^5I_7$
376.0	$^1D(3)_2 \rightarrow {}^5F_4$
408.5	$^3D(1)_3 \rightarrow {}^5I_6$
418.0	$^1D(3)_2 \rightarrow {}^3K(2)_8$
421.6	$^5G_5 \rightarrow {}^5I_8$
455.7	$^3D(1)_3 \rightarrow {}^5I_5$
474.8	$^1D(3)_2 \rightarrow {}^5G_5$
479.0 – 485.0	$^5F_3 \rightarrow {}^5I_8$
487.3	$^5G_4 \rightarrow {}^5I_7$
502.9	$^3D(1)_3 \rightarrow {}^5I_4$
509.5	$^1D(3)_2 \rightarrow {}^5G_4$
529.5	$^5G_5 \rightarrow {}^5I_7$
539.5 – 549.5	$^5S_2 \rightarrow {}^5I_8$
569.2 – 573.7	$^3D(1)_3 \rightarrow {}^5F_5$
582.0	$^5G_4 \rightarrow {}^5I_6$
640.0 –6 66.0	$^5F_5 \rightarrow {}^5I_8$

process converting one VUV photon into two or three UV/Vis photons. The efficiency of the photon cascade emissions yielding visible photons is low and Ho^{3+} is not a good candidate for a commercial VUV phosphor with a visible quantum efficiency exceeding unity.

References

[1] P. Dorenbos, *J. Lumin.* **91** (2000), 91.

[2] G. Blasse and B. C. Grabmaier, *Luminescent Materials*, Springer Verlag, Berlin, (1994).

[3] T. Jüstel, J. C. Krupa and D. U. Wiechert, *J. Lumin.* **93** (2001), 179.

[4] H. Donker, R. T. Wegh, A. Meijerink, J. C. Krupa and M. Queffelec, *J. Soc. Information Display* **6** (1998), 73.

[5] R. T. Wegh, H. Donker, K. D. Oskam and A. Meijerink, *Science* **283** (1999), 663.

[6] R. T. Wegh, H. Donker, A. Meijerink, R. J. Lamminmäki and J. Hölsä, *Phys. Rev. B* **56** (1997), 13841.

[7] A. A. Vlasenko, L. I. Devyatkova, O. N. Ivanova, V. V. Mikhailin, S. P. Chernov, T. V. Uvarova and B. P. Sobolev, *Sov. Phys. Dokl.* **30** (1985), 395.

[8] C. K. Jayasankar, F. S. Richardson and M. F. Reid, *J. Less-Common Metals* **148** (1989), 289.

[9] S. A. Miller, H. E. Rast and H. H. Caspers, *J. Chem. Phys.* **52** (1970), 4172.

[10] R. T. Wegh and A. Meijerink, *Phys. Rev. B.* **60** (1999), 10820.

[11] J. Hölsä, University of Turku, Finland: Private communication.

Chapter 4

Probing VUV levels of Gd^{3+} in LaF_3 by two–photon spectroscopy

The energy levels of lanthanide ions have been studied in great detail in the energy range up to 40 000 cm^{-1} (250 nm). Recently an increased interest in the high energy levels between 40 000 and 70 000 cm^{-1} has emerged, partly triggered by the need for new luminescent materials for vacuum ultraviolet (VUV) excitation. Using synchrotron radiation many new energy levels have been discovered for various lanthanide ions. However, the spectral resolution of a synchrotron is limited and to resolve the complete energy level structure higher resolution tunable lasers are required. Unfortunately no high–resolution tunable lasers are available in the VUV. To overcome this problem two–photon spectroscopy may be applied. In this chapter the use of resonant and non–resonant two–photon spectroscopy is applied to measure the energy level structure of Gd^{3+} in fluorides. Non-resonant two–photon excitation and resonant excited state absorption (ESA) from the $^6P_{7/2}$ level is shown to provide high–resolution spectra of the high energy levels of Gd^{3+}. The extension of the energy level structure is used to improve energy level calculations, which is especially beneficial for Gd^{3+} where only a limited number of energy levels is available from conventional laser spectroscopy.

4.1 Introduction

In the past decades the spectroscopic properties of the trivalent gadolinium ion has been studied extensively using one-photon and two–photon excitation spectroscopy. As a result, the positions of the energy levels up to 40 000 cm^{-1} in several host-lattices are known very accurately [1–6]. The parameters required for energy level calculations are obtained by fitting the calculated levels to experimental values. This works well for the lower energy levels, but to accurately calculate the higher energy levels of gadolinium situated in the vacuum ultraviolet (VUV, $>$50 000 cm^{-1}) experimental values from that spectralregion are required.

Recently many of the VUV levels of gadolinium have been measured using synchrotron radiation [7] but the spectral resolution of these experiments is not high enough to resolve the splitting of several multiplets into all crystal field components and therefore an unambiguous assignment of measured energy levels to the calculated levels is not possible.

To obtain higher resolution spectra in the UV and VUV a laser is required, but unfortunately no high–resolution tunable VUV lasers exist at the moment. To overcome this problem, excited state absorption or two–photon excitation measurements can be used to probe the VUV levels with the high resolution required to resolve individual crystal field levels. In the case of excited state absorption, two tunable lasers are used simultaneously and the gadolinium ion is excited in two steps. The first excitation is at a fixed energy exciting the Gd^{3+} ion into the $^6P_{7/2}$ level at about 32 200 cm^{-1}, while the second tunable laser is used to excite the Gd^{3+} ion from the $^6P_{7/2}$ state to a higher energy state. Commercially available laser dyes allow excitation to levels up to approximately 62 000 cm^{-1} for the trivalent gadolinium ion.

For a high resolution measurement in the (V)UV region of the spectrum also direct two–photon excitation also can be used, where two lower energy photons from one tunable laser are absorbed simultaneously to excite into the (V)UV levels of gadolinium at twice the photon energy. The disadvantage of this technique is that it is very sensitive to impurities in the samples. The probability for resonant one-photon absorption involving an impurity ion is several orders of magnitude higher than the probability of two–photon excitation. The method of excited state absorption does not suffer from this problem since the first excitation step is very specific for the ion to be probed. In this chapter we present our results using the techniques of two–photon excitation and excited state absorption to measure high energy levels of Gd^{3+} in LaF_3. Better knowledge of these levels is used to improve calculation parameters.

4.2 Two–photon excitation

In order to measure and resolve all crystal field components within the $4f^n$ configuration of lanthanide ions an excitation source with a high spectral resolution (typically in the order of 1 cm^{-1}, the inhomogeneous linewidth) is required. Since these transitions are parity–forbidden, also a high intensity is needed. Tunable dye lasers meet these criteria and have been used since the 1970s to resolve the energy level structure of lanthanide ions in the near–infrared, visible and ultraviolet in a wide variety of crystals. Unfortunately there are no high–resolution tunable lasers in the VUV yet, so one photon absorption is not an option to measure the high $4f^n$ energy levels of lanthanide ions. Synchrotrons do provide a high intensity and tunable VUV excitation source, but the resolution of a typical 1 m monochromator is about 0.3 Å which is not enough to resolve all crystal field levels. Nevertheless, the highest resolution excitation spectra in the VUV have been recorded using synchrotron radiation [7–10].

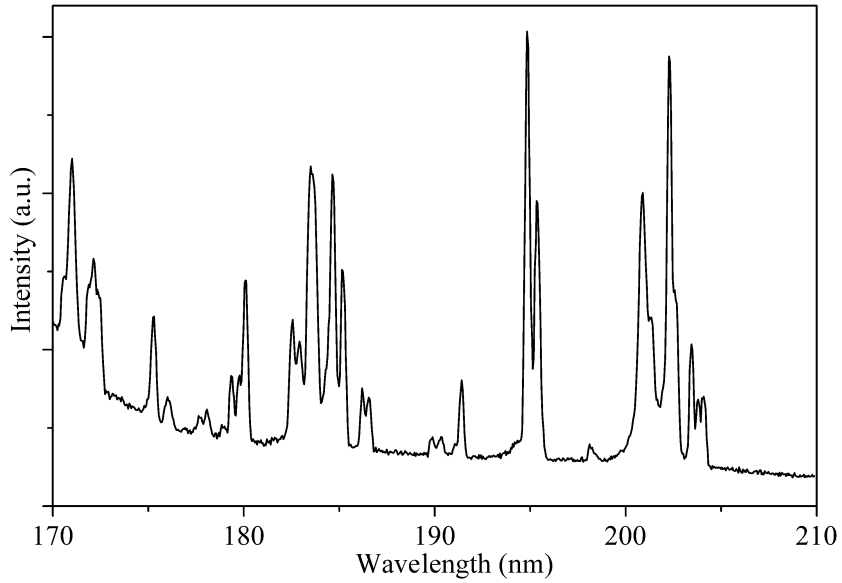

Figure 4.1: Excitation spectrum measured at the synchrotron for $LiYF_4$:Gd^{3+} (5%) at 7 K monitoring $^6P_{7/2}$ emission at 311 nm.

As an example figure 4.1 shows the excitation spectrum for $LiYF_4$:Gd^{3+} (5%) recorded at the DESY-synchrotron [7]. Many lines are observed, but it is impossible to resolve all crystal field levels. Especially in areas where different multiplets have a strong overlap (e.g. between 170 and 175 nm) it is impossible to resolve individual crystal field compo-

nents.

Two–photon excitation overcomes the problem of availability of VUV lasers, since only photons of half the energy are needed using this technique. To probe the energy levels in the VUV, high resolution tunable lasers with wavelengths between 400 and ∼200 nm can be used to probe excited states in the VUV situated between 200 and 100 nm. Commercial laser dyes with emission wavelengths of ∼300 nm and longer are commonly used and by frequency–doubling of the dye laser output it is possible to have a tunable laser up to 205 nm (48 750 cm^{-1}), which in theory enables probing of energy levels up to about 97 500 cm^{-1} using two–photon excitation.

The theory of two–photon excitation was developed by Maria Göppert-Mayer [11] in 1931. Using a second order perturbation theory, she predicted the possibility of the simultaneous absorption of two photons. For one photon electric dipole transitions the transition probability P_{OPA} is [12]

$$P_{\mathrm{OPA}} \propto \nu \ |< f|D|g >|^2 \tag{4.1}$$

In this formula g and f are the ground and final state respectively, ν is the frequency of the photon absorbed. For intraconfigurational $4f^n$–$4f^n$ transitions, both $|g>$ and $<f|$ are odd–parity wavefunctions. The electric dipole operator D is odd–parity and the resulting integral gives a zero transition probability. Since the electric dipole operator is odd–parity it cannot connect two states with the same parity. Therefore $4f^n$–$4f^n$ transitions are called parity–forbidden. The reason that these transitions still can be observed was explained by Van Vleck in 1937 [13]. Due to admixture of opposite parity configurations like $4f^{n-1}5d$ states the transitions become partially allowed as forced electric dipole transitions.

Two–photon excitation involves a virtual intermediate state. The transition probability P_{TPE} via all possible virtual intermediate states $|x>$ is given by [14]

$$P_{\mathrm{TPE}} \propto \left| \sum_x \left(\frac{< f|D|x >< x|D|g >}{E_{\mathrm{g}} + \hbar\omega_1 - E_{\mathrm{x}}} + \frac{< f|D|x >< x|D|g >}{E_{\mathrm{g}} + \hbar\omega_2 - E_{\mathrm{x}}} \right) \right|^2 \tag{4.2}$$

In this formula ω_1 and ω_2 are the frequencies of the two photons. The ground state $|g>$ and final state $|f>$ are odd–parity $4f^n$ wavefunctions. For transitions involving opposite–parity intermediate configurations, like $4f^{n-1}5d$ states, integrals $< f|D|x >< x|D|g >$ become nonzero and two–photon absorptions are therefore parity–allowed for $4f^n$–$4f^n$ transitions and parity–forbidden for $4f^n$–$4f^{n-1}5d$ transitions.

Although formally parity–allowed, the transition probability for a two–photon excitation is typically about a million times lower than for a one–photon absorption. It requires an intense excitation source and therefore the first observation of two–photon excitation was not until the 1960s shortly after the invention of the laser. In 1961 Kaiser and Garrett [15] performed two–photon excitation of CaF_2:Eu^{2+}. The output of a ruby laser was

used to excite the Eu^{2+} ions from the $4f^7$ ground state into the $4f^65d$ band. Upon excitation with 694.3 nm radiation, emission from the $4f^65d$ state at 410 nm was observed and the emission intensity showed a quadratic dependence on the excitation power.

Downer [3, 16] compared two–photon excitation measurements for intraconfigurational $4f^7$ transitions of Gd^{3+} and Eu^{2+} ions with calculated two–photon excitation spectra. In order to have a better agreement between calculation and experiment, he expanded the theory of two–photon absorption with third and fourth order perturbation theory. Energy levels of Gd^{3+} up to the ^6D_J levels around 40 000 cm^{-1} were observed, but measurement of the ^6G_J levels starting at 50 000 cm^{-1} was not successful, one of the reasons being the presence of impurities for which the one-photon absorption and resonant upconversion or excited state absorption was competing with the much weaker two–photon absorption of gadolinium ions. Eu^{3+} ions are frequently found as impurity in gadolinium samples. The $^5D_3$ and $^5L_6$ levels are situated around 25 000 cm^{-1} and resonant upconversion into one of the many levels around 50 000 cm^{-1} of Eu^{3+} followed by energy transfer to gadolinium ions hampers the observation of two–photon excitation of the gadolinium ^6G_J levels around 50 000 cm^{-1}.

In addition defect absorption bands in the VUV may be responsible for the fact that previous direct two–photon excitation experiments to observe the VUV levels of Gd^{3+} have failed. As an alternative method the next section will discuss excited state absorption.

4.3 Excited state absorption

In contrast with direct two–photon absorption, excited state absorption involves no virtual intermediate state. Instead, the ion under investigation is excited to a metastable intermediate energy level, followed by a second excitation to higher energy levels. Next, multiphonon relaxation occurs until an emitting level, having an energy gap to the next lower level of more than 4 to 5 times the maximum phonon energy of that lattice, is reached and emission from this level is observed. When the emitting level is situated above the first metastable level, anti–Stokes emission is observed when excited state absorption takes place.

The trivalent gadolinium ion has a suitable energy level scheme for excited state absorption measurements (see figure 4.2). First, excitation around 310 nm brings the ion to the $^6P_{7/2}$ state. After absorption of a second photon and (possibly) multi-phonon relaxation, emission occurs from the $^6I_{7/2}$, $^6D_{9/2}$ and $^6G_{7/2}$ levels at respectively 272 nm, 252 nm and 203 nm. Detection of one of these three anti–Stokes emissions can then be used as a probe for excited state absorption.

Excited state absorption measurements have some advantages compared to two–photon excitation. First, the transition probabilities are higher as the oscillator strength is about 6 orders of magnitude higher. Second, impurities are less of a problem when the ion under

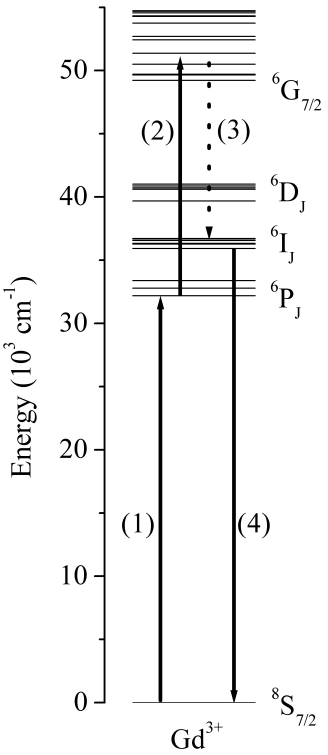

Figure 4.2: Energy level scheme showing free–ion levels for Gd^{3+} up to 55 000 cm^{-1} with arrows indicating the transitions for excited state absorption. (1) Excitation into the $^6P_{7/2}$ level, (2) excitation using a tunable laser, (3) relaxation to the $^6I_{7/2}$ level, and (4) anti–Stokes emission from the $^6I_{7/2}$ level.

investigation is being excited selectively. Tuning of the first excitation laser to an energy that corresponds to a resonant transitions of the Gd^{3+} ion (in figure 4.2 a $^8S_{7/2}\rightarrow{}^6P_{7/2}$ transition) gives the two–photon excitation process for the Gd^{3+} ion a strong enhancement over undesired two–photon excitation processes involving impurities or defects.

In the case of gadolinium another advantage is that the first excited state ($^6P_{7/2}$) is a spin sextet. Transitions to the higher sextets and quartets have a higher transition probability than transitions to these states starting from the octet $^8S_{7/2}$ ground state of Gd^{3+}. Starting at about 67 000 cm^{-1} also spin doublet states are calculated. Transitions to these states involve an extra spin-flip and therefore are much weaker.

4.4 Experimental

4.4.1 Sample preparation

Microcrystalline powders of LaF_3:Gd^{3+} and GdF_3 were prepared in a Philips PH 1006/13 high–frequency furnace with LaF_3 and GdF_3 as the starting compounds. The reactants were mixed and transferred to a vitreous carbon crucible. In order to remove water and air the sample was heated overnight at 300°C in a flow of ultrapure nitrogen ($<$ 10 ppm O_2). Subsequently the temperature was raised to 550°C and SF_6 was let into the reaction chamber for 30 minutes to remove the last traces of water and oxygen. During the rest of the synthesis a nitrogen atmosphere was maintained. The sample was heated until melting was observed. Next, the sample was cooled to room temperature in a few hours. The powders obtained were checked for phase purity by recording a powder diffractogram using a Philips PW1729 X-ray diffractometer using CuK_α radiation. All samples were single phase.

A single crystal of LaF_3 doped with 0.5% Gd^{3+} was grown in a Philips PH 1006/13 high–frequency furnace using the vertical Bridgman method. A slice of approximately 7 mm in diameter and with a thickness of 2 mm was cut and polished and glued to a copper sample holder.

4.4.2 Two–photon excitation

Two–photon excitation experiments were performed using a Lambda Physik LPD 3002 Dye laser which was pumped with a Lambda Physik LPX100 XeCl excimer laser. The laser was triggered externally at 8 Hz using a pulse generator. The dyes used for the two–photon excitation experiments are listed in table 4.1. Measurements were performed at $\sim$10 K using an Oxford Instruments liquid helium cold–finger flow cryostat, equipped with quartz windows.

Emission from the $^6P_{7/2}$ level at 311 nm was detected using a thermo–electrically cooled Hamamatsu R928-02 photomultiplier tube in combination with a set of filters blocking the excitation wavelengths. For the detection of emission from the $^6I_{7/2}$ level at 278 nm a Hamamatsu R7154 solar blind photomultiplier tube was used in combination with an interference filter for the region 277–280 nm. Gated detection of the amplified signal was performed using a Stanford Research SR400 boxcar averager with a delay of 100 μs and a gate of 3 ms.

4.4.3 Excited state absorption

Excited state absorption measurements were performed at approximately 10 K using an Air Products APC HC–2 cold finger type closed cycle cryostat fitted with quartz windows. The experimental setup for ESA (see figure 4.3) consisted of two tunable lasers. The first

Table 4.1: Laser dyes used for two–photon excitation measurements. The excitation region and corresponding energy levels of Gd^{3+} that can be reached by two–photon excitation are indicated in the last two columns.

Dye	Wavelength (nm)	Excitation region (cm^{-1})	Gd^{3+} levels
Sulforhodamine B	594 – 642	31150 – 33670	^6P_J
Coumarine 153	520 – 600	33300 – 38460	^6I_J
Coumarine 102	460 – 510	39200 – 43480	^6D_J
PBBO	386 – 420	47620 – 51810	^6G_J

was a Spectra–Physics PDL3 dye laser pumped by a frequency doubled Spectra-Physics Quanta Ray Nd:YAG laser operating at 15 Hz. A Rhodamine B laser dye solution was used to obtain a laser tunable around 620 nm. This red laser beam was frequency doubled to a UV laser with a wavelength of 310.25 nm by a Spectra–Physics wavelength extender with KDP crystals. The second laser used was a Lambda Physik LPD 3002 Dye laser which was pumped with a Lambda Physik LPX 100 XeCl excimer laser. A Stanford Research Systems DG535 digital delay/pulse generator was used to trigger the excimer laser and YAG laser. Both laser beams were focussed on the same spot in the crystal using mirrors and lenses. The emission from the crystal was collected using a cooled Hamamatsu R7154 solar blind photomultiplier tube. Various band and interference filters were used to block any light within the wavelength range of the excitation sources. The spectra obtained were corrected for the intensity of the dye laser using dye output spectra recorded with a power meter. The dyes used for the ESA experiments are listed in table 4.2.

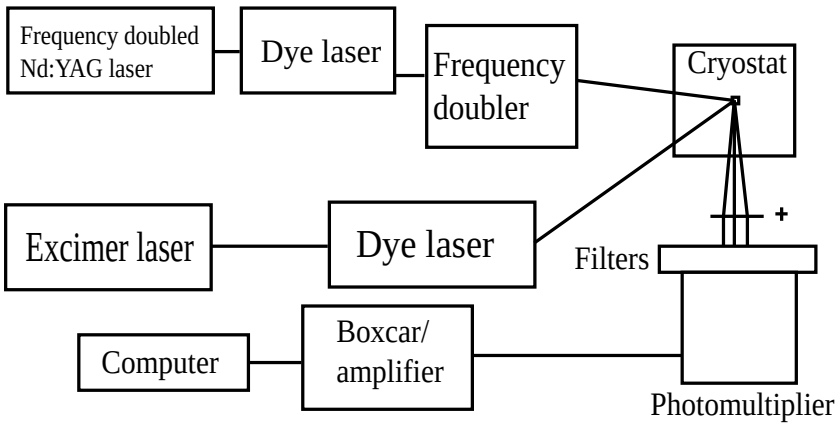

Figure 4.3: Experimental setups for excited state absorption and two–photon excitation. For two–photon excitation the Nd–YAG laser at the top is not used.

4.5 Results and Discussion

4.5.1 Two–photon excitation

Two–photon excitation (TPE) spectra for LaF_3:Gd^{3+} 0.5% and GdF_3 (powder) were recorded in the wavelength region of the ^6P_J, ^6I_J, ^6D_J and ^6G_J levels. For the ^6P_J

Table 4.2: Laser dyes used for excited state absorption measurements. The excitation region that is reached by the sum of the energies of the UV laser (310 nm) and the second dye laser is indicated in the last column.

Dye	Wavelength (nm)	Excitation region (cm^{-1})
Rhodamine 6G	570 – 600	48900 – 49700
Coumarine 153	520 – 580	49400 – 51400
Coumarine 307	470 – 540	50700 – 53500
Coumarine 120	430 – 470	53500 – 55500
Bis-MSB	403 – 436	55100 – 57000
PBBO	388 – 420	56000 – 58000
BiBuQ	375 – 390	57800 – 58800
DMQ	350 – 385	58100 – 60700
PTP	340 – 355	60400 – 61600

and $^6\mathrm{I}_J$ levels high resolution excitation spectra were obtained.

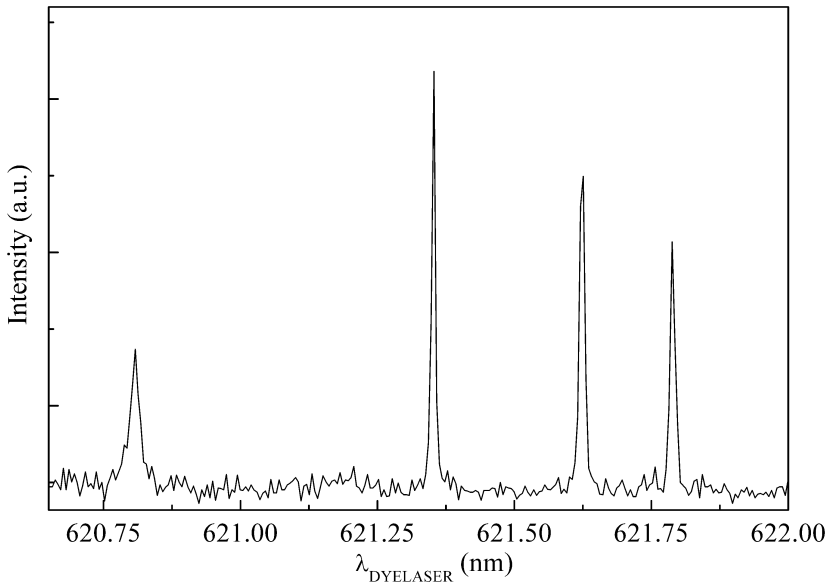

Figure 4.4: Two–photon excitation spectrum of the $^6\mathrm{P}_{7/2}$ levels of LaF_3:Gd^{3+} monitoring $^6\mathrm{P}_{7/2}$ emission at 4 K.

Figure 4.4 shows the two–photon excitation spectrum of the LaF_3:Gd^{3+} 0.5% crystal for the $^6\mathrm{P}_{7/2}$ level situated at about 32200 cm^{-1}. All four crystal-field levels were observed and their experimental and calculated energies (discussed below) are listed in table 4.3. In figure 4.5 the two–photon excitation spectrum is shown for the $^6\mathrm{I}_J$ levels of GdF_3 in the wavelength region 270–280 nm (dye laser scanned between 540 and 560 nm). In the spectrum 36 of the 39 expected energy levels are observed. The linewidths of the excitation lines are about 1 cm^{-1}, corresponding to the inhomogeneous linewidth of the transitions. From this high resolution excitation spectrum the positions of the $^6\mathrm{I}_J$ can be determined with great accuracy. Attempts to measure the TPE spectra for the higher energy $^6\mathrm{D}_J$ and $^6\mathrm{G}_J$ levels were not successful. Possibly, the lower oscillator strengths hamper the observation of TPE. For the $^6\mathrm{G}_J$ (situated around 200 nm) also the presence of trace amounts of Eu^{3+} ions interfered with the observation of TPE by Gd^{3+}. Eu^{3+} has many absorption lines around 400 nm. Since a one-photon absorption has a transition probability which is several orders of magnitude higher than a two–photon excitation, absorption around 400 nm excites the europium ions into the $^5\mathrm{D}_3$ and $^5\mathrm{L}_6$ states from which excited state absorption can occur into the europium levels around 50 000 cm^{-1} followed by energy transfer to the gadolinium ions. Since the probability of this excited state ab-

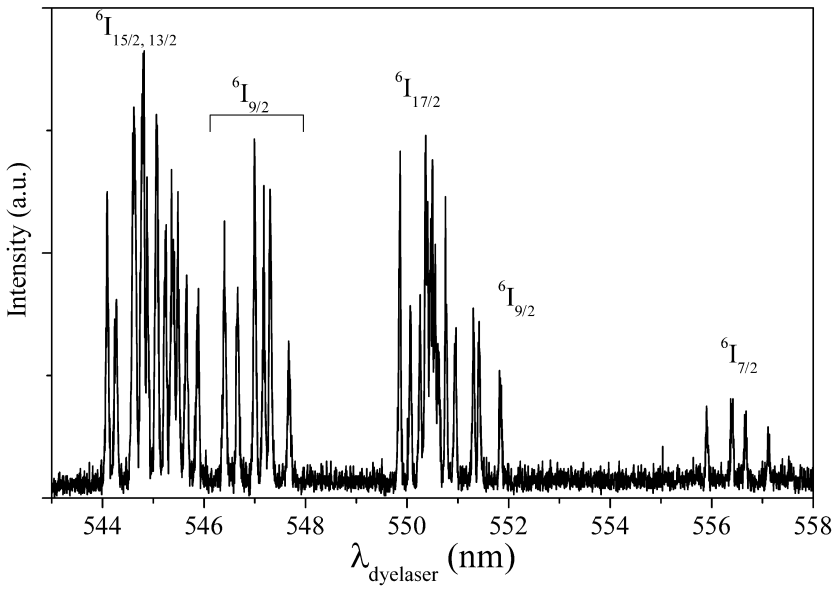

Figure 4.5: Two–photon excitation spectrum of the ^6I_J levels of GdF_3 monitoring $^6P_{7/2}$ emission at 4 K.

sorption is higher than for two–photon excitation, the gadolinium emission originating from the excited state absorption increases the baseline and two–photon absorption peaks cannot be observed anymore. Further experiments on crystals with higher Gd^{3+} concentrations and preferably no impurities may be used to measure the higher energy levels of Gd^{3+} by TPE.

4.5.2 Excited state absorption

This section describes the excited state absorption spectra and the assignment of the experimentally observed energy levels to an energy level scheme calculated for Gd^{3+} in LaF_3. The calculated energy level scheme is based on the parameter values listed by Carnall [2] based on 70 experimentally observed energy levels in the energy region up to 50 000 cm^{-1}. In these energy level fittings, the B_q^k crystal field parameter values were not varied, but were fixed at the parameter values for terbium. In order to make a comparison of parameter values based on fitting of the lower energy (UV) levels with the parameter values obtained from fittings including the VUV energy levels possible, we refitted the data of Carnall. We performed a least squares fitting of the B_q^k for all 70 experimentally observed levels up to 50 000 cm^{-1} as listed by Carnall. Only the cylindrically symmetric B_0^k's were allowed to vary, the other crystal field parameters were kept at fixed (terbium)

Table 4.3: Energies of the four $^6P_{7/2}$ crystal field levels of Gd^{3+} in LaF_3 determined from the two–photon excitation spectrum. The calculated energies are based on parameters from Carnall [2] and are discussed in section 4.5.2.

λ_{LASER} (nm)	E_{EXP} (cm^{-1})	E_{CALC} (cm^{-1})	E_{EXP}–E_{CALC} (cm^{-1})
621.46	32182	32147	35
621.32	32190	32154	36
621.02	32205	32172	33
620.50	32232	32202	30

ratios to the B_0^k values. Using 70 data points and varying 10 parameters a fit with a standard deviation of 8.0 cm^{-1} was obtained. As expected, the quality of the fit has improved (smaller σ and r.m.s. by allowing the variation of the B_0^k parameter values. All parameter values are listed together with their uncertainties in table 4.4.

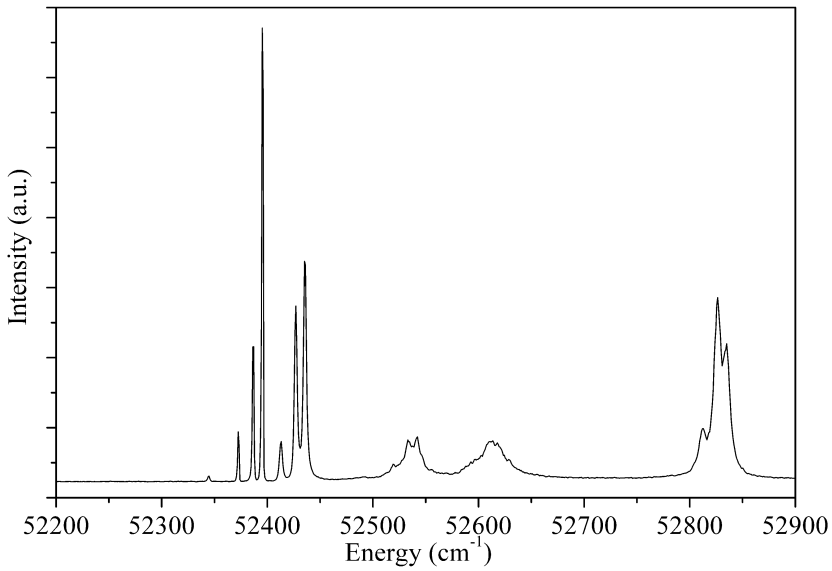

Figure 4.6: Excited state absorption spectrum of the $^4D(6)_{7/2}$ and $^6F_{1/2}$ levels of LaF_3:Gd^{3+} monitoring $^6I_{7/2}$ emission at 10 K.

A typical example of an excited state absorption spectrum is shown in figure 4.6. This spectrum shows absorptions to the four crystal field levels of the $^4D(6)_{7/2}$ state and the

Table 4.4: Free–ion and crystal field parameters for LaF_3:Gd^{3+} based on fitting the lower energy (UV) levels of Gd^{3+}. The left column shows the parameters reported by Carnall [2] and the right column shows the parameters obtained by fitting to the experimental energy levels reported by Carnall for LaF_3:Gd^{3+} as described in the text. Parameters for which no uncertainty is given were not varied.

Parameter	Carnall Value (cm^{-1})	New fit Value (cm^{-1})
E_{AVG}		87 812(11)
F^2	85 669(17)	85 592(18)
F^4	60 825	61 015(29)
F^6	44 776(24)	44 745(25)
α	18.92(0.83)	19.14(0.10)
β	–600	–600
γ	1575	1575
T^2	300	300
T^3	42	42
T^4	62	62
T^6	–295	–295
T^7	350	350
T^8	310	310
ζ	1508(2)	1499(2)
M^0	3.22(0.2)	3.20(0.03)
M^2	0.56 M^0	0.56 M^0
M^4	0.31 M^0	0.31 M^0
P^2	676(75)	676
P^4	0.5 P^2	0.5 P^2
P^6	0.1 P^2	0.1 P^2
B_0^2	–231	–212(14)
B_0^4	604	579(40)
B_0^6	280	292(22)
B_2^2	–99	0.4286 B_0^2
B_2^4	340	0.5629 B_0^4
B_4^4	452	0.7483 B_0^4
B_2^6	–721	–2.575 B_0^6
B_4^6	–204	–0.7286 B_0^6
B_6^6	–509	–1.8179 B_0^6
N	70	70
σ	10	8
r.m.s.	9	7

absorption to the $^6F_{1/2}$ level, which cannot be split by the crystal field because J=1/2. In the spectrum in figure 4.6 more than the five expected transitions are observed. Upon excitation into the $^6P_{7/2}$ multiplet, fast relaxation to the lowest crystal field level occurs.

The other three crystal field levels are thermally populated according to a Boltzmann distribution. Especially the second level, which is situated only 8 cm^{-1} above the lowest level (in LaF_3), is still considerably populated (24%) at a temperature of 10 K.

The population of the higher crystal field levels gives rise to more absorption lines in the excited state absorption spectrum, since excitations from the thermally populated levels can also occur. Next to the main absorption peak, extra absorptions at energy separations equal to the splitting of the $^6P_{7/2}$ levels can be expected. In some cases it is easy to recognize the difference between these transitions since the energy separations between the $^6P_{7/2}$ levels are known exactly. If the energy levels are closer together than about 50 cm^{-1} which is the total splitting of the $^6P_{7/2}$ levels, absorption peaks will overlap and the spectra should be interpreted more carefully. Although the populations of the four $^6P_{7/2}$ levels can be estimated using a Boltzmann-distribution, it is not possible to relate this to the relative absorption intensities since they also depend on symmetry and polarization. This is clearly visible for the absorption to the $^6F_{1/2}$ level at about 52 800 cm^{-1}, where the transition originating from the second $^6P_{7/2}$ crystal field level is the most intense transition. In table 4.5 the experimental energies of the $^4D(6)_{7/2}$ and $^6F_{1/2}$ levels are listed together with the calculated energies and M_J values for these levels using parameters from table 4.4. As the calculated energy levels contain contributions of wavefunctions of several states, the M_J value having the largest contribution is listed. The experimental energies of the levels were determined by adding the energy of the lowest $^6P_{7/2}$ level to the energies of the peaks in the excited state absorption spectrum that corresponds to excited state absorption from the lowest $^6P_{7/2}$ level. In all excited state absorption spectra shown in this chapter, this energy has been added to the values on the x–axis.

Table 4.5: Experimentally observed and calculated energies of the $^4D(6)_{7/2}$ and $^6F_{1/2}$ levels of Gd^{3+} in LaF_3. The calculations are based on the parameters from table 4.4.

Energy level	M_J	E_{EXP} (cm^{-1})	E_{CALC} (cm^{-1})	$E_{EXP} - E_{CALC}$ (cm^{-1})
$^4D(6)_{7/2}$	±5/2	52396	52356	40
$^4D(6)_{7/2}$	±3/2	52436	52370	66
$^4D(6)_{7/2}$	±1/2	52541	52490	51
$^4D(6)_{7/2}$	±7/2	52617	52554	63
$^6F_{1/2}$	±1/2	52835	52729	106

All experimentally observed energies are about between 40 and 100 cm^{-1} higher compared to the calculated energies. This clearly shows that there is a mismatch between experiment and calculation for the higher energy levels when only a set of low energy

levels is used to fit the parameters. Although there is a significant difference between the calculated and observed energies, assignment of these levels is still possible since there is an energy gap of 1000 cm^{-1} above and below these levels.

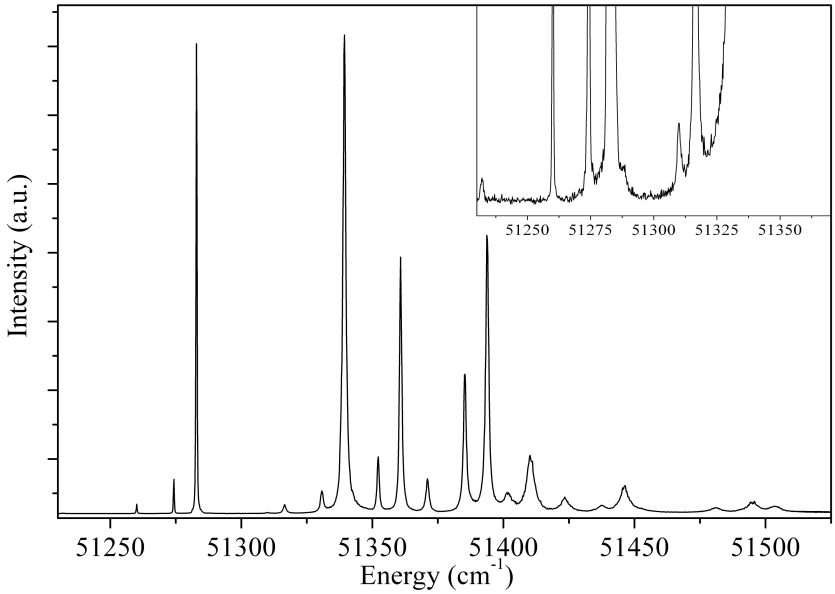

Figure 4.7: Excited state absorption spectrum of the $^6G_{13/2}$ levels of LaF_3:Gd^{3+} monitoring $^6I_{7/2}$ emission at 10K. The inset shows a magnified view of the region 51 230 – 51 350 cm^{-1}.

A second effect, besides the observation of more lines due to thermal population of the $^6P_{7/2}$ crystal field components, that complicates the determination of all VUV energy levels from the excited state absorption spectra is broadening of some of the absorption peaks. This is clearly visible in the spectrum shown in figure 4.7 which shows all seven crystal field levels of the $^6G_{13/2}$ multiplet. The broadening in the spectrum is probably caused by lifetime broadening due to fast relaxation, which is expected when there are energy levels below the one investigated at energy separations of approximately 100–350 cm^{-1}. The relaxation rate, at low temperatures, is due to a phonon emission process. The highest relaxation rates are for one–phonon emission. The rate is dependent on the density of states in the phonon spectrum. The phonon density of states increases with energy (in the Debye model the density of states is proportional to ω^2) which explains the lower limit of 100 cm^{-1}. The phonon cut–off energy in LaF_3 is about 350 cm^{-1}. For bridging energy gaps higher than 350 cm^{-1} multi–phonon emission processes are involved which have lower rates. A more quantitative analysis of the linewidth is beyond

Table 4.6: Experimentally observed and calculated energies of the seven $^6G_{13/2}$ levels of Gd^{3+} in LaF_3. For the calculation the parameters from table 4.4 were used. The crystal field levels of the $^6P_{7/2}$ multiplet from which the absorption originates is also indicated, where number 1 indicates the lowest level.

$^6G_{13/2}$ level	E_{EXP} (cm^{-1})	E_{CALC} (cm^{-1})	$^6P_{7/2}$ Origin
1	51 232		4
1	51 260		3
1	51 274		2
1	51 283	51 269	1
2	51 288		4
3	51 310		4
2	51 316		3
2	51 331		2
2	51 339	51 319	1
3	51 352		2
3	51 361	51 346	1
4	51 371		3
4	51 385		2
4	51 393	51 366	1
5	51 404		2
5	51 410	51 385	1
6	51 423		3
6	51 438		2
6	51 447	51 400	1
7	51 481		3
7	51 496		2
7	51 503	51 450	1

the scope of the present work. The broadening effect is illustrated in figure 4.7, where the lowest crystal field level of the $^6G_{13/2}$ multiplet is observed at 51 280 cm^{-1}. Broadening of the absorption peaks is expected starting at about 51 400 cm^{-1}, which is observed in the spectrum. In table 4.6 the experimentally determined energies are listed together with the calculated energies for the $^6G_{13/2}$ levels using parameters from table 4.4. The line broadening causes a weaker maximum absorption and overlapping of absorption peaks which hampers the observation of many transitions, especially in the energy region above 55 000 cm^{-1}.

The assignments in table 4.6 are based on the observation of the splitting pattern of

the $^6P_{7/2}$ level from which excitation occurs. The difference between calculated and experimental energies increases going from the lowest to the highest multiplet level. Above the highest $^6G_{13/2}$ crystal field level an energy gap of approximately 1000 cm^{-1} to the next higher level is calculated.

Another phenomenon that influences absorption intensities is the spin selection rule. The excited state from which excited state absorption occurs ($^6P_{7/2}$) is a spin sextet. Transitions to other sextets are spin-allowed and are more intense than transitions to spin-quartet levels, and transitions to spin-doublet levels are expected to be too weak to be observed. At energies of 55 900 cm^{-1} and higher spin quartet levels are calculated, above 67 000 cm^{-1} spin doublet states are also calculated. For lanthanide ions the spin selection rule is lifted by the strong spin–orbit coupling which mixes states of the same J value but with different spin multiplicity. As a result, the influence of the spin selection rule is a general trend while for a better understanding of the intensities it is necessary to consider all states contributing to a certain level that is labelled by the term symbol for the state with the largest contribution.

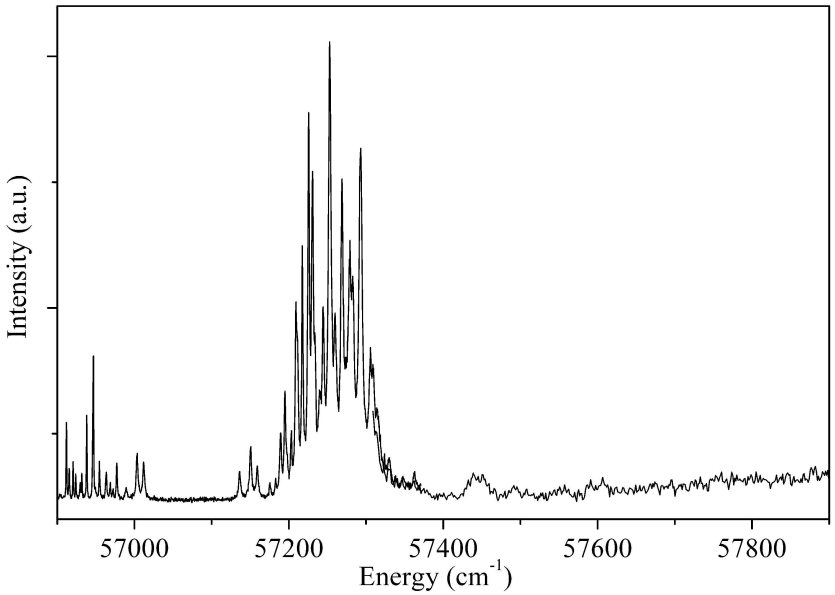

Figure 4.8: Excited state absorption spectrum of LaF_3:Gd^{3+} in the region 56 900 – 57 900 cm^{-1} monitoring $^6I_{7/2}$ emission at 10 K. Two different laser dyes were used for recording this spectrum with an overlap around 57 600 cm^{-1}.

Figure 4.8 shows the ESA spectrum for the region 56 900 – 57 900 cm^{-1}. In the region 57 450 – 57 820 cm^{-1} 16 levels are calculated for which the two largest contributions are

from spin quartet states. Only some weak absorptions are observed, and it is not possible to assign these to specific calculated energy levels. The low intensities of the absorption peaks in this region is also partly due to their quartet spin character. Between 57 130 and 57 450 cm^{-1} 27 energy levels are calculated and five of them have a sextet state among the two states with the highest contribution. In the spectrum of figure 4.8 intense absorptions are observed in this region. Also for the region 56 900 to 57 000 cm^{-1} levels with a considerable sextet character are calculated and observed.

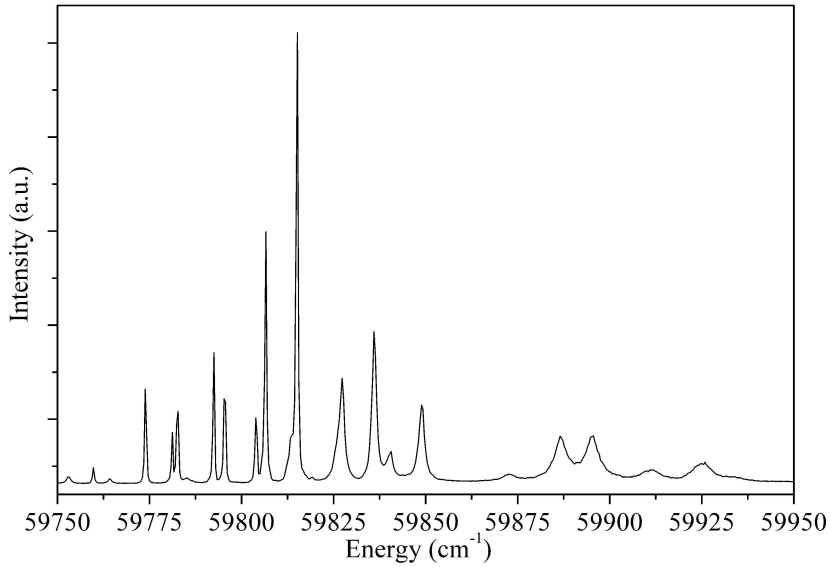

Figure 4.9: Excited state absorption spectrum of the $^6H_{13/2}$ multiplet in LaF_3:Gd^{3+} in the region 59 750 – 59 950 cm^{-1} monitoring $^6I_{7/2}$ emission at 10 K.

In lanthanide spectroscopy J is a better quantum number and J–selection rules apply. For electric dipole transitions ΔJ is limited to a maximum of ± 6. This means that electric dipole transitions originating from the $^6P_{7/2}$ state are allowed up to levels with a J of 19/2. The levels with the highest J levels for Gd^{3+} are the $^2Q_{23/2}$ and $^2Q_{25/2}$ level. These levels cannot be observed, due to a ΔJ of 8 or 9 and a change in spin of 2.

Since not all energy levels could be observed, assignment of especially the levels above 54 000 cm^{-1} was not always possible. Energy levels can only be used for the least squares fitting procedure if all crystal field levels of an isolated multiplet were observed. Figure 4.9 shows the absorptions of the $^6H_{13/2}$ multiplet, for which all 7 crystal field levels are observed. The calculated and experimentally obtained energies of the $^6H_{13/2}$ levels are listed in table 4.7. The difference between experimental and calculated energies

varies between 115 and 135 cm^{-1}. This indicates a shift of the whole multiplet, while the crystal field splitting is good.

Table 4.7: Experimentally observed and calculated energies of the $^6H_{13/2}$ levels of Gd^{3+} in LaF_3.

M_J	E_{EXP} (cm^{-1})	E_{CALC} (cm^{-1})	$E_{EXP} - E_{CALC}$ (cm^{-1})
±13/2	59781	59658	123
±7/2	59804	59679	125
±5/2	59815	59699	116
±1/2	59836	59708	128
±11/2	59849	59721	128
±9/2	59895	59763	132
±3/2	59933	59798	135

The highest two multiplets observed are the $^4F(4)_{9/2}$ and $^4F(4)_{7/2}$ levels in the region 60 900 to 61 400 cm^{-1}. The spectrum in figure 4.10 shows all crystal field levels and their energies, which are collected in table 4.8.

Table 4.8: Experimentally observed and calculated energies of the $^4F(4)_{9/2}$ and $^4F(4)_{7/2}$ levels of Gd^{3+} in LaF_3.

Energy level	M_J	E_{EXP} (cm^{-1})	E_{CALC} (cm^{-1})	$E_{EXP} - E_{CALC}$ (cm^{-1})
$^4F(4)_{9/2}$	±7/2	60927	60773	154
$^4F(4)_{9/2}$	±5/2	60964	60839	125
$^4F(4)_{9/2}$	±1/2	61016	60860	156
$^4F(4)_{9/2}$	±3/2	61075	60921	154
$^4F(4)_{9/2}$	±9/2	61088	60944	144
$^4F(4)_{7/2}$	±5/2	61334	61208	126
$^4F(4)_{7/2}$	±7/2	61344	61213	131
$^4F(4)_{7/2}$	±1/2	61365	61226	139
$^4F(4)_{7/2}$	±3/2	61388	61245	143

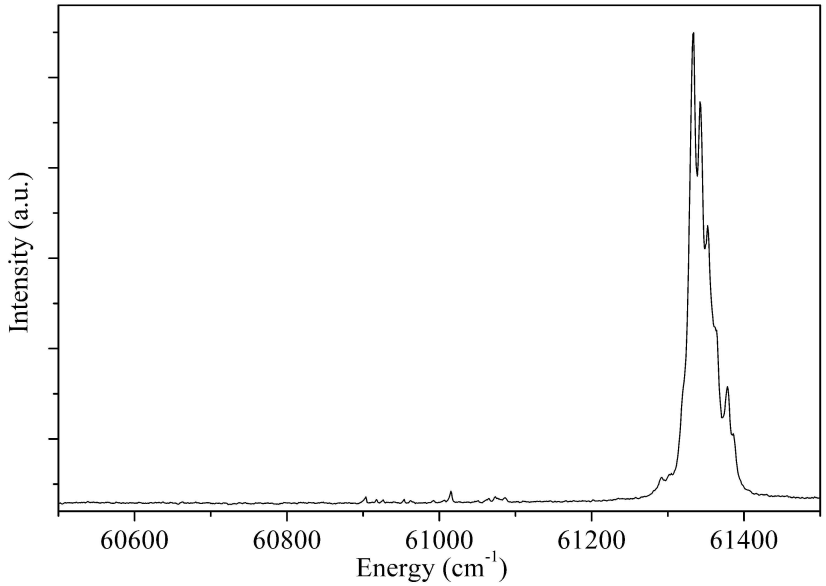

Figure 4.10: Excited state absorption spectrum of the ^{4}F(4)$_{9/2}$ and ^{4}F(4)$_{7/2}$ multiplets in LaF$_3$:Gd^{3+} in the region 60 900 to 61 400 cm^{-1} monitoring ^{6}I$_{7/2}$ emission at 10 K.

All experimentally observed energy levels and the assignments to the different multiplets are given in Appendix A. Note that the energy differences listed in the appendix are the differences with the calculated energies using fitted calculation parameters from table 4.4 based on the observed UV energy levels reported by Carnall [2]. In the next section the fitting procedure will be discussed leading to improved parameter values by including the presently observed high energy (VUV) energy levels of Gd^{3+} in LaF_3.

Figure 4.11 shows the excited state absorption spectrum for the complete range of dyes used. The energy on the horizontal axis is the energy at which excited state absorption peaks are observed added to 32182 cm^{-1}, the energy of the lowest ^{6}P$_{7/2}$ level. The spectrum has been corrected for the laser intensity using correction files recorded for each dye. The spectra for correction for the intensity of the UV dyes could not be measured and the intensity of the ESA spectrum in the region above 57 000 cm^{-1} has been scaled to the efficiencies of the dyes used. This results in an estimated error in intensity of 10 to 20 %. Furthermore, some wavelength regions were obtained using the same dye, but with a different grating order of the laser. This leads to small discrepancies in intensity and causes the small shifts of baseline in the spectrum.

Figure 4.12 shows the calculated excited state absorption spectrum in the same energy

range based on the newly fitted parameter values. Section 4.5.3 will discuss the fitting method used. For the simulated spectrum the temperature has been set to 10 K and a linewidth of 1.5 cm^{-1} was chosen.

The general agreement between the calculated spectrum and the observed spectrum is good. The strong lines in the calculated spectrum show up as strong lines in the experiment and lines for which a small intensity is calculated are weak or not observed. However, not all experimentally observed absorption intensities show a good agreement with the intensities in the calculated spectrum. Some of the absorption lines are broadened, while in the calculated spectrum the same linewidth is given to every absorption line leading to (peak)–intensities that are higher in the calculation than in the experiment. This can explain why the peak intensity for the broadened lines just below 50 000 cm^{-1} is lower than for the sharp lines in the calculated spectrum for this spectral region. The calculated intensity of the absorption lines around 50 500 cm^{-1} and 57 250 cm^{-1} is remarkably lower than the experimental intensity. Also, the absorption lines around 61 400 cm^{-1} are lower in the calculation when compared to the experimentally observed intensities. These differences may be caused to some extent by a wrong correction file for the output of the dye laser, especially for the UV region, where we used the relative efficiencies of the dyes as a correction factor. The discrepancy between the calculated and observed intensities for some of the lines is too large to be explained by correction errors for the dye laser intensities. Further improvements in the model used may resolve the discrepancy.

For comparison, figure 4.13 shows the one–photon excitation spectrum of the same crystal of LaF_3:Gd^{3+} 0.5% recorded at the DESY synchrotron, monitoring $^6P_{7/2}$ emission at 311 nm. In this spectrum only groups of energy levels can be observed, the individual splitting by the crystal field cannot be resolved. The poor resolution and low signal to noise ratio in this spectrum, compared to for example the one–photon excitation spectrum for $LiYF_4$:Gd^{3+} 5% shown in figure 4.1, is related to the low Gd^{3+} concentration (0.5%) and defect absorption bands in the VUV. In the one–photon excitation spectrum the excitation lines that can be observed do coincide with the stronger excitation lines in the excited state absorption spectrum.

4.5.3 Fitting of parameters values

The positions of all energy levels that could be identified for Gd^{3+} in LaF_3 based on the excited state absorption spectra are collected in Appendix A. In this appendix we have also included the energy differences with the calculated energies using the parameter values obtained from fitting the lower energy (UV) levels which are given in table 4.4 (second column). There is a clear difference between the calculated and observed energies. The energy difference ranges from $\sim$100 cm^{-1} for the lower energy VUV levels to 180 cm^{-1} for the highest energy levels. Clearly, the parameter values obtained from the lower energy

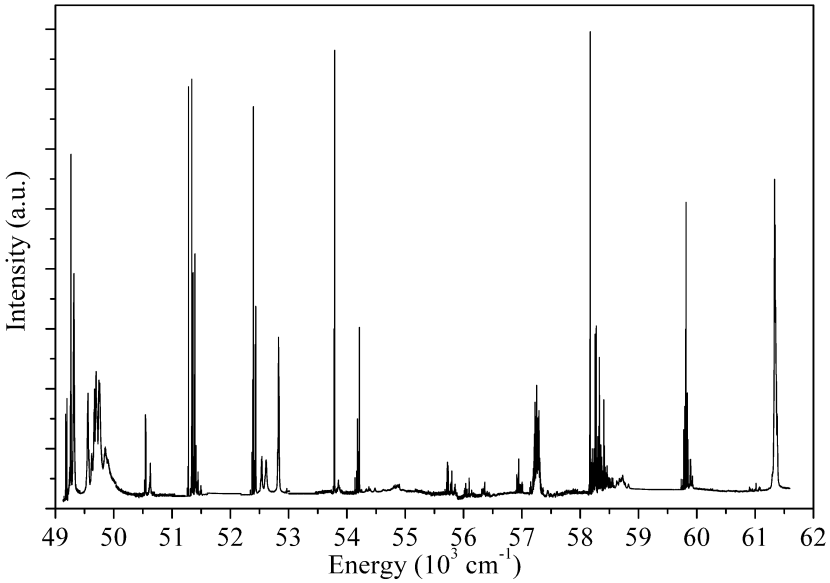

Figure 4.11: Excited state absorption spectrum of LaF_3:Gd^{3+} monitoring $^6I_{7/2}$ emission at 10 K for the complete (corrected) dye range of 49 000 – 62 000 cm^{-1} .

level fitting need to be improved to explain the positions of the high energy levels. The fitting procedure for the higher energy levels is not straightforward.

Although many energy levels were obtained by experiment, not all of them can be used in the parameter fitting procedure. Experimentally obtained energies have to be linked to specific energy levels in the calculation. Since the energy difference between the calculation based on Carnall's parameters and experiment increases when going to higher energies, assignment of a single level that matches in energy with a calculated energy level may not correspond to a correct assignment and could cause the fit to shift into the wrong direction.

Whenever possible complete multiplets have to be assigned. In the region 49 000 to 62 000 cm^{-1} the density of levels is still low enough to have energy gaps of about 1 000 cm^{-1} which facilitates the correct assignment of complete multiplets. Unfortunately, due to the broadening of levels or the occurrence of overlapping absorptions it was not always possible to assign a complete multiplet unambiguously. Overlap of multiplets also occurs in the calculated energy levels, which renders assignment impossible.

In order to extract new, and better, parameters describing the energy level structure for Gd^{3+} in LaF_3 it is important to carefully choose the energy levels that can be assigned unambiguously. Following the reasoning discussed above, 83 levels in the vacuum ultra-

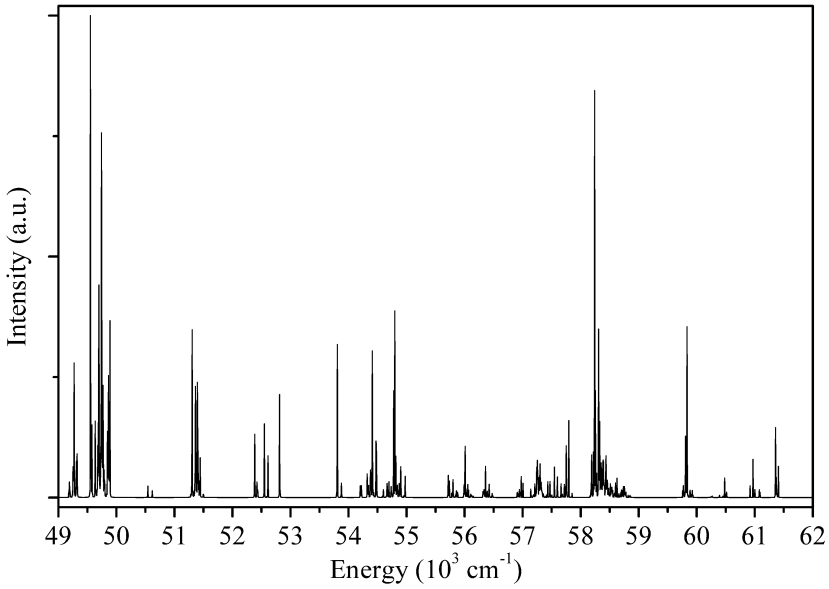

Figure 4.12: Calculated excited state absorption spectrum of LaF_3:Gd^{3+} from 49 000 – 62 000 cm^{-1}. The spectrum is calculated with parameter values listed in table 4.9 (third column) for absorption from the $^6P_{7/2}$ level at 10 K.

violet that were resolved by excited state absorption were used in the fitting procedure.

A second choice concerns the parameters that can vary in the fitting procedure. Allowing all parameters to vary freely often results in values that are not meaningful (e.g. wrong sign). To avoid this, the number of parameters needs to be limited to parameters that have a clear influence on the energy levels studied and fix the ratio of other parameters to established ratios.

First we consider the three–body interaction parameters T^i. The Crosswhite input files for the energy level program contain the matrix elements of the three electron operators t_i, and other electronic free–ion operators. The diagonal elements were all zero except for the elements of t_2. If no mixing of states would occur, T^2 would be the only three–body interaction parameter having effect on the energies. Since mixing of states cannot be neglected, the off–diagonal elements for the three-electron operators should be taken into account. This is more complicated, especially because of the large number of levels that have the same J value that can mix with each other. To get an impression of the relative influence of the T^n parameters on the energies, the free–ion levels of gadolinium were calculated while the value of each one of the six three–body interaction parameters was increased separately with 20 cm^{-1}. In figure 4.14 the change in energy of the free

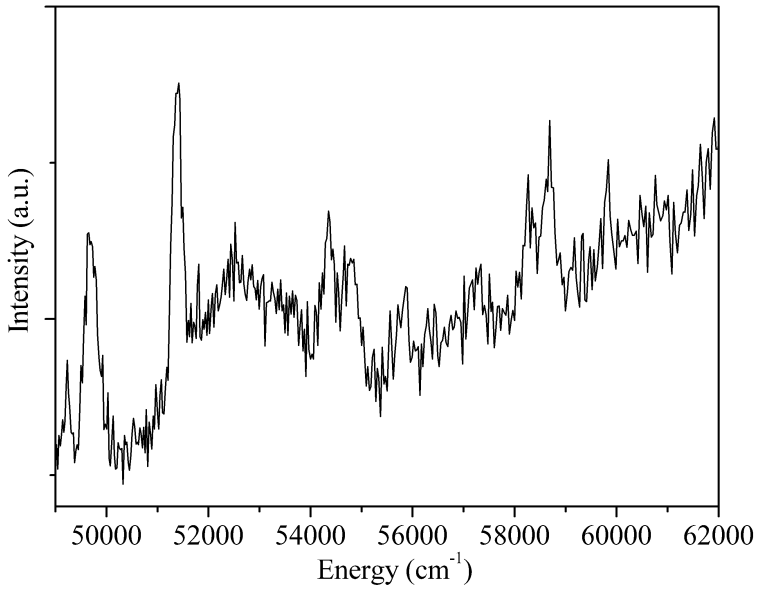

Figure 4.13: Excitation spectrum of LaF_3:Gd^{3+} 5% crystal recorded at the DESY synchrotron monitoring $^6P_{7/2}$ emission at 10 K

ion levels is plotted against the free ion energy level number. The vertical scale was set the same for each plot to facilitate comparison.

In our measurements the energy levels up to number 52 ($^4F(4)_{7/2}$) were probed using excited state absorption. For these levels only T^2 shows a large influence on nearly all the calculated energies, whereas for all other T^i parameters the energies of the levels up to level 52 are not affected by the change in the value for T (except for T^8 which gives a significant change in energy for level 32 ($^4H(2)_{7/2}$) and 34 ($^4H(2)_{13/2}$)). Based on this, it is reasonable to only allow T^2 to vary in the energy level fitting while keeping the other T's at constant values. The only way to fit the values of the T^3 up to T^8 for gadolinium in order to obtain more accurate values would be fits including higher energy levels. Starting at about free ion level 100 the T^3, T^4 and T^6 parameters have enough influence on the energy to fit them to experimental data. However, these levels are situated at 73 000 cm^{-1} and higher and have never been reported for Gd^{3+} in LaF_3. The density of levels is high at this energy, and energy differences between consecutive levels are generally about 10 cm^{-1}. Fast relaxation will broaden these levels in such an extent that assignment of these levels will be impossible. Moreover, at these energies most energy levels are spin quartet and doublet states. Therefore it is not possible to improve the values of T^3 to T^8 for gadolinium.

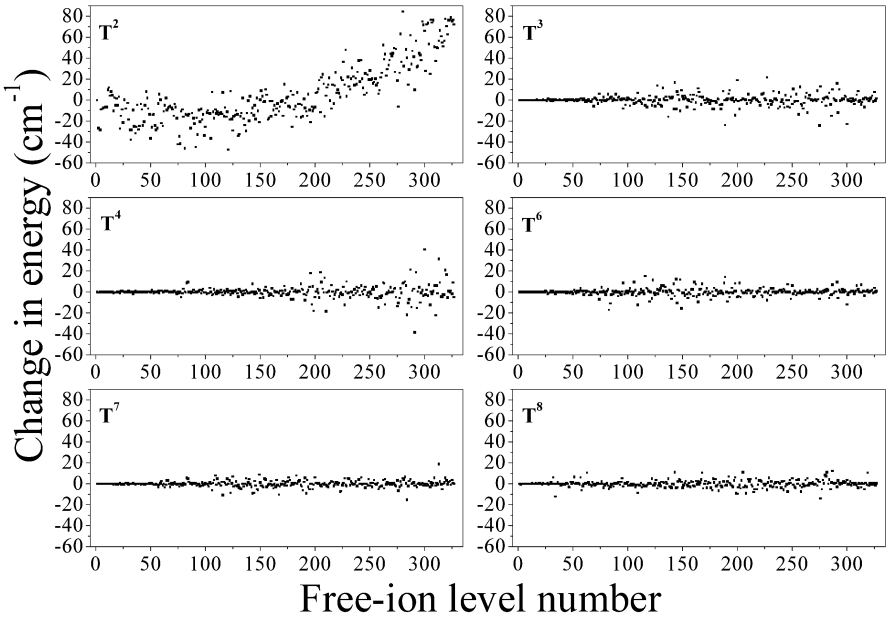

Figure 4.14: Changes in energy of the free–ion levels calculated for an increase of 20 cm^{-1} for the three–body interaction parameters T^2 to T^8. All vertical scales are set to the same energy range.

The higher order magnetic interaction parameters M and P were always allowed to vary. The M^2 and M^4 were kept at fixed ratios of 0.56 and 0.31 to M^0, the same was done with P^4 and P^6 with respect to P^2 with ratios of 0.5 and 0.1, respectively [2].

For the crystal field parameters B_q^k (in Wybourne normalization) the values of k are restricted to 2, 4 and 6 for 4f–electron configurations. For C_{2v}, which is the effective site symmetry used for LaF_3, the restrictions for q are: q = even and $0 \leq q \leq k$. Besides this one–electron crystal field interaction we also included two–electron correlation crystal field parameters D_q^k. It is known for certain lanthanide ions like Pr^{3+} that the one-electron crystal field parametrization gives an accurate description of the crystal field levels for most multiplets, but not for all of them [17]. The inclusion of two–electron correlated crystal field interaction was shown to improve the calculated splitting of the anomalously behaving multiplets [18]. We included the delta-function correlated crystal field parameters D_q^k for k = 2, 4 and 6 using the delta functions as reported by Lo and Reid [19].

Therefore, not all parameters were allowed to vary at the same time. In fact, without putting any restraints to the values of certain parameters the resulting set of parameter val-

ues will give the best agreement between calculation and experiment. This set, however, contains parameter values that have the wrong sign or order of magnitude and therefore has lost its physical meaning. Initially, only the free–ion parameters were allowed to vary and the crystal field parameters were set to the values listed in 4.4 which were obtained by fitting to the energy levels up to 50 000 cm^{-1} reported by Carnall *et al.* [2]. The new set of free–ion parameters thus obtained was used as a basis for a second fitting procedure in which the crystal field parameters were varied. Finally, a fit in which all parameters were allowed to vary freely (except T^3 to T^8 which were fixed and M^2, M^4, P^4 and P^6 set to the ratios mentioned above), was performed.

Table 4.9: Free–ion and crystal-field parameters for LaF_3:Gd^{3+}. Parameters for which no uncertainty is given were not varied. The number of data N, standard deviation σ and root mean square deviation are given at the bottom of the table.

Parameter	All data Value (cm^{-1})	Carnall's data Value (cm^{-1})	Present data Value (cm^{-1})
E_{AVG}	88025(7)	87812(10)	87989(5)
F^2	86065(67)	85592(18)	85798(82)
F^4	61499(95)	61015(29)	61529(103)
F^6	44832(116)	44745(25)	44633(137)
α	19.33(0.17)	19.13(0.09)	18.97(0.19)
β	-528(26)	–600	–520(23)
γ	1450(24)	1575	1490(23)
T^2	263(19)	300	288
T^3	42	42	42
T^4	62	62	62
T^6	–295	–295	–295
T^7	350	350	350
T^8	310	310	310
ζ	1516(2)	1499(2)	1517(2)
M^0	2.85(0.12)	3.20(0.03)	2.75(0.29)
P^2	538(37)	676	520(51)
B^2_0	–223(36)	–212(14)	–198(32)
B^4_0	622(171)	579(40)	909(96)
B^6_0	441(143)	292(22)	143(89)
B^2_2	–92(27)	0.4286 B^2_0	–117(19)
B^4_2	217(93)	0.5629 B^4_0	193(82)
B^4_4	556(95)	0.7483 B^4_0	343(88)
B^6_2	–720(89)	-2.575 B^6_0	–891(60)
B^6_4	–331(86)	-0.7286 B^6_0	–153(89)
B^6_6	–598(103)	-1.8179 B^6_0	–520(87)
D^2_0	1.02(0.88)		1.29(1.57)
D^4_0	–3.01(0.93)		–2.53(0.98)
D^6_0	–0.46(0.55)		–0.22(0.45)
N	133	70	83
σ	16.1	8.0	11.2
r.m.s.	14.6	7.4	10.1

On the basis of the newly observed energy levels in the VUV two fittings were done following the strategy discussed above, in addition to the fit based on the UV energy levels reported by Carnall. The resulting sets of parameters and their uncertainties are collected in table 4.9. In the first column the parameters are given based on fitting all 133 experimentally observed levels. The levels included are the levels up to 49 000 cm^{-1} as reported by Carnall [2] and the presently reported VUV energy levels. The quality of the fit is reflected by the standard deviation σ (16 cm^{-1}) and root mean square deviation r.m.s. (14.6 cm^{-1}). The second column gives the parameters obtained for the best fit for the lower energy levels (up to 49 000 cm^{-1}) while the third column contains the values for the parameters obtained by fitting the high energy (VUV) levels.

The quality of the fits for either the higher energy levels or the lower energy levels is very good which is demonstrated by the small root mean square deviation and standard deviation for these fits (around 10 cm^{-1}). For the fit including all energy levels the agreement is not as good which is not only clear from the higher numbers for σ and r.m.s. but also from the fact that the ground state is calculated at –108 cm^{-1} with the parameters in the first column in table 4.9. The origin for the discrepancy between the parameters obtained from fitting the experimentally observed energy levels in the two spectral regions is not clear. Calibration errors of the experimental set-ups can be excluded. With the dye laser used here for measuring the VUV energy levels of Gd^{3+} by excited state absorption we also measured the UV levels for Gd^{3+} in LaF_3 using one–photon and two–photon excitation. Our experiments give energies for the UV levels that agree within approximately 1 cm^{-1} with the values found by Carnall [2] and also with the energies reported by Downer obtained by two–photon experiments on LaF_3:Gd^{3+} [3].

At this point it is only possible to speculate about the origin of the discrepancy. Possibly the strong intermixing of states in the VUV region, where there is an overlap between many closely spaced multiplets, is not well reproduced by the presently used model and further refinement of the model is required. This may also explain some of the differences observed between the calculated and experimentally observed intensities for transitions in the VUV (see figures 4.11 and 4.12).

In appendix A all experimental results are tabulated and compared with values calculated for the UV and VUV energy levels from the parameters given in second and third column of table 4.9, respectively. The experimental energies between brackets were used for the calculations resulting in the parameters given in the second column of table 4.9 while the other data (energies of VUV levels) were used for the calculation resulting in the parameters given in the third column of table 4.9, except for the energies listed in parentheses, which were not included in the fitting procedure. In the column $\Delta 1$ the energy difference between the calculated and observed energies is given for the fit based on the VUV data while the column $\Delta 2$ gives the difference with the energies calculated with the parameters obtained from fitting the UV energy levels. The results show that

the parameters obtained from the fit to the data reported by Carnall result is large energy differences between the calculated and observed energies for the levels in the VUV. The energy differences $\Delta 2$ increase from about 100 cm^{-1} for the levels around 50 000 cm^{-1} to 180 cm^{-1} for the highest energy levels observed. The agreement between the calculated VUV energy levels and the experimentally observed energies is good when the parameters from the new fit are used. In figure 4.15 this is illustrated. In this figure the calculated energy level scheme for Gd^{3+} in LaF_3 is shown for both sets of parameters together with all experimentally observed energy levels, including the energy levels that have not been used in the fitting of the parameters. The agreement between the experimentally observed levels and the energy level structure calculated with the new set of fitting parameters (given in the third column of table 4.9) is very good while the energy level structure based on calculations with the parameters from fitting of the data reported by Carnall (given in the second column of table 4.9) cannot explain the observed energy level structure. Note that some of the calculated energy levels in the energy level diagram based on the new parameters are not experimentally observed. The reason for the absence in the experimental spectra is that the excited state absorption transitions to these levels is forbidden due to selection rules. For example, since transitions to levels with J-values higher than 19/2 are formally forbidden the energy levels that are calculated in the energy region around 57 700 and 60 400 cm^{-1} are not observed in the experiment.

4.6 Conclusions

Two–photon excitation and excited state absorption techniques have been used to probe high energy levels of the trivalent gadolinium ion with a high resolution. The ^6I_J levels were measured successfully: 36 of the expected 39 levels were observed. Two–photon excitation was not successful for probing the ^6G_J levels and higher levels of Gd^{3+} due to interference from impurities and possibly due to low oscillator strengths.

Excited state absorption proved to be a promising method to measure the energy levels of Gd^{3+} in LaF_3 up to 62 000 cm^{-1} with a resolution of $\sim$1 cm^{-1}. The energy levels measured were successfully used as a basis for the determination of more accurate parameters used for an energy level calculation of Gd^{3+} in LaF_3 that shows a root mean square deviation of 10 cm^{-1} for the energy levels in the VUV region.

It was not possible to obtain a parameter set that shows a good agreement for both the lower levels up to 50 000 cm^{-1} and our experimentally obtained VUV levels. Intensity calculations showed a good agreement for most absorptions, but for some absorptions there are differences between calculated and observed intensities. The inability of the calculations to reproduce the energy level structure and line intensities for the full spectral region in good agreement with experiment may be related to the strong overlap and intermixing of states in areas where the energy levels are closely spaced. Further improve-

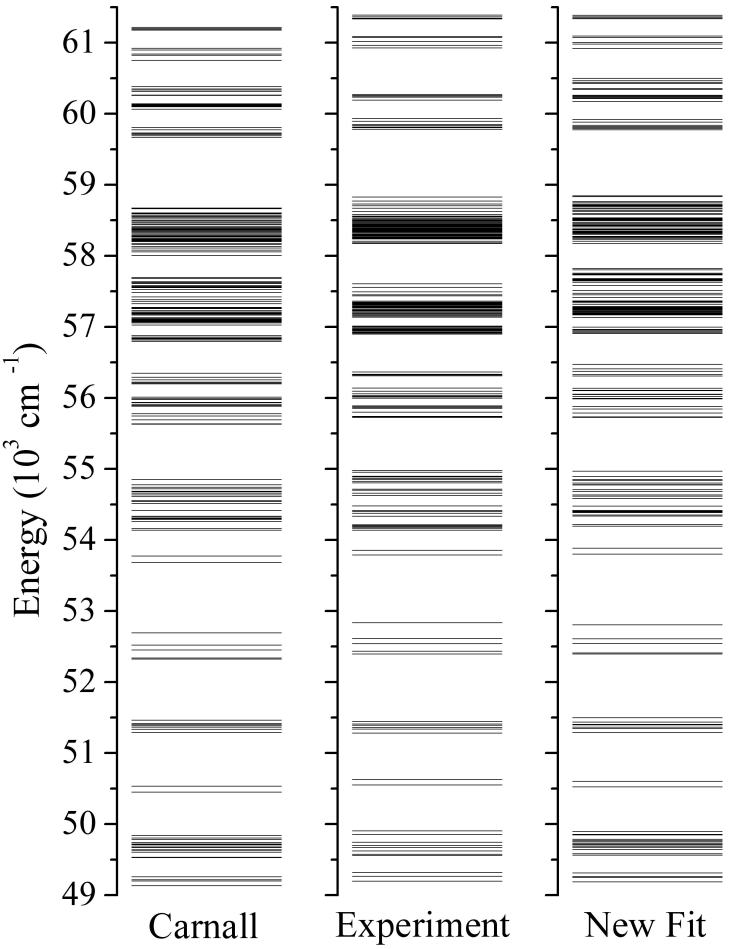

Figure 4.15: Calculated and experimentally observed energy levels for Gd^{3+} in LaF_3 using excited state absorption. The left column shows the energies calculated using the parameters published by Carnall [2], the middle column displays all experimentally observed energy levels and the right column shows the energy level diagram with the newly fit parameters.

ments in the energy level calculation model may resolve this issue.

References

[1] G. H. Dieke, *Spectra and energy levels of rare earth ions in crystals*, Interscience Publishers, New York (1968).

[2] W. T. Carnall, G. L. Goodman, K. Rajnak and R. S. Rana, *A Systematic Analysis of the Spectra of the Lanthanides Doped into Single Crystal LaF_3* Argonne National Laboratory, Argonne Illinois (1988).

[3] M. Dagenais, M. Downer, R. Neumann and N. Bloembergen, *Phys. Rev. Lett.* **46** (1981), 561.

[4] P. A. Tanner, V. V. Ravi Kanth Kumar, C. K. Jayasankar and M. F. Reid, *J. Alloys Comp.* **215** (1994), 349.

[5] K. A. Schoene, J. R. Quagliano and F. S. Richardson, *Inorg. Chem.* **30** (1991), 3803.

[6] J. Hölsä, R. J. Lamminmäki, M. Lastusaari and P. Porcher, *J. Alloys Comps.* **323-324** (2001), 811.

[7] R. T. Wegh, H. Donker, A. Meijerink, R. J. Lamminmäki and J. Hölsä, *Phys. Rev. B* **56** (1997), 13841.

[8] R. T. Wegh, A. Meijerink, R. J. Lamminmäki and J. Hölsä, *J. Lumin.* **87-89** (2000), 1002.

[9] R. T. Wegh, E. V. D. van Loef, G. W. Burdick and A. Meijerink, *Mol. Phys.* **101** (2003), 1047.

[10] P. S. Peijzel, R. T. Wegh, A. Meijerink, J. Hölsä and R. J. Lamminmäki, *Optics Communications* **204** (2002), 195.

[11] M. Göppert-Mayer, *Anw. Phys.* **9** (1931), 273.

[12] B. Henderson and G. F. Imbush, *Optical Spectroscopy of Inorganic Solids*, Clarendon Press: Oxford (1989).

[13] J. H. van Vleck, *J. Chem. Phys.* **41** (1937), 67.

[14] J. D. Axe, *Phys. Rev. A* **136** (1964), 42.

[15] W. Kaiser and C. G. B. Garrett, *Phys. Rev. Lett.* **7** (1961), 229.

[16] M. C. Downer and A. Bivas, *Phys. Rev. B.* **28** (1983), 3677.

[17] Y. Y. Yeung and D. J. Newman, *J. Chem. Phys.* **86** (1987), 6717.

[18] G. W. Burdick and F. S. Richardson, *Chem. Phys.* **228** (1998), 81.

[19] T. S. Lo and M. F. Reid, *J. Alloys Comps.* **193** (1993), 180.

Chapter 5

$4f^{n-1}5d \rightarrow 4f^n$ emission of Ce^{3+}, Pr^{3+}, Nd^{3+}, Er^{3+} and Tm^{3+} in $LiYF_4$ and YPO_4

This chapter describes the experimental and calculated $4f^{n-1}5d \rightarrow 4f^n$ emission spectra of Ce^{3+}, Pr^{3+}, Nd^{3+}, Er^{3+} and Tm^{3+} in $LiYF_4$ and YPO_4 host lattices. The positions and intensities of the zero–phonon lines were calculated and compared to the high–resolution emission spectra. For the thulium samples gated detection was used to distinguish between the spin–forbidden and spin–allowed $4f^{n-1}5d \rightarrow 4f^n$ emissions. Luminescence lifetimes for the spin–forbidden $4f^{n-1}5d \rightarrow 4f^n$ emissions were calculated and compared with experimentally observed lifetimes. A good agreement between experiment and theory is found, demonstrating the correctness of the model developed for the $4f^{n-1}5d$ and $4f^n$ states of lanthanide ions.

5.1 Introduction

More than a century of spectroscopy on lanthanide ions has involved detailed studies of the intraconfigurational $4f^n \leftrightarrow 4f^n$ transitions. Most of the aspects of these transitions are understood very well nowadays. Models have been developed for the energy level structure and transition probabilities and with the rapid increase of computer power it is nowadays possible to explain and predict the optical spectra of lanthanide ions. An illustrative example is presented in chapter 3 where the possibility for emission from the $^3P_2$ level of holmium was predicted on the basis of calculations before it was observed.

For interconfigurational $4f^n \leftrightarrow 4f^{n-1}5d$ transitions the situation is different. One of the reasons for this is the fact that these transitions are mainly situated in the UV and VUV region, which were studied thoroughly only during the last two decades, triggered by an increased interest in the high energy excited states of lanthanide ions. The possible application of lanthanide ions in new phosphors combined with the availability of high-intensity sources of VUV radiation like the synchrotron has greatly contributed to the knowledge of the $4f^{n-1}5d$ levels of all lanthanide ions in a number of host lattices.

Recently Van Pieterson *et al.* have shown that it is possible to calculate the energies of $4f^n \leftrightarrow 4f^{n-1}5d$ transitions using an extension of the model used for $4f^n$ levels by including crystal field and spin–orbit interactions for the 5d–electron and the Coulomb interaction between the 4f– and 5d–electrons [1, 2]. The model developed by Reid, Van Pieterson *et al.* for the energies of $4f^{n-1}5d$ states relies mainly on high resolution $4f^n \rightarrow 4f^{n-1}5d$ excitation spectra for experimental verification. Emission spectra could only be recorded with a poor spectral resolution. Recently, Zimmerer *et al.* reported a high–resolution $4f^{10}5d \rightarrow 4f^{11}$ emission band for $LiYF_4$:Er^{3+} [3].

In this chapter we report high resolution $4f^{n-1}5d \rightarrow 4f^n$ emission spectra for various lanthanide ions in $LiYF_4$ and YPO_4. This allows a more detailed study of the positions and intensities of the zero–phonon lines, together with the fine structure caused by vibronic transitions in the emission spectra. $4f^{n-1}5d \rightarrow 4f^n$ emission is expected for Ce^{3+}, Pr^{3+}, Nd^{3+}, Er^{3+} and Tm^{3+} in $LiYF_4$ and YPO_4, except for YPO_4:Tm^{3+} where the charge transfer band is situated below the $4f^{11}5d$ band. The other lanthanide ions do not show $4f^{n-1}5d \rightarrow 4f^n$ emission due to the presence of $4f^n$ levels just below the lowest $4f^{n-1}5d$ state allowing fast non–radiative decay to the $4f^n$ levels. This chapter will focus on the $4f^{n-1}5d \rightarrow 4f^n$ emission spectra of Ce^{3+}, Pr^{3+}, Nd^{3+}, Er^{3+} and Tm^{3+} in $LiYF_4$ and YPO_4. High resolution emission spectra are reported and compared with calculated spectra.

5.2 Theory

The 4f^{n-1}5d energy levels can be calculated by using an extended version of the model for the 4f^n configurations described in chapter 2. The 4f^n energy levels are calculated using a parameterized Hamiltonian that contains parameters for the electron interactions and crystal field parameters which describe the interaction of the ion and its ligands.

In short, the Hamiltonian is written as

$$\mathcal{H}(\mathrm{ff}) \;=\; \mathcal{H}_{\mathrm{A}}(\mathrm{ff}) \;+\; \mathcal{H}_{\mathrm{CF}}(\mathrm{ff}) \tag{5.1}$$

where the atomic part $\mathcal{H}_{\mathrm{A}}(\mathrm{ff})$ contains electronic interactions (Coulomb and spin-orbit). The crystal field interactions are represented by $\mathcal{H}_{\mathrm{CF}}(\mathrm{ff})$.

The full expression for $\mathcal{H}_{\mathrm{A}}(\mathrm{ff})$ is:

$$\begin{aligned}\mathcal{H}_{\mathrm{A}}(\mathrm{ff}) \;=\; & \sum_k F^k(\mathrm{ff}) f_k(\mathrm{ff}) \;+\; \zeta(\mathrm{ff}) A_{\mathrm{SO}}(\mathrm{ff}) \\ & + \alpha(\mathrm{ff}) L(L+1) \;+\; \beta(\mathrm{ff}) G(G_2) \;+\; \gamma(\mathrm{ff}) G(R_7) \\ & + \sum_i T^i(\mathrm{ff}) t_i(\mathrm{ff}) \;+\; \sum_k P^k(\mathrm{ff}) p_k(\mathrm{ff}) \\ & + \sum_j M^j(\mathrm{ff}) m_j(\mathrm{ff})\end{aligned} \tag{5.2}$$

with k = 2, 4, 6; i = 2, 3, 4, 6, 7, 8 and j = 0, 2, 4. The Coulomb interaction is parameterized by the F^k parameters. $\zeta(\mathrm{ff})$ defines the spin–orbit interaction. The two– and three–body correlations are parameterized by $\alpha(\mathrm{ff})$, $\beta(\mathrm{ff})$, $\gamma(\mathrm{ff})$ and T^i(ff). Higher order magnetic interactions are parameterized by M^j(ff) and P^k(ff).

The crystal–field splitting of the 4f^n states is determined by

$$\mathcal{H}_{\mathrm{CF}}(\mathrm{ff}) \;=\; \sum_{k,q} B_q^k(\mathrm{ff}) C_q^{(k)}(\mathrm{ff}), \tag{5.3}$$

where the $B_q^k(\mathrm{ff})$ parameters define the radially dependent part of the one–electron crystal–field interaction, and $C_q^{(k)}(\mathrm{ff})$ are the many–electron spherical tensor operators for the 4f^n configuration. For configurations concerning 4f–electrons the values of k are restricted to 2, 4 and 6. The applicable values of q depend on the site–symmetry of the lanthanide ion in the host lattice. Rare earth ions in $LiYF_4$ occupy sites with S_4 symmetry with only a small deviation from D_{2d} symmetry. D_{2d} is the exact site–symmetry for rare earth ions in YPO_4. For D_{2d} symmetry the allowed values for q are 0 and ± 4 [4].

To expand the well–known model for the calculation of 4f^n energy levels to 4f^{n-1}5d configurations the extra contributions of the d–electron have to be included [1]. These

are the spin–orbit interaction for the d–electron, the crystal–field interactions of the d–electron and the Coulomb interaction between the 4f–electron and the 5d–electron. The addition to the Hamiltonian is:

$$\mathcal{H}(\mathrm{fd}) \;=\; \mathcal{H}_A(\mathrm{fd}) \;+\; \mathcal{H}_\mathrm{A}(\mathrm{dd}) \;+\; \mathcal{H}_\mathrm{CF}(\mathrm{dd}) \tag{5.4}$$

The atomic Hamiltonian is written as:

$$\mathcal{H}_\mathrm{A}(\mathrm{fd}) \;=\; \Delta_\mathrm{E}(\mathrm{fd}) \;+\; \sum_k F^k(\mathrm{fd}) f_k(\mathrm{fd}) + \sum_j G^j(\mathrm{fd}) g_j(\mathrm{fd}) \tag{5.5}$$

$$\mathcal{H}_\mathrm{A}(\mathrm{dd}) \;=\; \zeta_\mathrm{SO}(\mathrm{dd}) A_\mathrm{SO}(\mathrm{dd}) \tag{5.6}$$

with k = 2 and 4, j = 1, 3 and 5. $F^k(\mathrm{fd})$ and $G^i(\mathrm{fd})$ are the direct and exchange Slater parameters for the Coulomb interaction between the d–electron and the 4f–electrons. $\zeta_\mathrm{SO}(\mathrm{dd})$ represents the spin–orbit interaction for the 5d–electron.

The 5d–levels are also split by the crystal field. This is parameterized by $\mathcal{H}_\mathrm{CF}(\mathrm{dd})$:

$$\mathcal{H}_\mathrm{CF}(\mathrm{dd}) \;=\; \sum_{k,q} B^k_q(\mathrm{dd}) C^{(k)}_q(\mathrm{dd}) \tag{5.7}$$

where k is limited to 2 and 4, while q can be 0 or ± 4 for $\mathrm{D_{2d}}$ symmetry.

The term $\Delta_\mathrm{E}(\mathrm{fd})$ defines the energy difference between the $4f^n$ ground state and the barycenter of the $4f^{n-1}5d$ excited state. Adjusting this value does not influence the splitting of the 5d–levels, it shifts them all by the same energy.

Emissions from the $4f^{n-1}5d$ excited state to the $4f^n$ ground states are allowed electric dipole transitions and it is possible to calculate the matrix elements of the electric dipole operator for these transitions. Electrons in 5d–orbitals do participate in the chemical bond between the lanthanide ion and its ligands. As a result, $4f^n \leftrightarrow 4f^{n-1}5d$ transitions are characterized by a much stronger electron–phonon coupling than $4f^n \leftrightarrow 4f^n$ transitions. Typical Huang–Rhys factors for $4f^n \leftrightarrow 4f^{n-1}5d$ transitions range from 1.5 to 5. This causes most of the intensity to show up in the vibronic bands of the emission spectra. In our model a Gaussian shape of the vibronic band is assumed, due to the superposition of coupling with several vibrational modes. The energy level calculations provide the positions of the zero–phonon lines of the emissions and Gaussian shaped bands are superimposed on those lines. The energy difference between the zero–phonon line and the maximum of the Gaussian band can be estimated from the cerium excitation spectrum [1].

The radiative transition probability from the initial state $\nu\Gamma_\mathrm{fd}$ to the final state $\nu'\Gamma_\mathrm{f}$ is given by [5]

$$A(\mathrm{ED}) \;=\; \frac{1}{4\pi\epsilon_0}\;\frac{4n\omega^3}{3\hbar c^3}\;\left(\frac{E_\mathrm{loc}}{E}\right)^2\;\frac{1}{g_\mathrm{fd}}\;S_\mathrm{tot}(\nu\Gamma_\mathrm{fd}\nu'\Gamma_\mathrm{f}). \tag{5.8}$$

In this equation ϵ_0 is the vacuum permittivity, n is the refractive index, ω is the angular frequency of the emission, $(E_{\rm loc}/E)^2$ is the local field correction and $g_{\rm fd}$ is the degeneracy of the excited state. We used a refractive index of 1.46 for $LiYF_4$ and 1.75 for YPO_4 which is a good approximation for the average value of n in the wavelength region of the emissions studied [6]. The local field correction is given by $\left((n^2+2)/3\right)^2$ [7]. The total electric dipole strength $S_{\rm tot}$ is the sum of its components:

$$S_{\rm tot} \;=\; S_x + S_y + S_z, \tag{5.9}$$

where

$$\begin{aligned} S_{x,y} \;&=\; \sum_{\gamma_{\rm f},\gamma_{\rm fd}} \frac{1}{2} |\left\langle \nu' \Gamma_{\rm f} \gamma_{\rm f} | erC^1_{-1} | \nu \Gamma_{\rm fd} \gamma_{\rm fd} \right\rangle \\ &\quad \pm \left\langle \nu' \Gamma_{\rm f} \gamma_{\rm f} | erC^1_{1} | \nu \Gamma_{\rm fd} \gamma_{\rm fd} \right\rangle |^2, \end{aligned} \tag{5.10}$$

$$S_z \;=\; \sum_{\gamma_f,\gamma_{\rm fd}} \left|\left\langle \nu' \Gamma_{\rm f} \gamma_{\rm f} | erC^1_{0} | \nu \Gamma_{\rm fd} \gamma_{\rm fd} \right\rangle\right|^2 . \tag{5.11}$$

The summation in equations 5.10 and 5.11 is over the squared transition dipole moments from the excited states $\nu\Gamma_{\rm fd}$ to the final states $\nu'\Gamma_{\rm f}$. C^1_q is a spherical tensor operator as defined in Refs. [8] and [9]. The lifetime of the emissions was calculated by taking the inverse of the spontaneous transition probability $A(\mathrm{ED})$. Radial integrals $\langle 5\mathrm{d}|r|4\mathrm{f}\rangle$ were calculated using Cowans program [8] and are included in table 5.3.

5.3 Experimental

Microcrystalline powders of YPO_4 doped with 1% RE^{3+} (RE = Ce, Pr, Nd, Er, Tm) were prepared by firing a mixture of Y_2O_3 (4N), the corresponding RE_2O_3 (4N) and $(NH_4)_2HPO_4$ in air at 1350°C for three hours. A YPO_4 crystal doped with 2% of Nd^{3+} was kindly provided by dr. L. Boatner from Oak Ridge National Laboratory. A microcrystalline powder of $LiYF_4$ doped with 0.1% Pr^{3+} was prepared by firing a mixture of YF_3, LiF and PrF_3 in stoichiometric ratios (with a 10% excess of LiF) in a flow of ultrapure nitrogen at 600°C.

$LiYF_4$ single crystals containing 1 to 4% of RE ions were grown using a Philips PH 1006/13 high frequency furnace with LiF, YF_3 and REF_3 as the starting compounds. The crystal growth melt contained a 15% excess of LiF. The reactants were mixed and transferred to a vitreous carbon crucible. In order to remove water and oxygen the sample was heated overnight at 300°C in a flow of ultrapure nitrogen. Subsequently the temperature was raised to 550°C and SF_6 was introduced in the reaction chamber for 30 minutes to remove the last traces of water and oxygen. During the rest of the synthesis a nitrogen

atmosphere was maintained. The sample was heated until melting was observed. Next, the sample was cooled to room temperature in 10 hours.

Both the $LiYF_4$ and YPO_4 samples were checked for phase purity by recording a powder diffractogram using a Philips PW1729 X-ray diffractometer using CuK_α radiation. All samples were single phase.

Emission measurements were performed at liquid helium temperatures using a cold–finger type Oxford Instruments liquid helium flow cryostat, equipped with MgF_2 windows. The excitation source consisted of a TuiLaser ExciStar S–200 F_2 laser producing 1 mJ pulses of a approximately 10 nanoseconds at 157 nm using fluorine and 10mJ pulses at 193 nm using an argon/fluorine mixture, both with a repetition rate of 100 Hz. Emission spectra were recorded using a 0.55 m Jobin Yvon TRIAX 550 monochromator with a 3600 lines/mm grating blazed for the VUV. The emission was detected using a Hamamatsu R166UHP or R7154 solar blind photo multiplier tube for the VUV and UV emissions up to 300 nm. Emission between 300 and 700 nm was detected using a Hamamatsu R928 photomultiplier tube, in combination with a 1200 lines/mm grating blazed at 400 nm. For the emission spectra of thulium–doped samples gated detection was performed using a Stanford Research SR400 boxcar averager. Luminescence lifetime measurements were performed using a Tectronix 2440 digital oscilloscope.

5.4 Results and Discussion

5.4.1 Parameter values

The zero–phonon lines in the $4f^{n-1}5d \rightarrow 4f^n$ emission spectra originate from transitions from the lowest $4f^{n-1}5d$ state to the different crystal field levels of the $4f^n$ final levels. For every zero–phonon line a vibronic side band with fine structure is present. In order to have a better agreement between the measured and calculated splitting of the $4f^n$ multiplets, we refitted the parameter values for the calculation of the $4f^n$ levels to the experimental values for the energy levels reported for Pr^{3+} [10, 11], Nd^{3+} [11, 12], Er^{3+} [13, 14] and Tm^{3+} [15] in $LiYF_4$ and YPO_4. Due to the continuous improvements in the model and computer programs for the energy level calculations it is possible to obtain a significantly better agreement between the calculated and observed energy levels than with the parameter values reported previously [10–15]. Since the positions of the zero–phonon lines depend strongly on the positions of the $4f^n$ final states, the use of better parameter values gives a better agreement between the calculated and experimentally observed $4f^{n-1}5d \rightarrow 4f^n$ emission spectra. The improved values for the fitting parameters are summarized in table 5.1. Parameters that were kept fixed in the fitting procedure are indicated in brackets. For Pr^{3+} and Nd^{3+} in $LiYF_4$ and Er^{3+} in both $LiYF_4$ and YPO_4 correlated crystal field interaction was also taken into account since it helped to improve the quality

of the fit. For other cases the inclusion of correlated crystal field parameters did not help and no values for the correlated crystal field parameters are included in table 5.1.

As far as we know, the crystal field levels of the $^2F_{5/2}$ and $^2F_{7/2}$ states of Ce^{3+} in $LiYF_4$ are not reported in the literature. Using the high resolution $4f^{n-1}5d \rightarrow 4f^n$ emission spectrum (see next section), five of the seven crystal field levels could be determined and were used to fit new parameter values. In this fit the value of ζ(dd) was kept fixed at the free–ion value of 1082 and the crystal field splitting of the d–levels was taken from the excitation spectrum reported by van Pieterson [16].

Table 5.1: Parameter values (in cm^{-1}) used for the $4f^n$ energy level calculation of Ce^{3+}, Pr^{3+}, Nd^{3+}, Er^{3+} and Tm^{3+} in $LiYF_4$ and YPO_4. Parameters that were not varied are listed in brackets.

	Ce^{3+}	Pr^{3+}		Nd^{3+}		Er^{3+}		Tm^{3+}
	$LiYF_4$	$LiYF_4$	YPO_4	$LiYF_4$	YPO_4	$LiYF_4$	YPO_4	$LiYF_4$
E_{AVG}	1517	10204	9999	24413	24105	35806	35569	18022
F^2(ff)		69025	67991	72667	71872	97449	96567	102215
F^4(ff)		50580	50031	52737	51793	68539	68144	72060
F^6(ff)		33326	32961	35817	35591	56051	53393	51366
α(ff)		[23.00]	21.30	21.49	19.87	18.27	19.97	18.20
β(ff)		–649	–683	–585	–606	[–580]	[–632]	–686
γ(ff)		[1371]	[1371]	1424	1445	[1416]	[1800]	[1820]
T^2(ff)				331	[298]	[486]	[400]	[400][1]
T^3(ff)				43	[35]	[43]	[43]	[43][1]
T^4(ff)				84	[59]	[81]	[73]	[73][1]
T^6(ff)				–324	[–285]	[–327]	[–271]	[–271][1]
T^7(ff)				387	[332]	[300]	[308]	[308][1]
T^8(ff)				322	[305]	[346]	[299]	[299][1]
ζ(ff)	628	750.1	742.1	870.1	876.3	2374	2364	2633
B^2_0(ff)	316	541	73	400	329	306	210	354
B^4_0(ff)	[–1150]	–1093	324	–1122	273	–581	81	–631
B^4_4(ff)	–1264	–1327	–856	–1272	–758	–917	–670	–851
B^6_0(ff)	[–89]	–45	–1278	–28	–1226	–6	–704	–171
B^6_4(ff)	–821	–1165	7	–1093	–89	–637	–61	–627
M_0(ff)[2]		[2.00]	0.99	0.66	2.11	3.91	5.48	4.67
P_2(ff)[3]		215	220	162	284	579	802	720
D^2(ff)		–15.9		4.9		5.3		
D^4(ff)		8.8		10.1		4.0	–1.02	

[1] Only for the excited $4f^{11}5d$ configuration

[2] M_2 and M_4 parameter values were included with the ratios $M_2/M_0 = 0.56$ and $M_4/M_0 = 0.31$

[3] P_4 and P_6 parameter values were included with the ratios $P_4/P_2 = 0.5$ and $P_6/P_2 = 0.1$

Table 5.2: Parameter values (in cm^{-1}) used for the $4f^{n-1}5d$ energy level calculation of Ce^{3+}, Pr^{3+}, Nd^{3+}, Er^{3+} and Tm^{3+} in $LiYF_4$ and YPO_4.

	Ce^{3+}	Pr^{3+}		Nd^{3+}		Er^{3+}		Tm^{3+}
	$LiYF_4$	$LiYF_4$	YPO_4	$LiYF_4$	YPO_4	$LiYF_4$	YPO_4	$LiYF_4$
Δ_E(fd)	43773	50966	47021	56684	52772	89762	86822	94218
F^2(fd)		22703	22703	22543	22543	19724	19724	19639
F^4(fd)		11321	11321	11188	11188	9358	9358	9275
F^6(fd)		9677	9677	9608	9608	8038	8038	7991
G^3(fd)		8370	8370	8284	8284	6848	6848	6789
G^5(fd)		6518	6518	6442	6442	5292	5292	5240
ζ(dd)	[1082]	1149	1188	1216	1257	1768	1821	1839
B_0^2(dd)	4673	4626	4763	4598	4734	4290	4417	4252
B_0^4(dd)	–18649	–18463	2221	–18351	2208	–17120	2060	–16971
B_4^4(dd)	–23871	–23632	–22568	–23489	–22431	–21914	–20927	–21723

The parameter values for the calculation of the excited $4f^{n-1}5d$ configurations are listed in table 5.2. The f–d Coulomb interaction parameters F^k(fd) and G^j(fd) are the values reported by Cowan [8] reduced to 75% for Pr^{3+} and Nd^{3+} and reduced to 67% for Er^{3+} and Tm^{3+} [1, 2]. The spin–orbit coupling represented by ζ(dd) and the crystal field parameters B_q^k(dd) for the $LiYF_4$ host lattice were obtained from the fit performed for Ce^{3+} by Van Pieterson [1]. For the YPO_4 host lattice the ground state levels of Ce^{3+} reported for $LuPO_4$ [18] and the 5d excited state energies reported for YPO_4 [1] were used to obtain an "exact" fit, since the number of energy levels is equal to the number of parameters varied. The 4f parameters found are similar to those reported for $LuPO_4$. The 5d parameter values are similar to the values obtained by Van Pieterson, except ζ(dd) which was kept fixed at the free–ion value of 1149 cm^{-1}, whereas we obtained a ζ(dd) of 1188 cm^{-1}.

The spin–orbit coupling and crystal field parameters used for the calculation of the $4f^{n-1}5d$ configurations for Pr^{3+}, Nd^{3+}, Er^{3+} and Tm^{3+} in $LiYF_4$ were taken from the report by Van Pieterson [19]. The parameter values for the same ions in YPO_4 were set to the ratios of the corresponding parameter values for Ce^{3+} in $LiYF_4$ and YPO_4.

The Δ_E(fd) values were adjusted to set the calculated energy of the zero–phonon line for the lowest $4f^{n-1}5d \rightarrow 4f^n$ emission equal to the experimentally observed zero–phonon line in the emission spectrum.

5.4.2 Emission spectra

Cerium

The high resolution 5d→4f emission spectrum of $LiYF_4$:Ce^{3+} 1% upon 193 nm excitation at 10 K is shown in figure 5.1. The spectrum shows two broad emission bands with the highest energy zero–phonon lines at 298.94 and 320.20 nm which corresponds to emission from the 5d level to the lowest energy crystal field components of the $^2F_{5/2}$ and $^2F_{7/2}$ states of cerium. The energy difference observed between the $^2F_{5/2}$ and $^2F_{7/2}$ levels is 2221 cm^{-1}. Figure 5.1 also shows the simulated 5d→4f emission spectrum of $LiYF_4$:Ce^{3+} based on the 5d parameters reported by Van Pieterson *et al.* [1] and the 4f parameters obtained from a fit to the positions of the $^2F_{5/2}$ and $^2F_{7/2}$ crystal field components in the measured emission spectrum. The parameter values for the calculation are listed in tables 5.1 and 5.2. Besides the zero–phonon lines the spectrum also shows some weak vibronic lines. The low intensity of the highest energy zero–phonon line in the experiment is due to resonant reabsorption of this emission.

Praseodymium

Figure 5.2 shows the calculated and the experimentally observed emission spectrum of $LiYF_4$:Pr^{3+} 0.1% upon excitation at 157 nm. The assignment of transitions is indicated in the figure. Fine structure is observed for all emission bands except for the highest energy emission. No clear vibronic progression can be observed in the emission spectrum. The intensity ratios of the emission bands are in excellent agreement with the ratios shown in the simulated spectrum. The calculated energy of the emission to the $^1G_4$ levels situated at 272 nm, however, is too low. It is known for trivalent praseodymium that the energy of the $^1G_4$ multiplet is influenced by correlated crystal field interactions if two electrons occupy the same orbital, but even with inclusion of correlated crystal field interaction the calculation model predicts the position of the $^1G_4$ at a somewhat different energy. The parameter values used for the calculation are summarized in tables 5.1 and 5.2.

Figure 5.3 shows the calculated and experimentally observed emission spectrum of YPO_4:Pr^{3+} 1% upon excitation at 157 nm. Besides sharp zero–phonon lines this spectrum also displays a clear vibronic structure on the emission bands for the transitions to the $^3H_4$, $^3H_5$ and $^3H_6$ multiplets. The parameter values used for the calculation are summarized in tables 5.1 and 5.2. The intensities of the emission bands and the relative intensities of the zero–phonon lines of the experiment is closely reproduced in the calculated spectrum. Also the positions of the zero–phonon lines are in good agreement. Clearly, the model and the parameter values for the $4f^{n-1}5d$ states and the $4f^n$ states for Pr^{3+} in YPO_4 give a good description of the actual states involved.

The main difference between the experimental and calculated spectrum is in the vibronic structure. In the model a vibronic Gaussian band is superimposed on the zero–

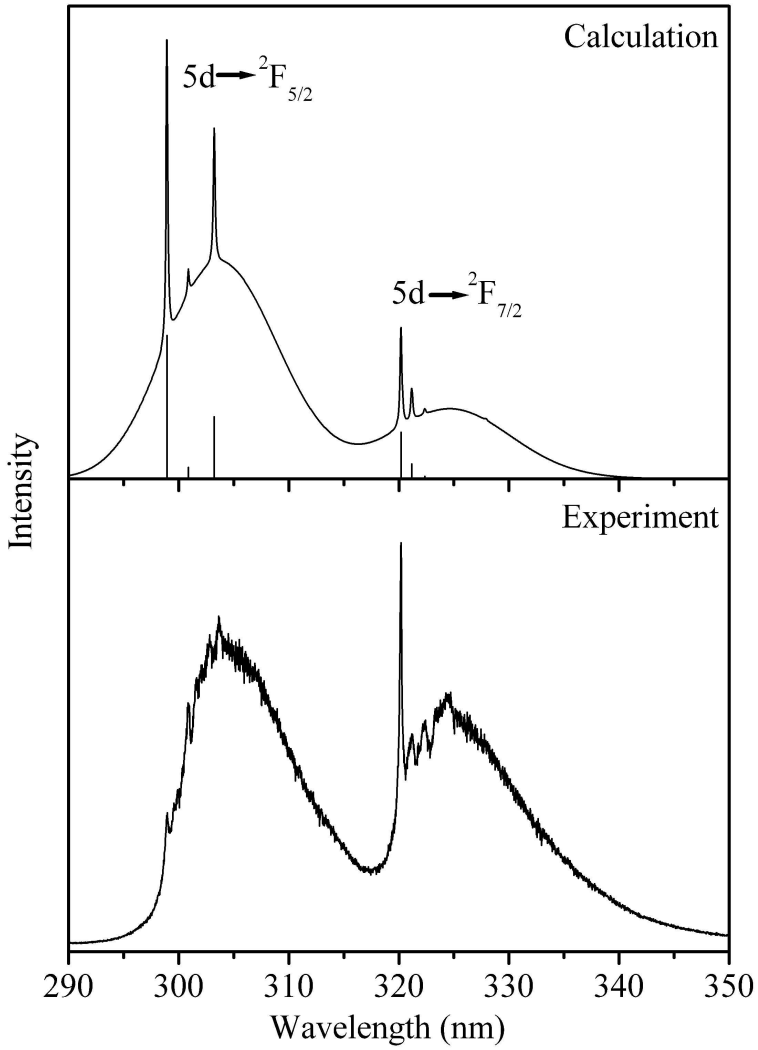

Figure 5.1: Calculated and measured emission spectrum of $LiYF_4$:Ce^{3+} 1% upon excitation at 157 nm at 10 K. In the upper spectrum the sticks give information on the positions and intensities calculated for the zero–phonon lines while the spectrum is obtained by superimposing a Gaussian band (offset 600 cm^{-1}, width 1000 wavenumbers) on the zero–phonon lines which have been given a width of 20 cm^{-1}. The same procedure is used in figures 5.2 to 5.9

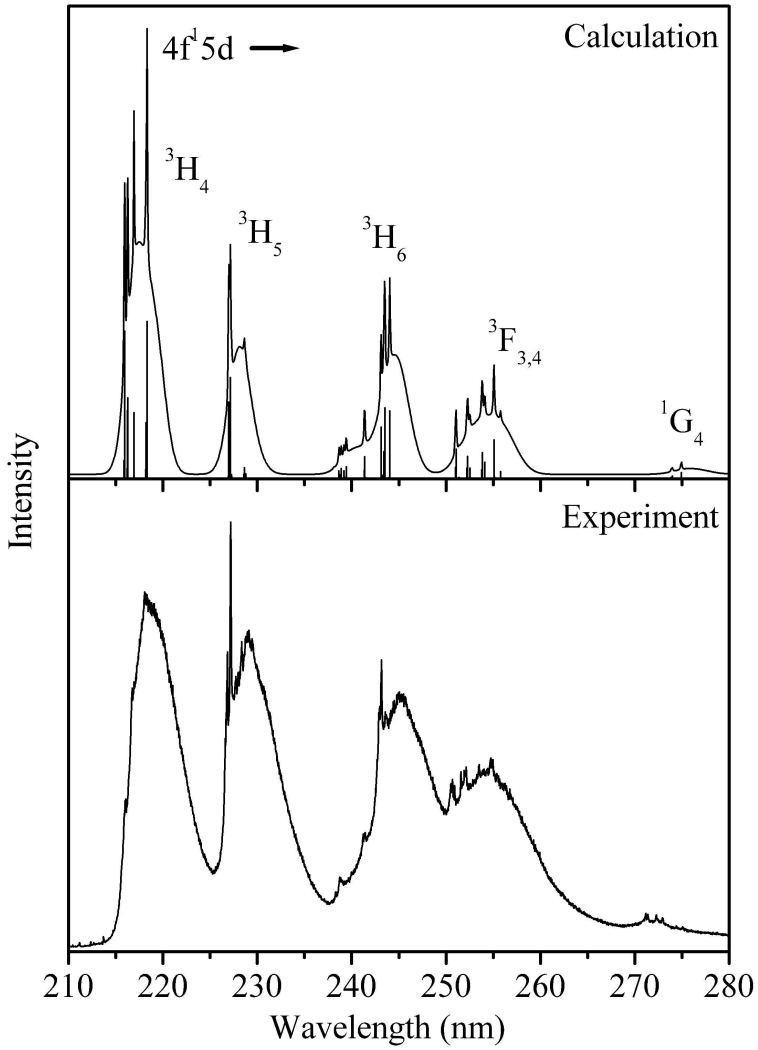

Figure 5.2: Calculated and measured emission spectrum of $LiYF_4$:Pr^{3+} 0.1% upon excitation at 157 nm at 10 K. See also figure 5.1.

phonon line. For the $4f^{n-1}5d \rightarrow 4f^n$ emission spectra for the lanthanide ions in $LiYF_4$ a broad vibronic band gives a reasonably good description since vibronic features are not clearly observed. However, in the case of YPO_4 the Huang–Rhys factor is smaller for the $4f^{n-1}5d \rightarrow 4f^n$ transitions which results in a higher relative intensity of the zero–phonon lines and the observation of sharp vibronic lines corresponding to coupling with

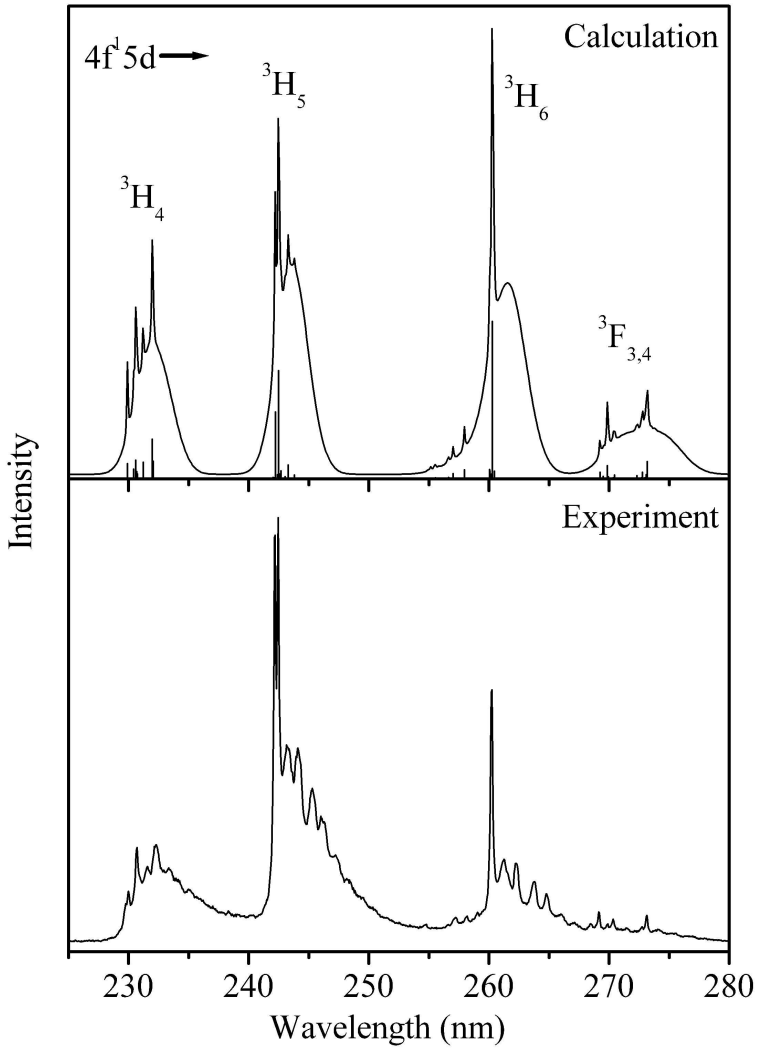

Figure 5.3: Calculated and measured emission spectrum of YPO_4:Pr^{3+} 1% upon excitation at 157 nm at 10 K. See also figure 5.1.

well–defined vibrational modes. From the analysis of the vibronic lines in figure 5.3 vibrational modes of 148 cm^{-1} and 370 cm^{-1} can be observed. A further analysis of the vibronic structure of the $4f^{n-1}5d \rightarrow 4f^n$ emission bands in YPO_4 is an interesting topic for further studies.

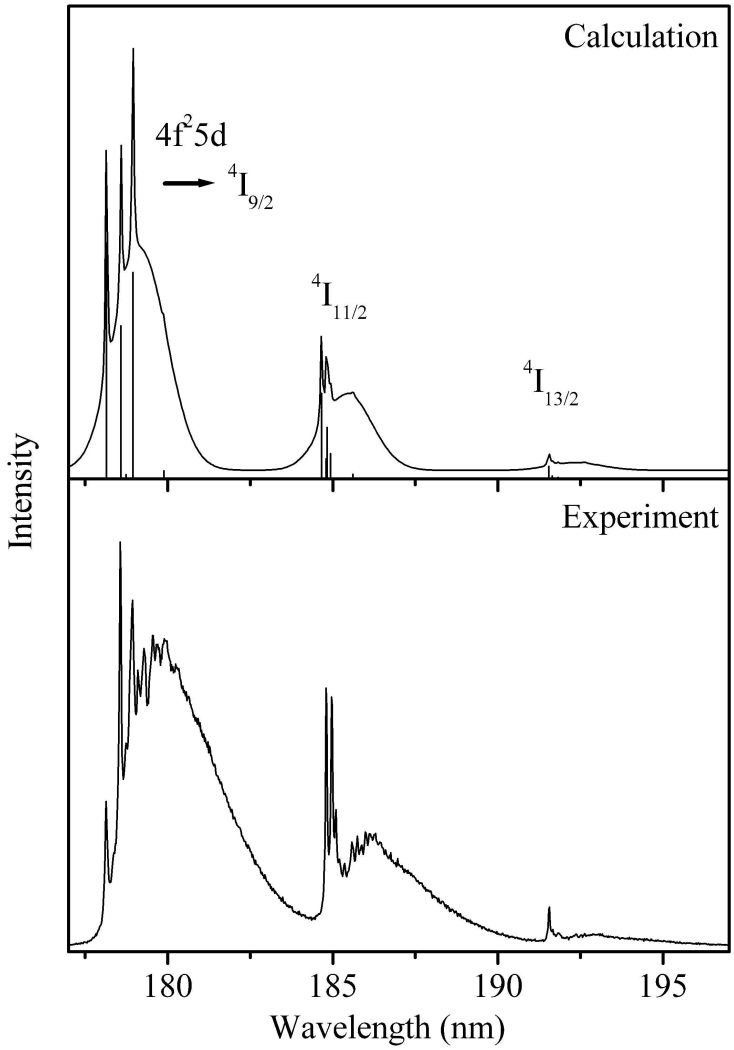

Figure 5.4: Calculated and measured emission spectrum of $LiYF_4$:Nd^{3+} 1% upon excitation at 157 nm at 10 K. See also figure 5.1.

Neodymium

The spectra depicted in figures 5.4 and 5.5 show the calculated and experimentally observed $4f^25d \rightarrow 4f^3$ emission spectrum of $LiYF_4$:Nd^{3+} and YPO_4:Nd^{3+}, respectively, upon excitation at 157 nm at 10 K. The emissions to the $^4I_{9/2}$, $^4I_{11/2}$ and $^4I_{13/2}$ levels are shown and indicated in the figures. For both $LiYF_4$:Nd^{3+} and YPO_4:Nd^{3+} the positions and in-

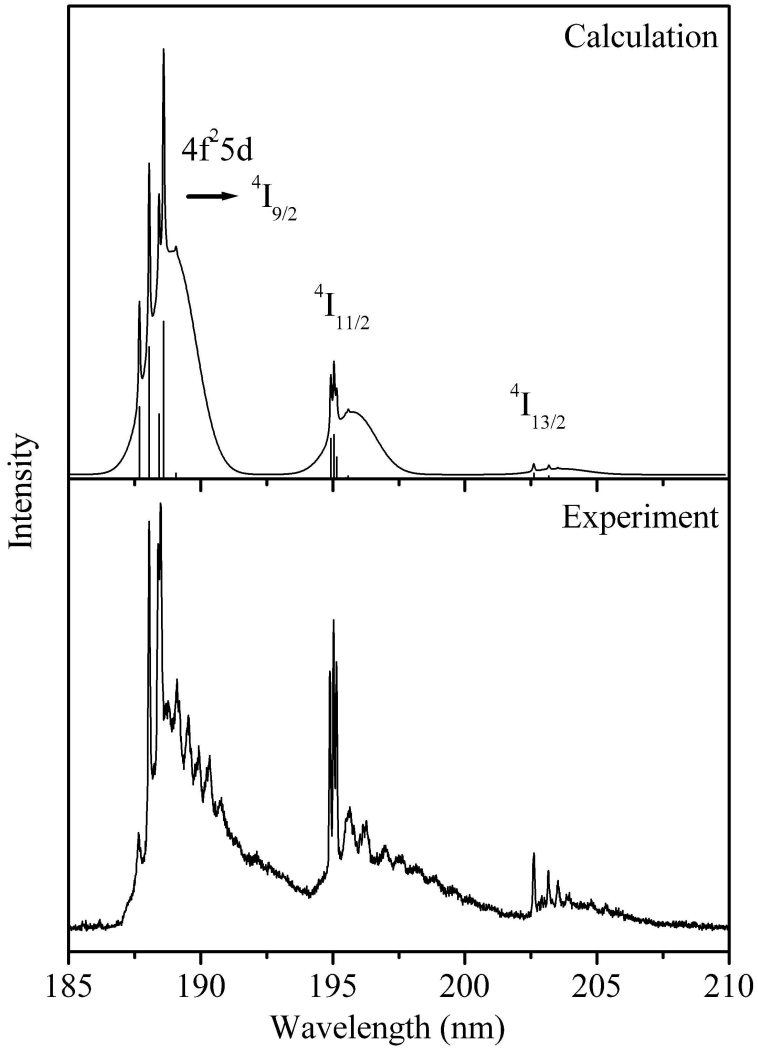

Figure 5.5: Calculated and measured emission spectrum of YPO_4:Nd^{3+} 1% upon excitation at 157 nm at 10 K. See also figure 5.1.

tensities of the zero–phonon lines in the simulated spectra are in good agreement with the experimentally obtained spectra. The highest energy zero–phonon line of the emission to the $^4I_{9/2}$ levels of both $LiYF_4$:Nd^{3+} and YPO_4:Nd^{3+} are weak due to reabsorption. In the emission spectrum of $LiYF_4$:Nd^{3+} a vibronic structure is visible, albeit weak. For YPO_4:Nd^{3+} a clear vibronic progression is observed just as for YPO_4:Pr^{3+}. Due to the

presence of many zero–phonon lines it is not possible to assign energies to vibrations unambiguously. The parameter values used for the calculations are summarized in tables 5.1 and 5.2.

Erbium

In figure 5.6 the calculated and experimentally observed emission spectrum of $LiYF_4$:Er^{3+} upon 157 nm excitation at 10 K are shown. At this excitation wavelength only the high–spin $4f^{10}5d$ state is populated (the onset of the low–spin excitation is at 155 nm [2]) and as a result only spin–forbidden emission is observed. The emission from the high–spin $4f^{10}5d$ state to the $^4I_{15/2}$ ground state is very intense compared to the emission to the $^4I_{13/2}$ level. The much higher relative intensity of the higher energy emission band is reproduced in the calculated emission spectrum. In fact, the calculated relative intensity of the emission band to the $^4I_{13/2}$ level is even weaker than in the experiment. This may be (partly) due to the fact that the emission spectra could not be corrected for the wavelength dependence of the instrumental response. Note that the observation of the weak $4f^{10}5d \rightarrow 4f^{11}(^4I_{13/2})$ emission band is hampered by the presence of emission bands around 180 nm and 185 nm due to a contamination with Nd^{3+}. The fact that these emissions show up as relatively strong bands is due to the fact that at 157 nm the Er^{3+} ion is excited in a spin–forbidden transition while the Nd^{3+} ion has a strong spin–allowed absorption band. The small relative intensity of the emission band corresponding to the $4f^{10}5d \rightarrow 4f^{11}(^4I_{13/2})$ transition can be understood on the basis of J–selection rules. Transitions with ΔJ of ± 1 are expected to have the highest transition probability for $4f^{n-1}5d \leftrightarrow 4f^n$ transitions. The lowest calculated high–spin $4f^{10}5d$ state has 89% contributions of J=17/2 states. In accordance with the ΔJ selection rule the highest emission intensity is expected for the emission to the $^4I_{15/2}$ ground state, which is observed in both the simulated and the experimental emission spectrum.

In figure 5.7 the calculated and experimentally observed emission spectrum of YPO_4 doped with Er^{3+} upon 157 nm excitation at 10 K is shown. At this excitation wavelength the low–spin $4f^{10}5d$ state is populated [2] and after relaxation to the high–spin state spin forbidden emission is observed. Just as in $LiYF_4$ the emission from the high–spin $4f^{10}5d$ state to the $^4I_{15/2}$ ground state is very intense compared to the emission to the $^4I_{13/2}$ level. The measured intensity ratio between the emissions to the $^4I_{15/2}$ and the $^4I_{13/2}$ levels differs from the calculated intensity ratio. The relative intensity of the higher energy band is expected to increase if the spectrum could be corrected for the wavelength dependence of the instrumental response resulting in a better agreement with the calculated spectrum. The parameter values used for the calculation are summarized in tables 5.1 and 5.2. The emission band at 170 nm shows a clear vibronic progression. The weak emissions at 188 nm are due to contamination of the sample with neodymium. The sharp emission lines at 184 nm are due to the intraconfigurational $4f^n\ ^2F_{7/2} \rightarrow ^4I_{15/2}$ transition of erbium. For

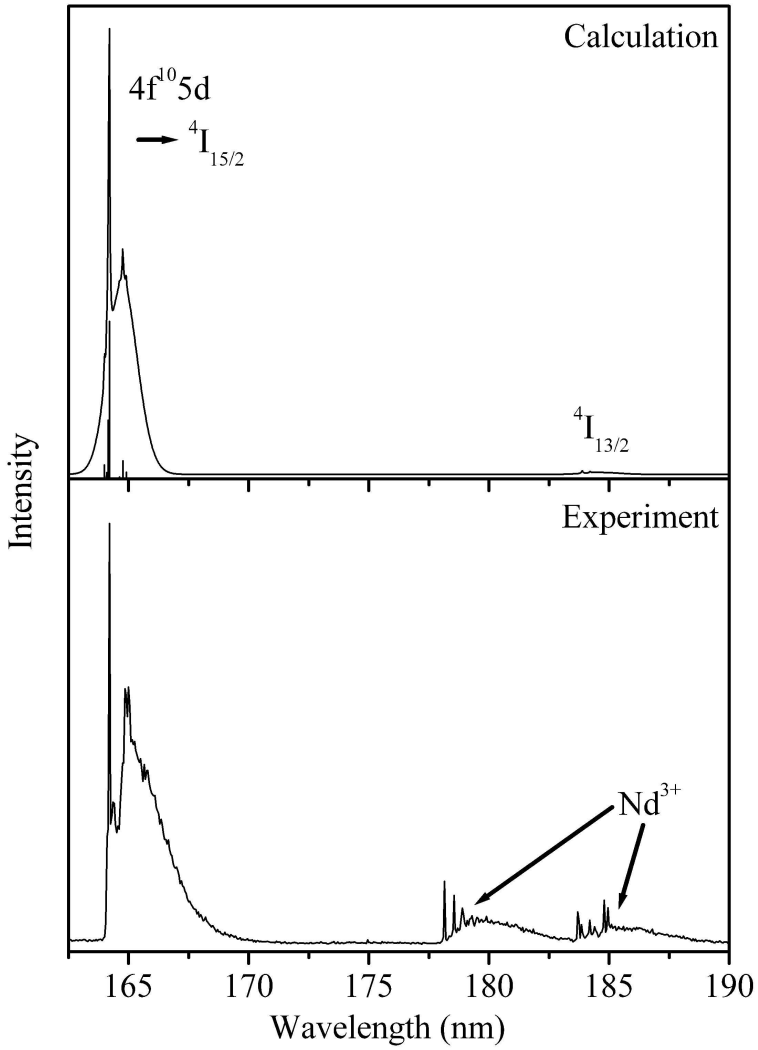

Figure 5.6: Calculated and measured emission spectrum of $LiYF_4$:Er^{3+} 1% upon excitation at 157 nm at 10 K. See also figure 5.1.

YPO_4:Er^{3+} the influence of the ΔJ selection rule is also observed. The lowest calculated high–spin $4f^{10}5d$ state has 81% contributions of J=17/2 states. According to the ΔJ selection rule the highest emission intensity is expected (and calculated) for the emission to the $^4I_{15/2}$ ground state, which is indeed observed in the spectrum.

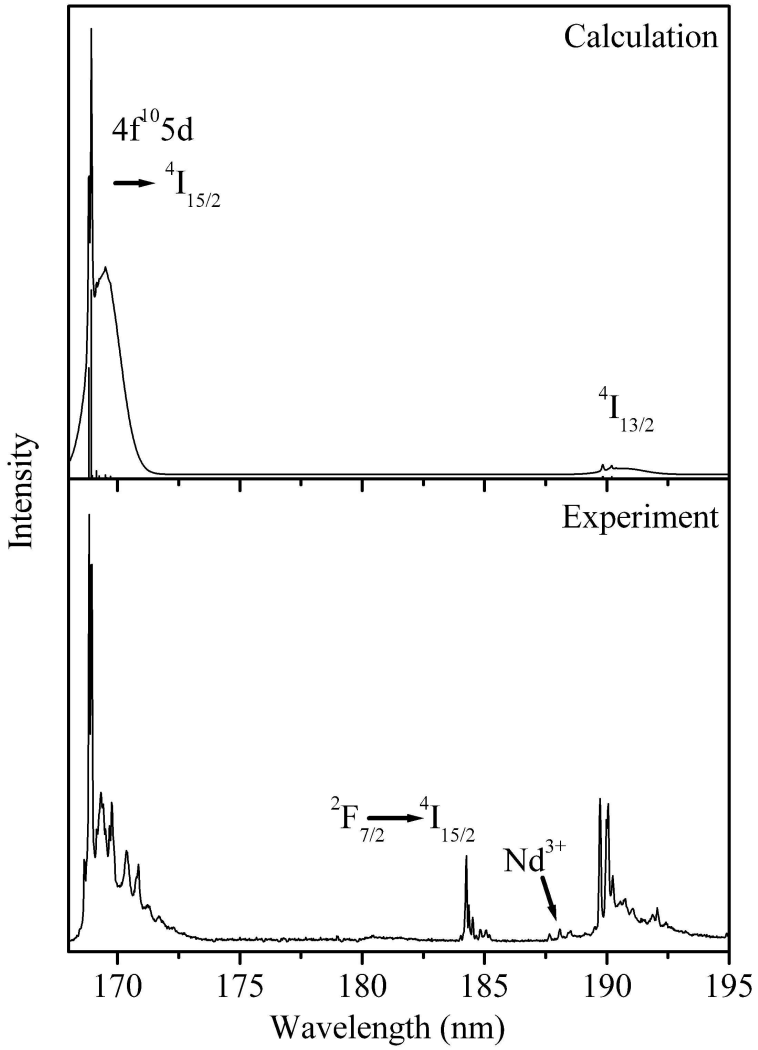

Figure 5.7: Calculated and measured emission spectrum of YPO_4:Er^{3+} 1% upon excitation at 157 nm at 10 K. See also figure 5.1.

Thulium

Figure 5.8 shows the calculated and experimentally observed emission spectrum of $LiYF_4$ doped with Tm^{3+}. Upon excitation at 157 nm emission from both the high–spin and low–spin $4f^{11}5d$ state are observed. The corresponding simulated emission spectra were

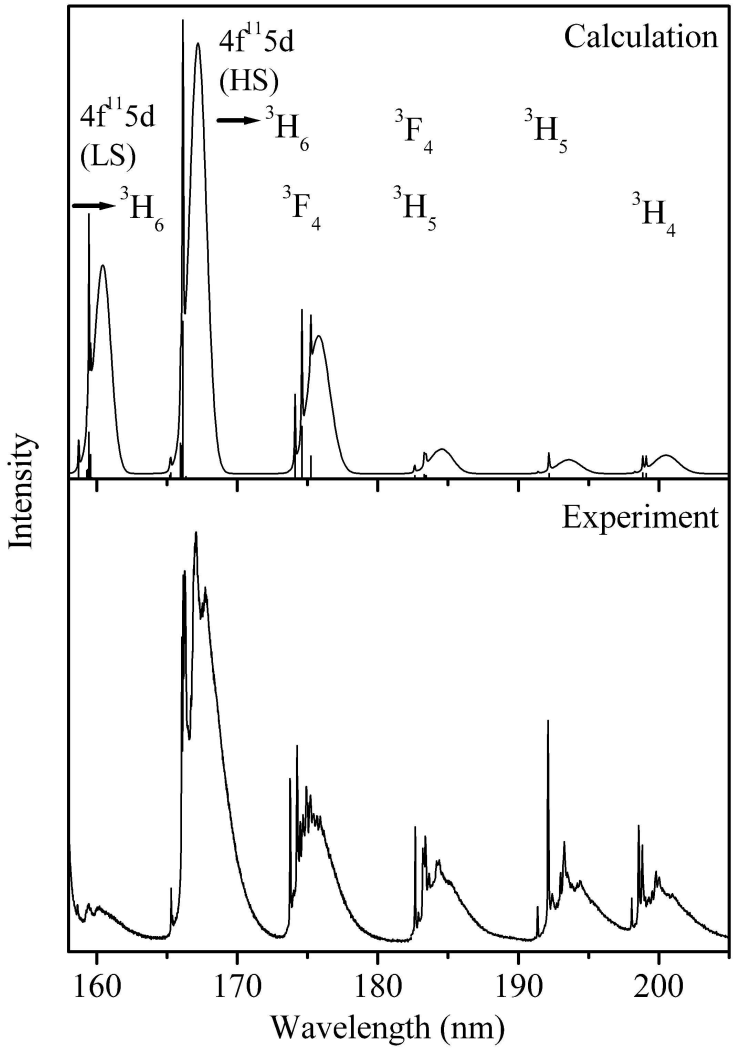

Figure 5.8: Calculated and measured emission spectrum of $LiYF_4$:Tm^{3+} 1% upon excitation at 157 nm at 10 K. The spin–allowed and spin–forbidden emission spectra were calculated separately and their relative intensity was set to match the experimentally observed spectrum. See also figure 5.1.

calculated separately and plotted with a ratio of the high–spin/low–spin emission intensity chosen to match the experimentally observed spectrum. The parameter values used for the calculations are summarized in tables 5.1 and 5.2. The calculated and measured intensities

are in good agreement, except for the spin–allowed emission to the $^3H_6$ levels at 160 nm, which is weaker in the experimental spectrum. This is due to the low sensitivity of the photomultiplier tube at this wavelength. The steep increase on the left hand side of the experimental spectrum is a due to scattered 157 nm radiation of the laser.

Using gated detection it was possible to record an emission spectrum for $LiYF_4$:Tm^{3+} showing only the spin–forbidden emissions. The spin–allowed fd–emission for Tm^{3+} in $LiYF_4$ has a 16 ns life time [19] and by applying gated detection with a delay of 1 μs and a gate of 5 μs, only the longer lived spin–forbidden emission ($\tau = 5.4\mu s$) is detected. The resulting emission spectrum is depicted in figure 5.9 together with the calculated spin–forbidden emission spectrum. The intensity ratios of the zero–phonon lines in the emission spectra show a good agreement with the calculated intensities.

5.4.3 Luminescence lifetime measurements

The lifetime of the spin–forbidden $4f^{n-1}5d \rightarrow 4f^n$ emission was measured for Er^{3+} in $LiYF_4$ and YPO_4 and for Tm^{3+} in $LiYF_4$. In figure 5.10 a typical example of a luminescence decay curve is shown. The luminescence decay is well–described by a single exponential with a lifetime in the order of μs. The experimentally observed lifetimes are included in table 5.3. The presently reported lifetimes are somewhat different from values published previously by us and also other groups [19, 20]. The reason is that in previous work the life times were obtained from luminescence decay curves measured at a synchrotron. The repetition rate (typically MHz) of synchrotron radiation is determined by the round trip time of bunches in the ring and is too high to accurately determine lifetimes that are μs or longer. For MHz repetition rates the decrease in signal between two pulses is very limited and the determination of the lifetime from the fit to a single exponential is rather inaccurate. With the presently used VUV laser with a much lower repetition rate (typically 100 Hz) the luminescence lifetimes can be accurately determined in the μs–ms range. We therefore believe that the values for the lifetimes in table 5.3 are more reliable than previously reported values.

Since the $4f^{n-1}5d \rightarrow 4f^n$ transitions are parity–allowed electric dipole transitions it is relatively simple to calculate the radiative transition probability. Using equation 5.8 and the parameter values from tables 5.1 and 5.2 the radiative decay rates were determined using radial integrals $\langle 5d|r|4f\rangle$ tabulated in table 5.3. The general trend in the decay times is well reproduced by the calculation and also the order of magnitude is correct. However, the experimentally obtained decay times are a factor of three lower than the calculated values. It is at this moment not clear what causes the difference. Most probably it is related to the radial integrals $\langle 5d|r|4f\rangle$. The transition probabilities are very sensitive to small changes in this integral. The radial integrals are calculated for the free–ion using Cowan's program [8]. In the crystal the radial integral will change due to covalency effects and this may explain the difference between calculated and experimentally observed luminescence

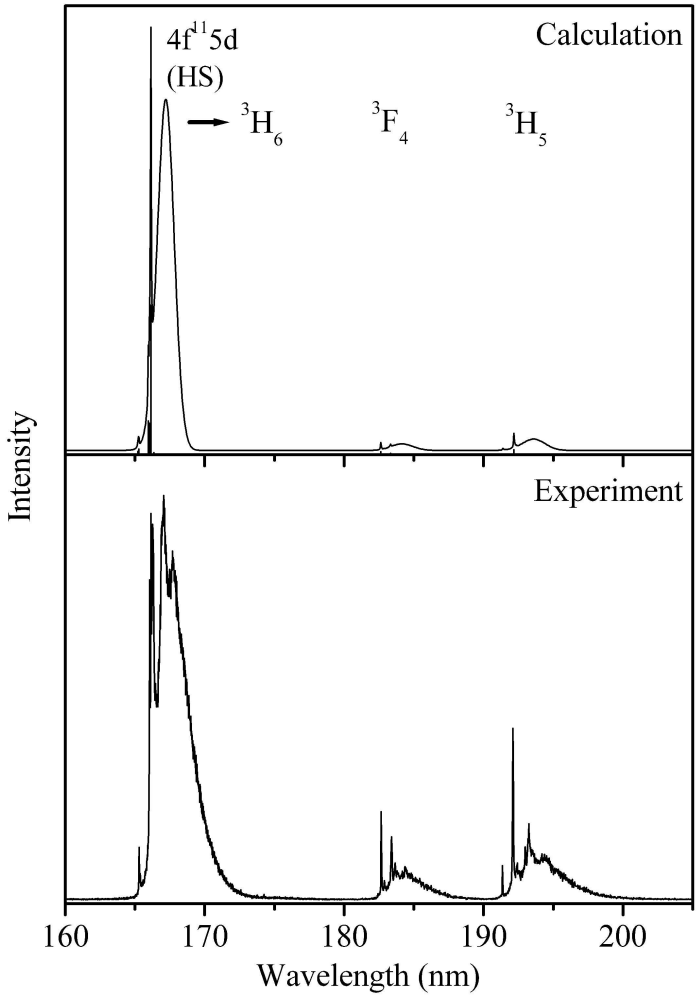

Figure 5.9: Calculated and measured spin–forbidden emission spectrum of $LiYF_4$:Tm^{3+} upon excitation at 157 nm at 10 K using gated detection (delay 1 μs, gate 5 μs). See also figure 5.1.

decay times. For YPO_4:Er^{3+} the shortening of the life time observed may also be partly due to fast non–radiative decay from the lowest high–spin $4f^{10}5d$ level to the $^2F(2)_{7/2}$ level of erbium. The energy difference in the order of 5000 $cm^{-1}$is approximately five times the maximum phonon energy in YPO_4 and multi–phonon relaxation from the lowest high–spin $4f^{10}5d$ level to the $^2F(2)_{7/2}$ level is expected [21].

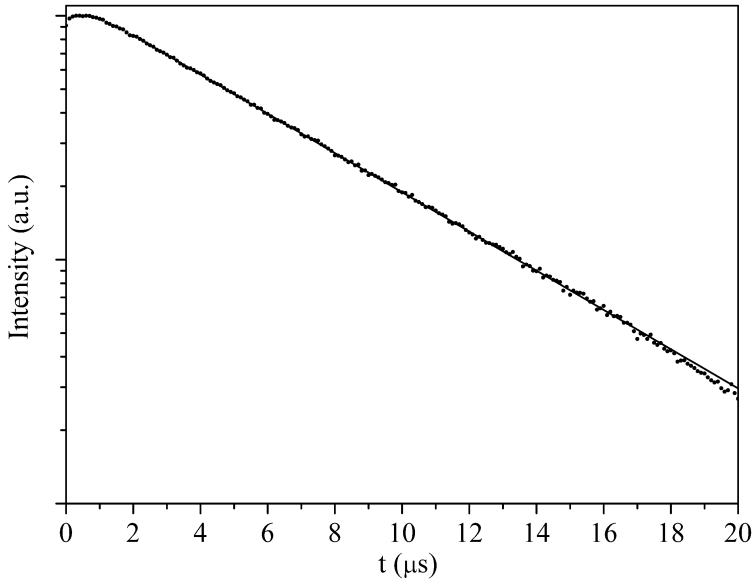

Figure 5.10: Luminescence decay curve of the spin–forbidden $4f^{10}5d \rightarrow 4f^{11}$ emission at 168 nm of $LiYF_4:Tm^{3+}$ upon excitation at 157 nm at 10 K. The dots give the measured time dependence of the luminescence intensity and the drawn line gives the best fit to a single exponential decay with $\tau = 5.4\mu s$. Note that the vertical axis is a logarithmic scale.

Table 5.3: Radial integrals $\langle 5d|r|4f\rangle$ and calculated and experimentally observed lifetimes for the spin–forbidden emissions of Er^{3+} and Tm^{3+} in $LiYF_4$ and YPO_4.

	Wavelength (nm)	τ_{exp} (μs)	τ_{calc} (μs)	$\langle 5d\|r\|4f\rangle$ [8] Å
$LiYF_4:Er^{3+}$	167	2.4	4.2	0.304
$YPO_4:Er^{3+}$	170	1.0	3.4	0.304
$LiYF_4:Tm^{3+}$	168	5.4	13.1	0.291

5.5 Conclusions

High resolution $4f^{n-1}5d \rightarrow 4f^n$ emission spectra of Pr^{3+} Nd^{3+} Er^{3+} and Tm^{3+} in $LiYF_4$ and YPO_4 have been measured and were compared with calculated emission spectra using a recently developed model for $4f^{n-1}5d$ states. The emission spectra show a well–

resolved fine structure with sharp zero–phonon lines and, especially in the YPO_4 host lattice, vibronic lines. In general a good agreement between calculation and experiment was found for the relative intensities and energies of zero–phonon lines corresponding to $4f^{n-1}5d \rightarrow 4f^n$ transitions to the lower energy $4f^n$ states. Luminescence lifetimes for the spin–forbidden $4f^{n-1}5d \rightarrow 4f^n$ emissions were calculated and found to be longer than the experimentally observed lifetimes.

References

[1] L. van Pieterson, M. F. Reid, R. T. Wegh, S. Soverna and A. Meijerink, *Phys. Rev. B* **65** (2002), 045113.

[2] L. van Pieterson, M. F. Reid, G. W. Burdick and A. Meijerink, *Phys. Rev. B* **65** (2002), 045114.

[3] Y. Chen, M. Kirm, E. Negodin, M. True, S. Vielhauer and G. Zimmerer, *Phys. Stat. Sol. B* **240** (2003), R1.

[4] C. Görller-Walrand and K. Binnemans, *Handbook on the Physics and Chemistry of Rare Earths*, Elsevier, Amsterdam (1996) vol 23.

[5] B. Henderson and G. F. Imbush, *Optical Spectroscopy of Inorganic Solids*, Clarendon Press, Oxford (1989).

[6] O. Guillot–Noel, B. Bellamy, B. Viana and D. Gourier, *Phys. Rev. B* **60** (1999), 1668.

[7] G. F. Imbush and R. Copelman, *Laser Spectroscopy of Solids*, edited by W. M. Yen and P. M. Selzer, Springer, New York (1981).

[8] R. D. Cowan, *The Theory of Atomic Structure and Spectra*, University of California, Berkeley, (1981).

[9] B. G. Wybourne, *Spectroscopic Properties of Rare Earths*, Interscience Publishers (1965), New York.

[10] G. W. Burdick and F. S. Richardson, *Chem. Phys.* **228** (1998), 81.

[11] T. Hayhurst, G. Shalimoff, N. Edelstein, L. A. Boatner and M. M. Abraham, *J. Chem. Phys.* **76** (1982), 3960.

[12] A. A. S. da Gama, G. F. de Sá, P. Porcher and P. Caro, *J. Chem. Phys.* **75** (1981), 2583.

[13] M. A. Couto dos Santos, E. Antic-Fidancev, J. Y. Gesland, J. C. Krupa, M. Lemaître-Blaise and P. Porcher, *J. Alloys Comps.* **275-277** (1998), 435.

[14] T. Hayhurst, G. Shalimoff, N. Edelstein, L. A. Boatner and M. M. Abraham, *J. Chem. Phys.* **74** (1981), 5449.

[15] H. P. Jenssen, A. Linz, R. P. Leavitt, C. A. Morrison and D. E. Wortman, *Phys. Rev. B* **11** (1975), 92.

[16] M. F. Reid, L. van Pieterson, R. T. Wegh and A. Meijerink, *Phys. Rev. B* **62** (2000), 14744.

[17] W. T. Carnall, G. L. Goodman, K. Rajnak and R. S. Rana, *J. Chem. Phys.* **90** (1989), 3443.

[18] G. M. Williams, P. C. Becker, J. G. Conway, N. Edelstein, L. A. Boatner and M. M. Abraham, *Phys. Rev. B* **40** (1989), 4132.

[19] L. van Pieterson, R. T. Wegh, A. Meijerink and M. F. Reid, *J. Chem. Phys.* **115** (2001), 9382.

[20] V. N. Makhov, N. M. Khaidukov, N. Y. Kirikova, M. Kirm, J. C. Krupa, T. V. Ouvarova and G. Zimmerer, *J. Lumin.* **87–89** (2000), 1005.

[21] R. T. Wegh, W. van Klinken and A. Meijerink, *Phys. Rev. B* **64** (2001), 045115.

Chapter 6

Thulium as a sensitizer for the Gd^{3+}/Eu^{3+} quantum cutting couple

The increasing knowledge of the energy level structure of the lanthanides has led to new applications for these ions. The Gd^{3+}/Eu^{3+} quantum cutting couple was discovered a few years ago and may be applied in phosphors for fluorescent tubes based on a VUV xenon discharge. The VUV absorption of the phosphor $LiGdF_4:Eu^{3+}$ is poor and therefore a sensitizer is needed. This contribution describes the investigation of using the strong $4f^{12} \rightarrow 4f^{11}5d$ VUV absorption bands of thulium ions as a sensitizer for the Gd^{3+}/Eu^{3+} quantum cutting couple. The incorporation of thulium in the quantum cutting phosphor $LiGdF_4$ does result in sensitization of Gd^{3+} but not in downconversion in the Gd^{3+}/Eu^{3+} couple. A competing downconversion process between gadolinium and thulium occurs resulting in infrared emission of thulium, which is not suitable for lighting applications.

6.1 Introduction

During the twentieth century the knowledge on the spectroscopic properties of lanthanides expanded vastly and was based on both experimentally obtained and calculated energy level diagrams. Wybourne described a method for the calculation of the energy level diagrams of lanthanide ions [1, 2]. Dieke constructed an energy level diagram based on experimentally observed energy levels up to 40 000 cm^{-1} in $LaCl_3$ and is still being referred to nowadays as the Dieke-diagram [3, 4].

In the 1980s Carnall and coworkers [5] performed an extensive study of the energy levels of lanthanides in LaF_3. Carnall combined the experimentally observed levels with calculations and extended the energy level diagram up to 50 000 cm^{-1}.

The vacuum ultraviolet (VUV) region of the electromagnetic spectrum is situated between 50 and 200 nm (200 000 to 50 000 cm^{-1}). Research on the VUV energy levels of lanthanide ions has been very limited until recently. Two decades ago, VUV absorption spectra were reported for Ho^{3+} [6] and Er^{3+} [7]. A few f-f transitions in the VUV were observed, but at that time no further research investigating $4f^n$-$4f^n$ transitions of other lanthanide ions was performed. One reason for this was the absence of good experimental facilities for VUV spectroscopy. VUV spectroscopy requires special setups, with intense tunable sources of VUV radiation like deuterium lamps or synchrotrons and VUV monochromators.

Another reason for the low number of reports on VUV spectroscopy was the absence of applications that require knowledge on VUV levels of these ions. This has changed with the need for new phosphors in for instance plasma display panels and mercury free fluorescent tubes.

The efficiency of the phosphors currently applied in mercury based fluorescent tubes is close to 100%. For environmental reasons however, an alternative for the mercury discharge is being investigated. Xenon discharge seems to be a promising candidate, having emissions at 147 and 172 nm with a ratio depending on the xenon pressure. The phosphors applied in mercury based fluorescent tubes have been optimized for absorption at the main mercury emission line at 254 nm. These phosphors do not all perform well under excitation by a xenon discharge since the VUV absorption or stability are low and consequently new phosphors have to be found. Another issue is the energy-loss involved in the conversion of a photon in the ultraviolet to a visible photon (65% loss for a 172 nm photon compared to 50% for a 254 nm photon). Moreover, the efficiency of the mercury plasma is 75% whereas the highest xenon discharge efficiency reported is 65% [8].

In order to obtain a higher energy efficiency than a mercury based discharge lamp, a xenon based fluorescent tube needs phosphors with a visible quantum efficiency higher than 100%. This is possible with a so-called quantum cutting phosphor which upon VUV excitation emits two (visible) photons for each VUV photon absorbed. Already in 1957 the possibility for quantum cutting was discussed by Dexter [9] and in the 1970s it was

show that Pr^{3+} can emit two visible photons upon VUV excitation [10–12]. More recently Wegh *et al.* reported on the quantum cutting phosphor $LiGdF_4$:Eu^{3+} [13]. Upon VUV excitation this phosphor emits two visible photons via a two-step energy transfer process. After VUV excitation of the gadolinium ions and energy migration over the gadolinium sublattice, part of the excitation energy is transferred via cross relaxation to a neighboring europium ion which gets excited into the $^5D_0$ state. Next, the europium emits a visible photon. A second europium ion gets excited by direct energy transfer of the remaining energy of the excited gadolinium ion. This europium ion also emits a visible photon. The estimated quantum yield that can be achieved for this system is 190%.

For application in a xenon based fluorescent tube, the quantum cutting phosphors must have a good absorption in the VUV. For $LiGdF_4$:Eu^{3+} this is not the case since the gadolinium absorptions at 172 nm are parity and spin-forbidden $4f^n$–$4f^n$ transitions. A so called sensitizer is needed that shows good absorption in the VUV and can transfer the energy efficiently to the gadolinium ions. Wegh [14] reported on the energy transfer from thulium to gadolinium ions. Thulium absorbs efficiently in the VUV, where the $4f^{12} \rightarrow 4f^{11}5d$ absorption bands are situated. The energy transfer for $LiGdF_4$:Tm^{3+} is depicted schematically in figure 6.1. The thulium f–d emission has a good overlap with the high energy levels of gadolinium. Since efficient transfer to the ^6G_J and higher states gadolinium has been found, thulium may be used as a sensitizer for the Gd^{3+}/Eu^{3+} quantum cutting couple. In this paper we investigate whether Tm^{3+} can be used as an efficient sensitizer for the Gd^{3+}/Eu^{3+} quantum cutting system in $LiGdF_4$:Eu^{3+}.

6.2 Experimental

Powder samples of $LiGdF_4$:Tm^{3+} 1% and $LiGdF_4$:Tm^{3+} 1%,Eu^{3+} 0.3% were prepared by firing stoichiometric amounts of GdF_3, LiF (10% excess), TmF_3 and EuF_3 in a furnace. The samples were heated at 200 °C for 3 hours to remove water adsorbed in the starting materials. The fluoride mixture was then heated to 675°C for 8 hours. The furnace was flushed with nitrogen and NH_4F was added to the crucibles to create a fluoride atmosphere. X-ray diffraction patterns were recorded to confirm the structure and phase purity of the sample using a Philips PW1729 X-ray diffractometer.

Low resolution excitation and emission measurements were performed on a SPEX 1680 spectrofluorometer equipped with 0.22 m double monochromators. The spectral resolution of these spectrofluorometers is about 0.5 nm. For VUV/UV excitation a D2-lamp (Hamamatsu L1835, 150W) fitted with a MgF_2 window was used. The excitation monochromator contains VUV-gratings blazed at 150 nm (1200 lines/mm) and Al mirrors coated with MgF_2. Excitation spectra were recorded in the range 140–350 nm and were corrected for lamp intensity using sodium salicylate excitation spectra as reference. To avoid absorption of VUV radiation by oxygen the lamp housing, excitation monochroma-

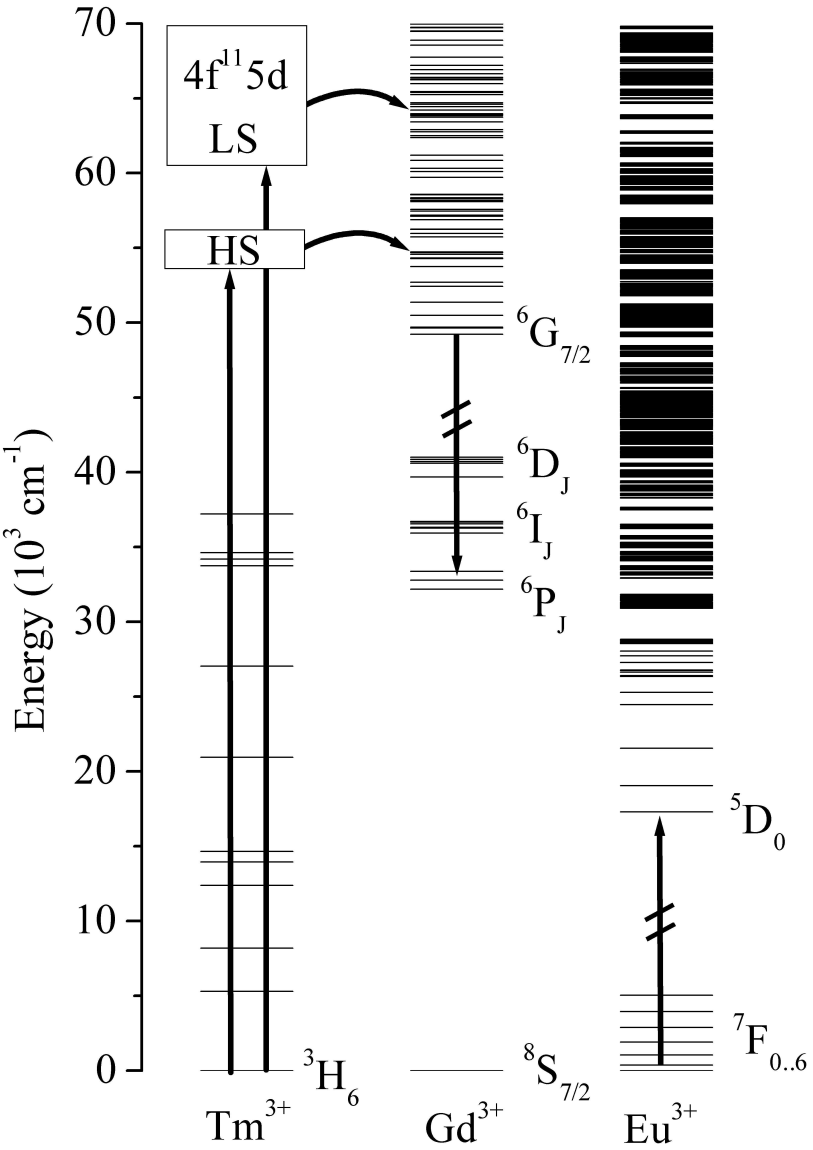

Figure 6.1: Schematic energy level diagram for $LiGdF_4$:Tm^{3+},Eu^{3+} showing energy transfer upon $4f^{11}5d$ excitation of Tm^{3+}.

tor and sample chamber were flushed with nitrogen for at least 2 hours prior to measurements. The emission monochromator is equipped with gratings blazed at 500 nm (1200

lines/mm). The signal was detected with a cooled Hamamatsu R928 photomultiplier tube, with which emission in the range of 250–800 nm could be measured. Emission spectra recorded with the R928 photomultiplier tube were corrected for the monochromator and detector response using correction spectra provided by the manufacturer.

Higher resolution excitation spectra and low resolution VUV/UV/Vis emission spectra and luminescence decay times were measured at the HIGITI setup of the HASYLAB Synchrotron-Strahlungslabor at DESY in Hamburg. For a detailed description of this setup, see Ref. [15]. The excitation monochromator consists of a Wadsworth 1m monochromator with a holographic MgF_2-coated Al grating blazed at 150 nm (1200 lines/mm), providing an ultimate resolution of 0.3 Å. Excitation was possible in the range 80 – 400 nm. Emission spectra in the range of 250–1080 nm were recorded using a Tektronix CCD array attached to a monochromator with a 150 lines/mm and a 1200 lines/mm grating. The temperature of the sample could be varied between 10 K and room temperature. The pressure in the sample chamber was maintained below 10^{-8} mbar.

6.3 Results and Discussion

Figure 6.2 shows the excitation spectrum of $LiGdF_4$:Tm^{3+} (1%) monitoring gadolinium $^6P_{7/2}$ emission (311 nm) measured at the synchrotron setup. The low-spin and high-spin $4f^{11}5d$ bands of thulium are observed between 120–160 and 160–165 nm, respectively. The observation that the Tm^{3+} excitation bands are present in the excitation spectrum of Gd^{3+} emission indicates that energy transfer from thulium to gadolinium occurs. In the region 165–205 nm excitation lines corresponding to the $4f^7$ levels of gadolinium are observed. This region of the spectrum is similar to the excitation spectrum for Gd^{3+} in $LiYF_4$ [15].

In order to serve as an efficient sensitizer for the Gd^{3+}/Eu^{3+} couple, the absorption of VUV radiation should be followed by energy transfer to one of the high energy (VUV) energy levels of Gd^{3+}. From the high energy levels fast relaxation to the $^6G_{7/2}$ level occurs and this level serves as the starting level for the quantum cutting process. The strongest f–d emission bands of Tm^{3+} in $LiYF_4$ are situated in the VUV region and have a good spectral overlap with the VUV energy levels of Gd^{3+} [16]. As a result, energy transfer to the high energy levels of Gd^{3+} is expected resulting in population of the $^6G_{7/2}$ level.

The excitation spectrum in figure 6.2 shows that the Tm f–d absorption bands can efficiently absorb the VUV emission from a Xe discharge in the spectral region below 160 nm. To test if absorption of the VUV radiation is followed by quantum cutting through the downconversion process in the Gd/Eu couple, emission spectra have been recorded. By comparison of the emission spectra recorded upon VUV excitation and lower energy excitation, for example in the ^6I_J levels (272 nm), the occurrence of quantum cutting can

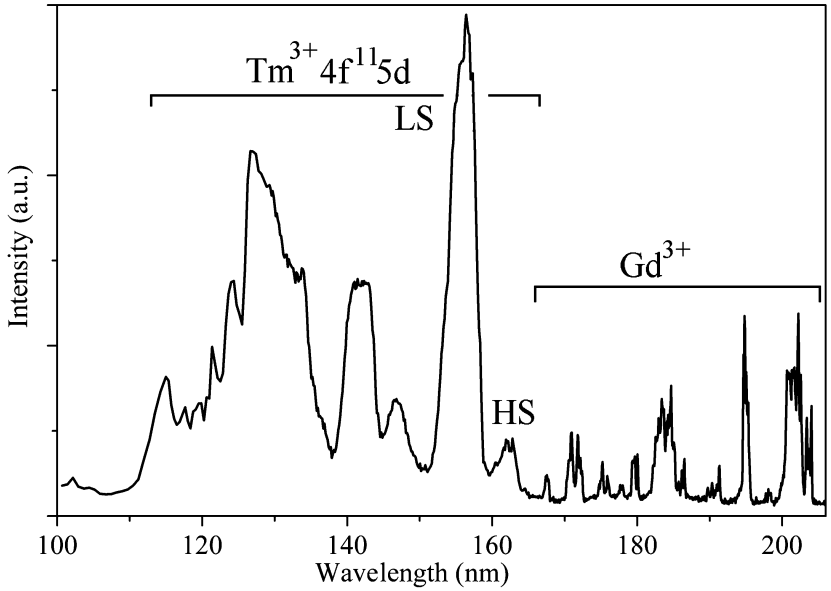

Figure 6.2: Excitation spectrum of $LiGdF_4$:Tm^{3+} (1%) monitoring gadolinium $^6P_{7/2}$ emission (311 nm) at 10K.

be observed by an increase in the $^5D_0$ emission of europium relative to the emissions from the $^5D_1$ and higher levels. The first step of the quantum cutting process (cross-relaxation from the $^6G_{7/2}$ level of Gd^{3+}) only populates the $^5D_0$ level of europium, while the second energy transfer populates all ^5D_J levels.

Excitation in the lower energy levels of Gd^{3+} or in the UV levels of Eu^{3+} results in a fast relaxation to the various ^5D_J levels and emission from the different ^5D_J levels in a ratio that is determined by the relaxation rates to the lower ^5D levels. As a result of the direct feeding of the $^5D_0$ level from the $^6G_{7/2}$ level a significant increase of the relative intensity of the $^5D_0$ emission is expected upon VUV excitation and serves as a signature for the occurrence of quantum cutting [17]. In figure 6.3 the emission spectra are shown for $LiGdF_4$:Eu^{3+},Tm^{3+} upon excitation in the f–d band of Tm^{3+} (at 156 nm), excitation in the $^6G_{7/2}$ level of Gd^{3+} (202 nm) and excitation in the ^6I_J level of Gd^{3+} (272 nm). For excitation at 202 nm (in the $^6G_{7/2}$ level of Gd^{3+}) and 156 nm (in the fd level of Tm^{3+}) quantum cutting is expected to occur. Comparison of the spectra in figure 6.3 shows however that the intensity of the $^5D_0$ emission does not increase relative to the emission from the higher energy ^5D_J levels. This indicates that the desired quantum cutting process is not sensitized by Tm^{3+} and that the incorporation of Tm^{3+} even eliminates the Gd^{3+}/Eu^{3+} downconversion process upon direct excitation in the $^6G_{7/2}$ level of Gd^{3+}.

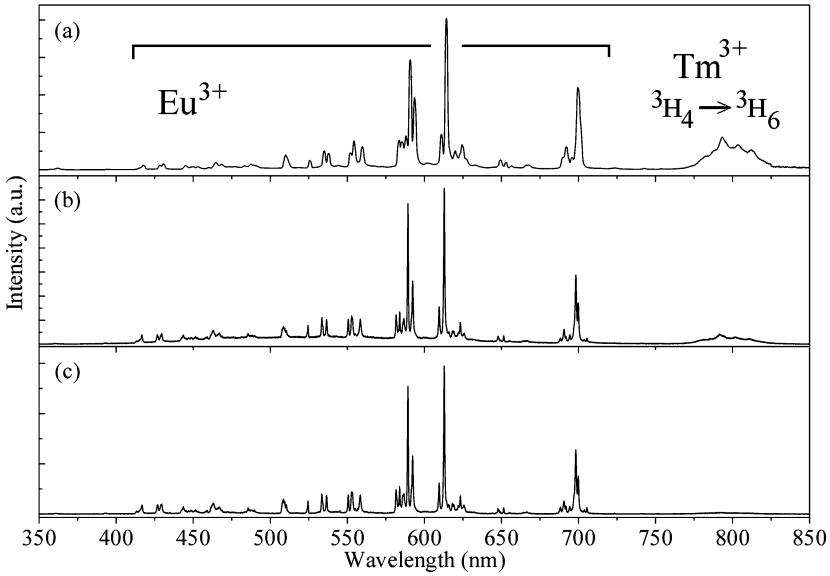

Figure 6.3: Emission spectra of $LiGdF_4$:Tm^{3+} 1%,Eu^{3+} 0.3% upon excitation (a) in the f–d band of Tm^{3+} at 156 nm, (b) $^6G_{7/2}$ excitation at 202 nm, and (c) upon ^6I_J excitation at 272 nm. All spectra are recorded at room temperature.

To understand what is causing the apparent absence of quantum cutting, a careful inspection of the emission spectra is required. Even though the ratio of the $^5D_0$ to ^5D_J emission is the same in figures 6.3 (a) through (c), there is a significant difference in the near-infrared part of the spectrum. Only under VUV excitation (156 nm or 202 nm) an emission is observed in the infrared spectral region around 800 nm. This emission is assigned to $^3H_4 \rightarrow {}^3H_6$ emission from Tm^{3+}. The fact that the $^3H_4$ emission is much stronger upon VUV excitation indicates that there is direct feeding of the $^3H_4$ level of Tm^{3+} from the $^6G_{7/2}$ level of Gd^{3+}. This increase can be explained by a cross relaxation process between gadolinium and thulium (see figure 6.4).

The energies of the emissions from the $^6G_{7/2}$ level to the ^6D_J and ^6I_J levels match the excitation energies from the thulium $^3H_6$ ground state to the $^3H_5$ and $^3H_4$ levels. In the spectrum of figure 6.3 the increase in emission from the $^3H_4$ level at 800 nm indicates energy transfer from gadolinium to thulium. Since no energy transfer by cross relaxation to the europium $^5D_0$ level is observed, energy transfer to thulium is probably more efficient than energy transfer to europium. To understand why the cross-relaxation process from the $^6G_{7/2}$ level of Gd^{3+} shown in figure 6.4 is more efficient than the (desired) cross-relaxation process $Gd^{3+}(^6G_{7/2} \rightarrow {}^6P_{7/2})$ $Eu^{3+}(^7F_1 \rightarrow {}^5D_0)$, we calculated the re-

duced matrix elements that determine the oscillator strengths of the transitions involved. The theory for the calculation of oscillator strengths for intraconfigurational $4f^n$ transitions was developed in the early 1960's by Wybourne, Judd and Ofelt and allows one to predict the oscillator strengths with a good accuracy [1, 2, 18, 19]. In table 6.1 the squares

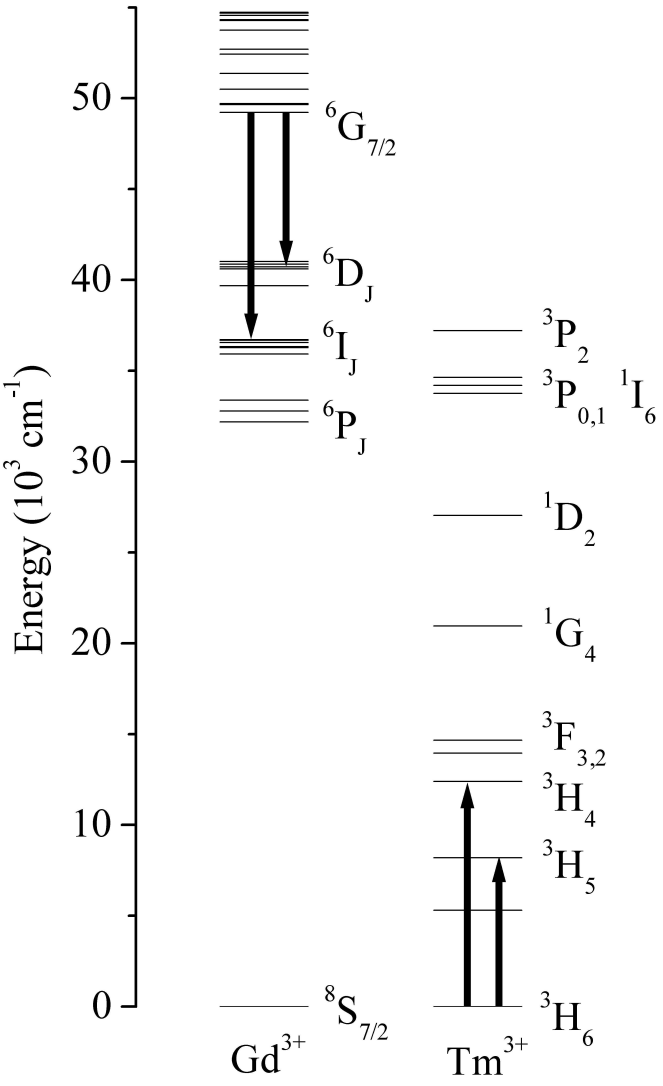

Figure 6.4: Energy level diagrams of gadolinium and thulium showing the possibility for cross relaxation.

of reduced matrix elements for the various emissions originating from the $^6G_{7/2}$ level are collected together with the squares of the reduced matrix elements for absorptions of Tm^{3+} ions.

In this table the transitions originating from the gadolinium $^6G_{7/2}$ level that have approximately the same energy as thulium absorptions are displayed in bold. The energies show a mismatch of some tens of cm^{-1}, but the energies given are for the free ion levels. The energy mismatch for the free ion levels is so small that the crystal field splitting and

Table 6.1: Squares of the reduced matrix elements for gadolinium $^6G_{7/2}$ emission and thulium $^3H_6$ absorptions. Transitions relevant for (resonant) cross-relaxation are typeset in bold.

Gadolinium emissions				
Transition	Energy (cm^{-1})	$\left(U^{(2)}\right)^2$	$\left(U^{(4)}\right)^2$	$\left(U^{(6)}\right)^2$
$^6G_{7/2} \rightarrow {}^8S_{7/2}$	49226	6.7801E-05	4.1666E-03	1.9040E-05
$^6G_{7/2} \rightarrow {}^6P_{7/2}$	17033	9.9715E-03	1.8458E-01	8.5570E-04
$^6G_{7/2} \rightarrow {}^6P_{5/2}$	16433	3.3504E-03	1.3204E-01	3.1071E-05
$^6G_{7/2} \rightarrow {}^6P_{3/2}$	15836	6.6171E-04	1.2743E-01	0
$^6G_{7/2} \rightarrow {}^6I_{7/2}$	13295	3.5304E-02	9.0484E-02	1.5802E-01
$^6G_{7/2} \rightarrow {}^6I_{9/2}$	12948	5.4468E-02	4.8707E-02	2.2478E-02
$^6G_{7/2} \rightarrow {}^6I_{17/2}$	12893	0	0	1.0171E-01
$^6G_{7/2} \rightarrow {}^6I_{11/2}$	12669	3.1283E-02	3.3279E-04	1.4364E-02
$^6G_{7/2} \rightarrow {}^6I_{15/2}$	**12550**	**0**	**8.2359E-02**	**7.1557E-02**
$^6G_{7/2} \rightarrow {}^6I_{13/2}$	**12515**	**0**	**5.2193E-02**	**6.3881E-02**
$^6G_{7/2} \rightarrow {}^6D_{9/2}$	9541	4.4318E-02	8.4008E-02	2.1074E-02
$^6G_{7/2} \rightarrow {}^6D_{1/2}$	8620	0	7.4730E-04	0
$^6G_{7/2} \rightarrow {}^6D_{7/2}$	8505	1.4829E-01	5.7148E-06	1.5910E-02
$^6G_{7/2} \rightarrow {}^6D_{3/2}$	8360	9.9989E-02	6.0116E-03	0
$^6G_{7/2} \rightarrow {}^6D_{5/2}$	**8214**	**7.5861E-03**	**3.6992E-02**	**2.3796E-02**
Thulium absorptions				
Transition	Energy (cm^{-1})	$\left(U^{(2)}\right)^2$	$\left(U^{(4)}\right)^2$	$\left(U^{(6)}\right)^2$
$^3H_6 \rightarrow {}^3H_6$	0	1.2527E+00	6.9030E-01	7.7510E-01
$^3H_6 \rightarrow {}^3F_4$	5308	5.5282E-01	7.3859E-01	2.5407E-01
$^3H_6 \rightarrow {}^3H_5$	**8192**	**1.0738E-01**	**2.3140E-01**	**6.3830E-01**
$^3H_6 \rightarrow {}^3H_4$	**12390**	**2.2556E-01**	**1.0006E-01**	**5.8149E-01**
$^3H_6 \rightarrow {}^3F_3$	13961	0	3.1637E-01	8.4105E-01
$^3H_6 \rightarrow {}^3F_2$	14659	0	5.5957E-06	2.5544E-01
$^3H_6 \rightarrow {}^1G_4$	20957	4.4598E-02	7.1409E-02	9.8739E-03
$^3H_6 \rightarrow {}^1D_2$	27041	0	3.6236E-01	1.0085E-01
$^3H_6 \rightarrow {}^3P_0$	33755	0	0	7.5778E-02
$^3H_6 \rightarrow {}^1I_6$	34201	1.0690E-02	3.9162E-02	1.3522E-02
$^3H_6 \rightarrow {}^3P_1$	34636	0	0	1.2390E-01
$^3H_6 \rightarrow {}^3P_2$	37213	0	2.1778E-01	1.6996E-02
$^3H_6 \rightarrow {}^1S_0$	74344	0	0	3.0686E-05

phonon assistance will allow for resonant energy transfer in the $LiGdF_4$ crystallites. The transition probabilities P depend on the squares of the reduced matrix elements $\left(U^{(\lambda)}\right)^2$ as follows:

$$P \propto \nu^x \sum_{\lambda=2,4,6} \Omega_\lambda \left(U^{(\lambda)}\right)^2 \tag{6.1}$$

with ν being the frequency of the photon being emitted or absorbed for this transition. For absorption x is 1, for emission x is 3. The Judd-Ofelt parameters Ω_λ are lattice dependent and can be obtained from absorption and emission spectra. For Gd^{3+} in $LiYF_4$ the values $\Omega_2 = 0.32{\cdot}10^{-20}$ cm^2, $\Omega_4 = 0$ and $\Omega_6 = 1.8{\cdot}10^{-20}$ cm^2 were reported by Ellens [20]. The high value of Ω_6 implies that for Gd^{3+} in $LiYF_4$ the transition intensities are dominated by the $U^{(6)}$ reduced matrix elements. We expect the Judd-Ofelt parameters to be similar for $LiGdF_4$ and as a result the numbers for the $\left(U^{(6)}\right)^2$ matrix elements in table 6.1 will give the dominant contribution to the dipole strengths of the transitions involved in the downconversion processes. If the energy transfer occurs through dipole-dipole interaction, the efficiency of the downconversion process will be proportional to the product of the dipole strengths of transitions involved on the donor and acceptor ions. For the Gd^{3+}/Tm^{3+} couple the transitions involved are the $^6G_{7/2} \rightarrow {}^6I_J$ and $^6G_{7/2} \rightarrow {}^6D_J$ transitions on Gd^{3+} and the $^3H_6 \rightarrow {}^3H_4$ and $^3H_6 \rightarrow {}^3H_5$ transitions on Tm^{3+}, respectively. For the Gd^{3+}/Eu^{3+} couple the transitions involved are $^6G_{7/2} \rightarrow {}^6P_{7/2}$ on Gd^{3+} and $^7F_1 \rightarrow {}^5D_0$ on Eu^{3+}. Inspection of table 6.1 shows that the $\left(U^{(6)}\right)^2$ matrix elements for the $^6G_{7/2} \rightarrow {}^6I_J$ transitions are almost two orders of magnitude higher than for the $^6G_{7/2} \rightarrow {}^6P_{7/2}$ transitions. This explains the higher efficiency of the downconversion between Gd^{3+} and Tm^{3+} in comparison with Gd^{3+} and Eu^{3+}. The dipole strengths of the transitions on Tm^{3+} ($^3H_6 \rightarrow {}^3H_4$) and Eu^{3+} ($^7F_1 \rightarrow {}^5D_0$, the magnetic dipole strength calculated for this transition is $4.13{\cdot}10^{-23}$ cm^2) also favor cross-relaxation between Gd^{3+} and Tm^{3+} over cross-relaxation between Gd^{3+} and Eu^{3+}. This analysis shows that even though Tm^{3+} can efficiently sensitize the $^6G_{7/2}$ level of Gd^{3+} upon excitation in the $4f^{11}5d$ absorption band, the desired Gd^{3+}/Eu^{3+} downconversion process does not occur due to competition by Gd^{3+}/Tm^{3+} downconversion. As a solution for this problem one may suggest to increase the Eu^{3+} concentration. This will favor Gd^{3+}/Eu^{3+} downconversion due to a higher number of Eu^{3+} ions compared to Tm^{3+}. There is little hope, however, that this will work. Eu^{3+} has a strong charge transfer (F^- to Eu^{3+}) absorption band around 160 nm [21]. Excitation in this band is followed by a fast relaxation to the various $4f^6$ excited states and results in the emission of only one visible photon from a ^5D_J level. If the Eu^{3+} concentration exceeds the Tm^{3+} concentration this competing VUV absorption will prevent sensitization of the $^6G_{7/2}$ level of Gd^{3+}. The fact that in the $LiGdF_4$:Tm^{3+} 1%, Eu^{3+} 0.3% sample there is no sign of quantum cutting through the Gd^{3+}/Eu^{3+} couple indicates that the downconversion rate for the Gd^{3+}/Eu^{3+} couple is very much smaller than for the Gd^{3+}/Tm^{3+} couple. This is supported by the analy-

sis of the dipole strengths of the transitions involved and indicates that only for a very high Eu^{3+} concentration (in comparison to the Tm^{3+} concentration) the quantum cutting through the Gd^{3+}/Eu^{3+} couple may be favored. For the high Eu^{3+} concentrations the VUV absorption due to the Eu-F charge transfer transition will be much stronger than the f–d absorption by Tm^{3+} ions and sensitization of the $^6G_{7/2}$ level of Gd^{3+} will not occur.

6.4 Conclusions

Thulium was investigated as a sensitizer for the gadolinium/europium quantum cutting couple. Excitation into the strong f–d absorption bands of Tm^{3+} does result in sensitization of the Gd^{3+} $^6G_{7/2}$ level but is not followed by quantum cutting through downconversion by the Gd^{3+}/Eu^{3+} couple. Instead, a cross relaxation process was found to occur between gadolinium and thulium ions. The higher efficiency for this (competing) downconversion process could be explained by combining the energy level schemes of the ions with calculated reduced matrix elements for the transitions involved. The results show that thulium is not a suitable candidate for sensitizing the gadolinium/europium quantum cutting couple. The infrared emission of thulium generated by the quantum cutting process cannot be used in lighting applications. Our current research investigates other ions for their application as a sensitizer for the $LiGdF_4$:Eu^{3+} phosphor.

References

[1] B. G. Wybourne, *J. Chem. Phys.* **36** (1962), 2295.

[2] B. G. Wybourne, *Spectroscopic Properties of the Rare Earths*, J. Wiley and Sons Inc., New York (1965).

[3] G. H. Dieke, and H. M. Crosswhite, *Appl. Opt.* **2** (1963), 675.

[4] G. H. Dieke, *Spectra and energy levels of rare earth ions in crystals*, Interscience Publishers, New York (1968).

[5] W. T. Carnall, G. L. Goodman, K. Rajnak and R. S. Rana, *A Systematic Analysis of the Spectra of the Lanthanides Doped into Single Crystal LaF_3* Argonne National Laboratory, Argonne Illinois (1988).

[6] A. A. Vlasenko, L. I. Devyatkova, O. N. Ivanova, V. V. Mikhailin, S. P. Chernov, T. V. Uvarova and B. P. Sobolev, *Sov. Phys. Dokl.* **30** (1985), 395.

[7] K. M. Devyatkova, O. N. Ivanova, K. B. Seiranyan, S. A. Tamazyan and S. P. Chernov, *Sov. Phys. Dokl.* **35** (1990), 40.

[8] F. Vollkommer and L. Hitzschke, Patent-Treuhand-Gesellschaft für elektrische Glühlampen mbH, WO-A 94/23442 (1994).

[9] D. L. Dexter, *Phys. Rev.* **108** (1957), 630-633.

[10] J. L. Sommerdijk, A. Bril and A. W. de Jager, *J. Lumin.* **8** (1974), 341.

[11] J. L. Sommerdijk, A. Bril and A. W. de Jager, *J. Lumin.* **9** (1974), 288.

[12] W. W. Piper, J. A. DeLuca and F. S. Ham, *J. Lumin.* **8** (1974), 344.

[13] R. T. Wegh, H. Donker, K. D. Oskam and A. Meijerink, *Science* **283** (1999), 663-666.

[14] R. T. Wegh, Ph.D thesis, (1999) Utrecht University.

[15] R. T. Wegh, H. Donker, A. Meijerink, R. J. Lamminmäki and J. Hölsä, *Phys. Rev. B* **56** (1997), 13841.

[16] R. T. Wegh, and A. Meijerink, *Phys. Rev. B* **60** (1999), 10820.

[17] R. T. Wegh, H. Donker, K. D. Oskam and A. Meijerink, *J. Lumin.* **82** (1999), 93.

[18] B. R. Judd, *Phys. Rev.* **127** (1962), 750.

[19] G. S. Ofelt, *J. Chem. Phys.* **37** (1962), 511.

[20] A. Ellens, H. Andres, M. L. H. Ter Heerdt, R. T. Wegh, A. Meijerink and G. Blasse, *Phys. Rev. B* **55** (1997), 180.

[21] G. Blasse, *J. Phys. Chem. Solids* **50** (1989), 99.

Chapter 7

Visible photon cascade emission from the high energy levels of Er^{3+}

In the past decade quantum cutting phosphors with a visible quantum yield over 100% were investigated. This chapter descibes a method to calculate the maximum visible quantum yield for photon cascade emission of Er^{3+} using Judd–Ofelt theory.

7.1 Introduction

Luminescent tubes based on phosphors doped with lanthanide ions are very popular for household and other general lighting applications. The phosphors currently applied rely on the UV excitation originating from a mercury discharge. The main emission line of mercury is situated at 254 nm. Mercury is toxic and can be replaced by xenon. The xenon discharge has emissions in the vacuum ultraviolet (VUV) at 147 and 172 nm, depending on the pressure, and has the advantage that it requires no start–up time.

The phosphors currently used in luminescent tubes do not absorb the 147 and 172 nm radiation efficiently and/or suffer from degradation upon VUV excitation. Moreover, in the conversion of one VUV photon of the xenon discharge into a visible photon more energy is lost than in the conversion of a UV photon of the mercury discharge into a visible photon. As the xenon discharge efficiency (65%) is lower than the efficiency of the mercury plasma (75%), phosphors with a visible quantum efficiency considerably higher than 100% are required in order to make the xenon discharge lamp competitive (i.e. have a higher energy efficiency) with the mercury based luminescent tube.

A visible quantum efficiency of more than 100% can be achieved by the subsequent emission of two visible photons upon excitation at high energy and the theoretical possibility was reported in 1957 by Dexter [1]. In this publication the possibility of cooperative sensitization of two acceptors by a single donor was discussed for the situation where the excited state of the donor is at twice the energy of the acceptors. Later it was experimentally shown that quantum efficiencies exceeding unity can also be achieved by a photon cascade on a single lanthanide ion. In the 1970s photon cascade emission was observed for Pr^{3+} in YF_3 by Sommerdijk and co–workers [2, 3] and also reported by Piper and co–workers [4].

The luminescent properties of YF_3:Pr^{3+} have been studied extensively as the energy level scheme is suitable for photon cascade emission, where excitation in the $^1S_0$ level results in the consecutive emission of two visible photons. First, emission from the $^1S_0$ level to the $^1I_6$ level yields a photon in the violet region of the electromagnetic spectrum (407 nm). Next, emission from the $^3P_0$ level to the ^3H_J and ^3F_J levels yields photons in the green to red region of the spectrum. A visible quantum efficiency of 140% is reported for YF_3:Pr^{3+} [4], but it is not a phosphor suitable for lighting applications as the violet emission results in a low color rendering index [5].

The possibility for photon cascade emission from high energy levels of other lanthanide ions has been considered but was found to yield quantum efficiencies in the visible below 100% [6]. The recent investigations on the VUV energy levels of lanthanide ions has resulted in many new levels from which photon cascade emission is expected, possibly with quantum efficiencies in the visible above 100%. Recently, the VUV energy levels of Er^{3+} were reported [7]. The erbium ion also has a energy level scheme suitable for photon cascade emission in the visible. $LiYF_4$ and LaF_3 doped with Er^{3+} show emis-

sion from several high $4f^{11}$ levels upon excitation in the $4f^{10}5d$ bands. Photon cascade emission was observed, but the most intense emissions were situated in the UV region of the spectrum. It was concluded that a visible quantum efficiency higher than 100% cannot be achieved with a phosphor based on Er^{3+} alone, but this conclusion was not supported by a quantitative analysis. A proper analysis of the maximum visible quantum efficiency requires the calculation of the branching ratios for the emission from the starting level.

Judd–Ofelt theory can be used to predict transition probabilities (and thus branching ratios) for emissions of lanthanide ions using reduced matrix elements for these transitions. To estimate maximum visible quantum efficiencies for photon cascade emission upon excitation in the high-energy (V)UV levels of Er^{3+} the reduced matrix elements for transitions originating from the VUV levels are needed. Carnall *et al.* [11] reported the reduced matrix elements for transitions on erbium up to the $^2P_{1/2}$ level at 33 000 cm^{-1}. For the transitions involving the higher energy levels the reduced matrix elements have not been reported in the literature. Here, we report the reduced matrix elements for the transitions originating from VUV and UV energy levels of Er^{3+}. In addition to that, we list the reduced matrix elements for absorption from the ground state to all $4f^{11}$ excited states of erbium up to 65 000 cm^{-1}. Using Judd–Ofelt theory we predict the maximum visible quantum efficiency for photon cascade emission starting from the (V)UV levels of Er^{3+}.

7.2 Theory

In the 1960s Judd [8] and Ofelt [9] independently developed a theory for the calculation of transition probabilities between J-multiplets of lanthanide ions. This theory is known as the Judd–Ofelt theory and has played an important role (and still does) in the understanding and interpretation of lanthanide spectra. The derivations in this theory are not easy to understand as they involve complex mathematics. The resulting formulas describing the transition probabilities, however, are surprisingly simple, which makes the Judd–Ofelt theory easy to use. For a review of Judd–Ofelt theory, see ref. [10].

The Judd–Ofelt theory explains the intensity of the "forbidden" $4f^n$–$4f^n$ transitions by taking into account the admixture of configurations of opposite parity (for example $4f^{n-1}5d$ configurations) into the $4f^n$ configuration. One of the approximations used is that the admixing configuration is totally degenerate (the closure approximation) and its energy is set equal to the mean energy of this configuration. The position of the opposite–parity configuration is considered to be far above the $4f^n$ configuration. For lanthanide ions showing emission from a $4f^n$ level for which the lowest $4f^{n-1}5d$ absorption is close to the $4f^n$ level like, for example, the $^1S_0$ level of praseodymium this approximation is not valid and can cause a discrepancy between theory and experiment.

A second approximation used in the Judd–Ofelt theory is that transition probabilities

are calculated for transitions between J–multiplets. In a crystal the J–levels are split by the crystal field and transitions between individual crystal field levels will be different (depending on M_J). Only for situations in which the various crystal field components of the initial state are equally populated (which is true if the crystal field splitting is much smaller than kT) the transition probability is correctly determined with the Judd–Ofelt theory. If this is not the case, the transition probabilities between individual crystal field components have to be evaluated and there will be an influence of temperature due to a variation of the thermal population of the various crystal field components with temperature.

For a general description of transition probabilities, independent of crystal structure, the Judd–Ofelt theory gives a good indication of branching ratios for emission from an initial level to all lower energy levels. In the calculation of transition probabilities it is essential to calculate the reduced matrix elements $\mathrm{U}^{(\lambda)}$ between all possible initial and final $4f^n$ states.

Carnall *et al.* [11] tabulated the (squares of the) reduced matrix elements $U^{(\lambda)}$ for transitions up to about 40 000 cm^{-1} for all lanthanide ions.

The electric dipole strength S_{ed} for a transition from the initial level $f^n[\gamma, S, L]J$ to a final level $f^n[\gamma', S', L']J'$ is defined as

$$S_{\mathrm{ed}} \;=\; \sum_{\lambda=2,4,6} \Omega_\lambda \left| < f^n[\gamma, S, L]J || U^{(\lambda)} || f^n[\gamma', S', L']J' > \right|^2 , \qquad (7.1)$$

where the term Ω_λ is called a Judd–Ofelt parameter and the squared term between brackets is referred to as the reduced matrix element $U^{(\lambda)}$. The transition probability A for a transition can be calculated from the dipole strength S_{ed} by

$$A \;=\; \frac{64\,\pi^4\,e^2\,n(n^2+2)^2\,\nu^3}{27\,h\,(2J+1)}\;S_{\mathrm{ed}}, \qquad (7.2)$$

where n is the refractive index, ν is the frequency of the photon emitted and $(2J+1)$ is the degeneracy of the initial level.

The Judd–Ofelt parameters Ω_λ are lattice dependent and can be obtained from absorption and emission spectra. Ω_λ values have been reported for the lanthanide ions in many host lattices. This allows the prediction of intensities for transitions that have not yet been observed and the Judd–Ofelt intensity parameters can be used to compare intensity ratios for emissions of a lanthanide ion in different host-lattices. See, for instance, ref [12]. Judd–Ofelt theory is used to determine transition probabilities and oscillator strengths for forced electric dipole transitions. The strength for magnetic dipole transitions can be calculated exactly, but these transitions are generally much weaker. If the reduced matrix elements are known for all intraconfigurational transitions of a lanthanide

ion, then transition probabilities and subsequently branching ratios for emissions can be calculated, using the Ω_λ values as parameters.

Using Judd–Ofelt theory a visible quantum efficiency of 157% was calculated for YF_3 by Pappalardo [6]. We present a similar calculation method to predict the maximum visible quantum efficiency for photon-cascade emission of a lanthanide ion upon excitation at different energies, but our method requires less calculation steps as it omits the calculation of radiative lifetimes and non–radiative decay rates.

7.3 Method

As discussed in the previous section the transition probabilities for the emission from an initial $4f^n$ state to final states depends on the squares of the reduced matrix elements $\left(U^{(\lambda)}\right)^2$ as follows:

$$A' \propto \nu^3 \sum_{\lambda=2,4,6} \Omega_\lambda \left(U^{(\lambda)}\right)^2, \tag{7.3}$$

with ν being the frequency of the photon being emitted for this transition. In equation 7.3 no correction for the wavelength dependence of the refractive index n is applied.

Usually emission is observed from an energy level when the energy gap to the next lower level is more than five times the maximum phonon energy of the host-lattice. If the energy difference with the lower level is less, then non-radiative relaxation becomes more probable. With the Judd–Ofelt calculations the radiative transition probability between different J-multiplets can be calculated. The crystal field splitting has to be considered in order to find the energy gaps between energy levels for a lanthanide ion incorporated in a host-lattice. For Er^{3+} we used the emitting levels that have been observed in previous investigations [7]. In LaF_3:Er^{3+} the highest energy levels from which emission is observed are the $^2F(2)_{5/2}$ (63 110 cm^{-1}), $^2F(2)_{7/2}$ (54 390 cm^{-1}), $^4D_{1/2}$ (47 150 cm^{-1}) and the $^2P_{3/2}$ level (31 570 cm^{-1}). Figure 7.1 depicts the schematic energy level diagram of Er^{3+} showing the free-ion levels up to the $^2F(2)_{5/2}$ level at 63 100 cm^{-1}. Levels that show visible emission in LaF_3 are indicated with a filled semicircle, all other levels in the visible and UV region of the spectrum show multi-phonon relaxation to the next lower level.

No correction for the degeneracy of the initial level was applied, since this will not affect the calculated branching ratios. Using the calculated reduced matrix elements $U^{(\lambda)}$ and the assumptions mentioned above it is possible to calculate the visible quantum efficiencies for photon cascade emission that depend only on the values of Ω_2, Ω_4 and Ω_6. By setting two of the three Ω_λ values to zero, the values that are found for the maximum visible quantum efficiency can be used to determine the maximum quantum efficiency that is possible for emission from a certain multiplet. In an actual crystal, with finite values for

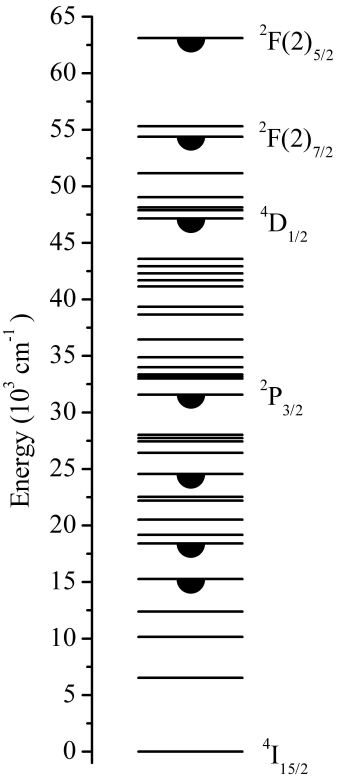

Figure 7.1: Schematic energy level diagram for LaF_3:Er^{3+} up to 65 000 cm^{-1}. Energy levels from which visible emission may be observed are indicated with a filled semicircle.

all three Ω_λ parameters, the visible quantum efficiency will be between "extreme" values that are calculated for the (hypothetical) situation in which only one of the Judd–Ofelt parameters is non–zero.

Any energy level can be chosen as a starting level. The energy gap to the next lower level is used to decide if the level shows emission. If so, then branching ratios for all emissions originating from this level are calculated for each of the three sets of $U^{(\lambda)}$ reduced matrix elements. From the branching ratios the visible, ultraviolet and infrared quantum efficiency for the emissions of the starting level can be calculated. If the starting level is not expected to show emission, its population is added to the next lower level. This process is repeated going down one level at a time until the ground state is reached. If all branching ratios have been calculated, it is possible to evaluate the number of visible photons N_{vis} that can be emitted upon populating N ions into the starting level. The

ratio N_{vis}/N yields the maximum visible quantum yield, which can be calculated independently for values of Ω_2, Ω_4 and Ω_6.

7.4 Results and Discussion

To check the applicability of our calculation method, we calculated the maximum visible quantum efficiency for YF_3:Pr^{3+} using Judd–Ofelt intensity parameter ratios of Ω_2/Ω_6 = 0.013 and Ω_4/Ω_6 = 0.07 as reported by Piper *et al.* [4]. A visible quantum efficiency of 157% was calculated, which is the same as found by Piper *et al.* and Pappalardo [6]. The experimentally observed visible quantum efficiency of YF_3:Pr^{3+} is 140% $\pm$ 15% [4] which is lower than the calculated one, because the calculation method does not consider losses of energy due to impurities and other no–radiative processes that lower the actual quantum efficiency in a real luminescent material.

In the "Blue Report" of Carnall *et al.* [11] the reduced matrix elements were listed for transitions on erbium up to the $^4G_{7/2}$ level at about 28 200 cm^{-1}. For the calculation of transitions to and from the higher energy levels of er^{3+}, tables 7.1 to 7.5 contain reduced matrix elements for transitions involving the high energy levels. In table 7.1 the reduced matrix elements are tabulated for transitions from the $^4I_{15/2}$ ground state to all excited states. Tables 7.2 to 7.5 contain reduced matrix elements for transitions from the $^2P_{3/2}$, $^4D_{1/2}$, $^2F(2)_{7/2}$ and $^2F(2)_{5/2}$ levels to all lower energy levels. For the calculation of the reduced matrix elements we used the computer program of Reid, described in detail in chapter 2.

Using the calculation method described in the previous section we calculated the maximum visible quantum efficiency for photon cascade emission in erbium. Table 7.6 shows the ultraviolet, visible and infrared quantum efficiencies upon excitation into the starting-levels indicated, assuming no non–radiative losses. Quantum efficiencies are listed in three rows, indicated with Ω_2, Ω_4 and Ω_6, for the extreme cases that only one of the parameters Ω_2, Ω_4 or Ω_6 is nonzero.

Table 7.1: Squares of reduced matrix elements $U^{(\lambda)}$ for transitions from the ground state to all excited states up to the $^2F(2)_{5/2}$ state at 63 100 cm^{-1}

Transition		Energy	$\left(U^{(2)}\right)^2$	$\left(U^{(4)}\right)^2$	$\left(U^{(6)}\right)^2$
$^4I_{15/2} \rightarrow$	$^4I_{13/2}$	6516	1.953391E-02	1.172007E-01	1.430466E+00
$^4I_{15/2} \rightarrow$	$^4I_{11/2}$	10150	2.825657E-02	3.022411E-04	3.959048E-01
$^4I_{15/2} \rightarrow$	$^4I_{9/2}$	12384	0	1.589323E-01	6.879329E-03
$^4I_{15/2} \rightarrow$	$^4F_{9/2}$	15267	0	5.535099E-01	4.628935E-01
$^4I_{15/2} \rightarrow$	$^4S_{3/2}$	18403	0	0	2.244118E-01
$^4I_{15/2} \rightarrow$	$^2H(2)_{11/2}$	19167	7.162505E-01	4.134738E-01	9.151088E-02
$^4I_{15/2} \rightarrow$	$^4F_{7/2}$	20516	0	1.466022E-01	6.260557E-01
$^4I_{15/2} \rightarrow$	$^4F_{5/2}$	22195	0	0	2.231645E-01
$^4I_{15/2} \rightarrow$	$^4F_{3/2}$	22519	0	0	1.240454E-01
$^4I_{15/2} \rightarrow$	$^2G(1)_{9/2}$	24556	0	2.152695E-02	2.188979E-01
$^4I_{15/2} \rightarrow$	$^4G_{11/2}$	26426	9.146268E-01	5.255929E-01	1.181624E-01
$^4I_{15/2} \rightarrow$	$^4G_{9/2}$	27437	0	2.361020E-01	1.319018E-01
$^4I_{15/2} \rightarrow$	$^2K_{15/2}$	27735	2.225979E-02	4.109547E-03	7.653175E-02
$^4I_{15/2} \rightarrow$	$^4G_{7/2}$	28024	0	1.944212E-02	1.181282E-01
$^4I_{15/2} \rightarrow$	$^2P_{3/2}$	31568	0	0	1.705492E-02
$^4I_{15/2} \rightarrow$	$^2K_{13/2}$	32998	3.147192E-03	2.903375E-03	1.566346E-02
$^4I_{15/2} \rightarrow$	$^2P_{1/2}$	33175	0	0	0
$^4I_{15/2} \rightarrow$	$^4G_{5/2}$	33347	0	0	2.762925E-03
$^4I_{15/2} \rightarrow$	$^2G(1)_{7/2}$	33998	0	3.355016E-02	2.952361E-03
$^4I_{15/2} \rightarrow$	$^2D(1)_{5/2}$	34869	0	0	2.190434E-02
$^4I_{15/2} \rightarrow$	$^2H(2)_{9/2}$	36449	0	4.937109E-02	1.248140E-04
$^4I_{15/2} \rightarrow$	$^4D_{5/2}$	38652	0	0	2.730884E-02
$^4I_{15/2} \rightarrow$	$^4D_{7/2}$	39346	0	8.855582E-01	2.809146E-02
$^4I_{15/2} \rightarrow$	$^2I_{11/2}$	41139	1.022052E-04	2.745264E-02	3.375220E-03
$^4I_{15/2} \rightarrow$	$^2L_{17/2}$	41694	4.774695E-03	6.731838E-02	3.326225E-02
$^4I_{15/2} \rightarrow$	$^2D(1)_{3/2}$	42300	0	0	1.158354E-02
$^4I_{15/2} \rightarrow$	$^4D_{3/2}$	42933	0	0	1.157719E-03
$^4I_{15/2} \rightarrow$	$^2I_{13/2}$	43587	5.579864E-03	1.755970E-02	5.387361E-03
$^4I_{15/2} \rightarrow$	$^4D_{1/2}$	47150	0	0	0
$^4I_{15/2} \rightarrow$	$^2L_{15/2}$	47880	1.961927E-04	2.741981E-03	2.226391E-03
$^4I_{15/2} \rightarrow$	$^2H(1)_{9/2}$	48131	0	3.685036E-03	7.254680E-05
$^4I_{15/2} \rightarrow$	$^2D(2)_{5/2}$	49032	0	0	9.862959E-03
$^4I_{15/2} \rightarrow$	$^2H(1)_{11/2}$	51155	7.744309E-05	8.334811E-03	6.670523E-05
$^4I_{15/2} \rightarrow$	$^2F(2)_{7/2}$	54389	0	1.488249E-02	6.684364E-05
$^4I_{15/2} \rightarrow$	$^2D(2)_{3/2}$	55316	0	0	8.046529E-04
$^4I_{15/2} \rightarrow$	$^2F(2)_{5/2}$	63110	0	0	3.731320E-08

Table 7.2: Squares of reduced matrix elements $U^{(\lambda)}$ for transitions originating from the $^2P_{3/2}$ level situated at 31 568 cm^{-1} to all lower energy levels.

Transition		Energy	$\left(U^{(2)}\right)^2$	$\left(U^{(4)}\right)^2$	$\left(U^{(6)}\right)^2$
$^2P_{3/2} \rightarrow$	$^4I_{15/2}$	31568	0	0	1.705492E-02
$^2P_{3/2} \rightarrow$	$^4I_{13/2}$	25052	0	0	1.501984E-01
$^2P_{3/2} \rightarrow$	$^4I_{11/2}$	21418	0	1.005387E-01	4.098805E-02
$^2P_{3/2} \rightarrow$	$^4I_{9/2}$	19184	0	4.012983E-02	4.961068E-03
$^2P_{3/2} \rightarrow$	$^4F_{9/2}$	16301	0	4.880246E-02	5.587311E-03
$^2P_{3/2} \rightarrow$	$^4S_{3/2}$	13165	7.963935E-02	0	0
$^2P_{3/2} \rightarrow$	$^2H(2)_{11/2}$	12401	0	1.618818E-02	2.721111E-02
$^2P_{3/2} \rightarrow$	$^4F_{7/2}$	11052	2.048359E-02	8.486319E-03	0
$^2P_{3/2} \rightarrow$	$^4F_{5/2}$	9373	1.776694E-02	4.337817E-02	0
$^2P_{3/2} \rightarrow$	$^4F_{3/2}$	9049	1.297066E-02	0	0
$^2P_{3/2} \rightarrow$	$^2G(1)_{9/2}$	7012	0	2.073039E-01	2.617371E-01
$^2P_{3/2} \rightarrow$	$^4G_{11/2}$	5142	0	2.881470E-02	1.078156E-02
$^2P_{3/2} \rightarrow$	$^4G_{9/2}$	4131	0	1.016293E-02	3.752607E-03
$^2P_{3/2} \rightarrow$	$^2K_{15/2}$	3834	0	0	2.869797E-02
$^2P_{3/2} \rightarrow$	$^4G_{7/2}$	3544	1.217570E-02	4.873522E-04	0

Table 7.3: Squares of reduced matrix elements $U^{(\lambda)}$ for transitions originating from the $^4D_{1/2}$ level situated at 47 150 cm^{-1} to all lower energy levels.

Transition		Energy	$\left(U^{(2)}\right)^2$	$\left(U^{(4)}\right)^2$	$\left(U^{(6)}\right)^2$
$^4D_{1/2} \rightarrow$	$^4I_{15/2}$	47150	0	0	0
$^4D_{1/2} \rightarrow$	$^4I_{13/2}$	40634	0	0	1.495770E-02
$^4D_{1/2} \rightarrow$	$^4I_{11/2}$	37000	0	0	1.518488E-02
$^4D_{1/2} \rightarrow$	$^4I_{9/2}$	34766	0	8.214634E-02	0
$^4D_{1/2} \rightarrow$	$^4F_{9/2}$	31883	0	1.580791E-01	0
$^4D_{1/2} \rightarrow$	$^4S_{3/2}$	28747	3.118394E-02	0	0
$^4D_{1/2} \rightarrow$	$^2H(2)_{11/2}$	27983	0	0	4.695628E-02
$^4D_{1/2} \rightarrow$	$^4F_{7/2}$	26634	0	1.770394E-01	0
$^4D_{1/2} \rightarrow$	$^4F_{5/2}$	24955	8.459202E-02	0	0
$^4D_{1/2} \rightarrow$	$^4F_{3/2}$	24631	1.118488E-01	0	0
$^4D_{1/2} \rightarrow$	$^2G(1)_{9/2}$	22594	0	1.004551E-02	0
$^4D_{1/2} \rightarrow$	$^4G_{11/2}$	20724	0	0	1.557158E-01
$^4D_{1/2} \rightarrow$	$^4G_{9/2}$	19713	0	2.166389E-02	0
$^4D_{1/2} \rightarrow$	$^2K_{15/2}$	19416	0	0	0
$^4D_{1/2} \rightarrow$	$^4G_{7/2}$	19126	0	1.104434E-02	0
$^4D_{1/2} \rightarrow$	$^2P_{3/2}$	15582	1.982918E-03	0	0
$^4D_{1/2} \rightarrow$	$^2K_{13/2}$	14152	0	0	2.466114E-03
$^4D_{1/2} \rightarrow$	$^2P_{1/2}$	13975	0	0	0
$^4D_{1/2} \rightarrow$	$^4G_{5/2}$	13804	2.780160E-01	0	0
$^4D_{1/2} \rightarrow$	$^2G(1)_{7/2}$	13152	0	1.557405E-02	0
$^4D_{1/2} \rightarrow$	$^2D(1)_{5/2}$	12281	7.922444E-02	0	0
$^4D_{1/2} \rightarrow$	$^2H(2)_{9/2}$	10701	0	4.825009E-02	0
$^4D_{1/2} \rightarrow$	$^4D_{5/2}$	8498	6.427968E-04	0	0
$^4D_{1/2} \rightarrow$	$^4D_{7/2}$	7804	0	1.693371E-01	0
$^4D_{1/2} \rightarrow$	$^2I_{11/2}$	6011	0	0	2.836335E-02
$^4D_{1/2} \rightarrow$	$^2L_{17/2}$	5456	0	0	0
$^4D_{1/2} \rightarrow$	$^2D(1)_{3/2}$	4850	2.409400E-01	0	0
$^4D_{1/2} \rightarrow$	$^4D_{3/2}$	4217	8.610514E-03	0	0
$^4D_{1/2} \rightarrow$	$^2I_{13/2}$	3563	0	0	2.721084E-02

Table 7.4: Squares of reduced matrix elements $U^{(\lambda)}$ for transitions originating from the ^{2}F(2)$_{7/2}$ level situated at 54 389 cm^{-1} to all lower energy levels.

Transition		Energy	$\left(U^{(2)}\right)^2$	$\left(U^{(4)}\right)^2$	$\left(U^{(6)}\right)^2$
^{2}F(2)$_{7/2}$ →	^{4}I$_{15/2}$	54389	0	1.488249E-02	6.684364E-05
^{2}F(2)$_{7/2}$ →	^{4}I$_{13/2}$	47873	0	1.771347E-03	1.271621E-03
^{2}F(2)$_{7/2}$ →	^{4}I$_{11/2}$	44239	4.788119E-02	5.164277E-02	2.360191E-04
^{2}F(2)$_{7/2}$ →	^{4}I$_{9/2}$	42005	1.427886E-02	1.041936E-01	4.309259E-05
^{2}F(2)$_{7/2}$ →	^{4}F$_{9/2}$	39122	4.694553E-05	1.293213E-02	8.839698E-03
^{2}F(2)$_{7/2}$ →	^{4}S$_{3/2}$	35986	7.018708E-03	1.386783E-02	0
^{2}F(2)$_{7/2}$ →	^{2}H(2)$_{11/2}$	35222	3.833998E-01	5.238046E-01	3.910455E-03
^{2}F(2)$_{7/2}$ →	^{4}F$_{7/2}$	33873	2.031094E-04	3.961057E-04	1.120666E-02
^{2}F(2)$_{7/2}$ →	^{4}F$_{5/2}$	32194	4.239938E-02	5.386028E-04	2.684387E-03
^{2}F(2)$_{7/2}$ →	^{4}F$_{3/2}$	31870	2.292673E-02	3.605325E-03	0
^{2}F(2)$_{7/2}$ →	^{2}G(1)$_{9/2}$	29833	2.047402E-01	5.665908E-01	2.494966E-02
^{2}F(2)$_{7/2}$ →	^{4}G$_{11/2}$	27963	6.993732E-01	4.551778E-01	5.784810E-04
^{2}F(2)$_{7/2}$ →	^{4}G$_{9/2}$	26952	1.176179E-03	1.098373E-01	9.378602E-03
^{2}F(2)$_{7/2}$ →	^{2}K$_{15/2}$	26655	0	1.928985E-01	1.077022E+00
^{2}F(2)$_{7/2}$ →	^{4}G$_{7/2}$	26365	1.758016E-02	5.409883E-02	4.698095E-02
^{2}F(2)$_{7/2}$ →	^{2}P$_{3/2}$	22821	1.537327E-01	1.363721E-01	0
^{2}F(2)$_{7/2}$ →	^{2}K$_{13/2}$	21391	0	3.731407E-02	4.523586E-01
^{2}F(2)$_{7/2}$ →	^{2}P$_{1/2}$	21214	0	9.371214E-02	0
^{2}F(2)$_{7/2}$ →	^{4}G$_{5/2}$	21043	8.945031E-04	1.490101E-02	1.286084E-02
^{2}F(2)$_{7/2}$ →	^{2}G(1)$_{7/2}$	20391	1.178427E-02	6.342112E-02	5.000151E-02
^{2}F(2)$_{7/2}$ →	^{2}D(1)$_{5/2}$	19520	7.935929E-01	4.607301E-02	9.914596E-03
^{2}F(2)$_{7/2}$ →	^{2}H(2)$_{9/2}$	17940	1.032645E-02	2.391587E-02	7.124092E-02
^{2}F(2)$_{7/2}$ →	^{4}D$_{5/2}$	15737	6.981178E-02	7.838503E-05	1.308718E-02
^{2}F(2)$_{7/2}$ →	^{4}D$_{7/2}$	15043	1.575900E-02	8.233160E-03	1.720987E-03
^{2}F(2)$_{7/2}$ →	^{2}I$_{11/2}$	13250	1.884386E-02	6.971085E-03	4.419348E-01
^{2}F(2)$_{7/2}$ →	^{2}L$_{17/2}$	12695	0	0	5.179839E-01
^{2}F(2)$_{7/2}$ →	^{2}D(1)$_{3/2}$	12089	9.484021E-03	2.081132E-03	0
^{2}F(2)$_{7/2}$ →	^{4}D$_{3/2}$	11456	6.489530E-02	6.687118E-02	0
^{2}F(2)$_{7/2}$ →	^{2}I$_{13/2}$	10802	0	6.503152E-04	1.761652E-01
^{2}F(2)$_{7/2}$ →	^{4}D$_{1/2}$	7239	0	2.110493E-02	0
^{2}F(2)$_{7/2}$ →	^{2}L$_{15/2}$	6509	0	6.763144E-04	4.647919E-02
^{2}F(2)$_{7/2}$ →	^{2}H(1)$_{9/2}$	6258	5.972428E-05	3.040203E-02	2.456805E-01
^{2}F(2)$_{7/2}$ →	^{2}D(2)$_{5/2}$	5357	4.127559E-01	1.230194E-02	3.123084E-02
^{2}F(2)$_{7/2}$ →	^{2}H(1)$_{11/2}$	3235	2.064873E-02	1.156838E-01	1.209876E-01

Table 7.5: Squares of reduced matrix elements $U^{(\lambda)}$ for transitions originating from the $^2F(2)_{5/2}$ level situated at 63 110 cm^{-1} to all lower energy levels.

Transition		Energy	$\left(U^{(2)}\right)^2$	$\left(U^{(4)}\right)^2$	$\left(U^{(6)}\right)^2$
$^2F(2)_{5/2} \rightarrow$	$^4I_{15/2}$	63110	0	0	3.731320E-08
$^2F(2)_{5/2} \rightarrow$	$^4I_{13/2}$	56594	0	1.058019E-02	1.393599E-05
$^2F(2)_{5/2} \rightarrow$	$^4I_{11/2}$	52960	0	9.161540E-03	6.056503E-03
$^2F(2)_{5/2} \rightarrow$	$^4I_{9/2}$	50726	1.943295E-02	1.424206E-02	1.104505E-02
$^2F(2)_{5/2} \rightarrow$	$^4F_{9/2}$	47843	8.311989E-04	5.034247E-03	1.909126E-03
$^2F(2)_{5/2} \rightarrow$	$^4S_{3/2}$	44707	5.324252E-03	5.197777E-03	0
$^2F(2)_{5/2} \rightarrow$	$^2H(2)_{11/2}$	43943	0	2.021703E-02	7.864124E-03
$^2F(2)_{5/2} \rightarrow$	$^4F_{7/2}$	42594	1.213696E-03	3.783181E-03	1.579702E-04
$^2F(2)_{5/2} \rightarrow$	$^4F_{5/2}$	40915	6.674374E-03	1.220195E-04	0
$^2F(2)_{5/2} \rightarrow$	$^4F_{3/2}$	40591	1.288891E-02	2.841269E-03	0
$^2F(2)_{5/2} \rightarrow$	$^2G(1)_{9/2}$	38554	5.407693E-02	9.438310E-03	2.504680E-02
$^2F(2)_{5/2} \rightarrow$	$^4G_{11/2}$	36684	0	1.314667E-02	1.111116E-02
$^2F(2)_{5/2} \rightarrow$	$^4G_{9/2}$	35673	4.890043E-02	1.106948E-01	1.006475E-05
$^2F(2)_{5/2} \rightarrow$	$^2K_{15/2}$	35375	0	0	1.117189E-01
$^2F(2)_{5/2} \rightarrow$	$^4G_{7/2}$	35086	2.015724E-02	7.512604E-03	6.501056E-02
$^2F(2)_{5/2} \rightarrow$	$^2P_{3/2}$	31542	6.222656E-03	2.214679E-02	0
$^2F(2)_{5/2} \rightarrow$	$^2K_{13/2}$	30112	0	2.173382E-02	3.276350E-01
$^2F(2)_{5/2} \rightarrow$	$^2P_{1/2}$	29935	2.312318E-03	0	0
$^2F(2)_{5/2} \rightarrow$	$^4G_{5/2}$	29763	7.588375E-05	7.063682E-03	0
$^2F(2)_{5/2} \rightarrow$	$^2G(1)_{7/2}$	29112	8.113802E-03	8.446030E-02	4.287491E-03
$^2F(2)_{5/2} \rightarrow$	$^2D(1)_{5/2}$	28241	3.103042E-02	3.486548E-03	0
$^2F(2)_{5/2} \rightarrow$	$^2H(2)_{9/2}$	26661	7.245746E-01	9.660469E-01	3.728392E-02
$^2F(2)_{5/2} \rightarrow$	$^4D_{5/2}$	24458	2.492174E-03	4.950820E-03	0
$^2F(2)_{5/2} \rightarrow$	$^4D_{7/2}$	23764	1.524821E-03	1.109456E-02	3.135008E-05
$^2F(2)_{5/2} \rightarrow$	$^2I_{11/2}$	21971	0	3.998432E-02	9.533206E-05
$^2F(2)_{5/2} \rightarrow$	$^2L_{17/2}$	21416	0	0	9.627156E-03
$^2F(2)_{5/2} \rightarrow$	$^2D(1)_{3/2}$	20810	2.686287E-01	8.481251E-02	0
$^2F(2)_{5/2} \rightarrow$	$^4D_{3/2}$	20177	5.970343E-02	5.467364E-02	0
$^2F(2)_{5/2} \rightarrow$	$^2I_{13/2}$	19523	0	1.305413E-01	2.618728E-01
$^2F(2)_{5/2} \rightarrow$	$^4D_{1/2}$	15960	2.692330E-03	0	0
$^2F(2)_{5/2} \rightarrow$	$^2L_{15/2}$	15230	0	0	5.453580E-01
$^2F(2)_{5/2} \rightarrow$	$^2H(1)_{9/2}$	14979	4.410985E-04	1.759168E-01	7.876421E-02
$^2F(2)_{5/2} \rightarrow$	$^2D(2)_{5/2}$	14078	4.929906E-03	5.865036E-05	0
$^2F(2)_{5/2} \rightarrow$	$^2H(1)_{11/2}$	11955	0	3.457037E-02	4.525917E-01
$^2F(2)_{5/2} \rightarrow$	$^2F(2)_{7/2}$	8721	7.617464E-02	1.074694E-02	7.751673E-02
$^2F(2)_{5/2} \rightarrow$	$^2D(2)_{3/2}$	7794	7.816360E-01	7.826820E-02	0

Table 7.6: Calculated maximum visible quantum efficiencies for photon cascade emission of Er^{3+} for different high energy starting levels. The quantum efficiencies indicated for dominant Ω_λ are determined by setting the other two Ω_λ values to zero.

Starting level	Dominant Ω_λ	$\eta_{\mathrm{UV}}(\%)$	$\eta_{\mathrm{VIS}}(\%)$	$\eta_{\mathrm{IR}}(\%)$
	Ω_2	89	79	17
$^2F(2)_{5/2}$	Ω_4	93	92	18
	Ω_6	96	98	7
	Ω_2	84	63	7
$^2F(2)_{7/2}$	Ω_4	94	53	36
	Ω_6	79	112	10
	Ω_2	16	96	8
$^4D_{1/2}$	Ω_4	96	47	83
	Ω_6	67	83	9
	Ω_2	0	78	22
$^2P_{3/2}$	Ω_4	0	107	85
	Ω_6	15	85	5

Contrary to what was suggested in ref. [7] a visible quantum efficiency exceeding 100% is theoretically possible. For emission from the $^2F(2)_{7/2}$ level the theoretical quantum efficiency is 112% if Ω_6 dominates (is much larger than Ω_2 and Ω_4). Emission from the $^2P_{3/2}$ level can exceed 100% for a crystal in which Ω_4 is large compared to the other two Judd-Ofelt parameters. For both levels, however, the quantum efficiency is well below the values that are required for quantum cutting phosphors in a xenon discharge lamp. The extreme cases where only one of the intensity parameters Ω_λ is nonzero do not occur in real crystals, and the actual visible quantum efficiency is always in between the efficiencies calculated. For example, the intensity parameters reported for LaF_3:Er^{3+} (in 10^{-20} cm^2) are Ω_2 = 1.16, Ω_4 = 1.38 and Ω_6 = 0.88 [13]. Using these values the highest visible quantum efficiency calculated is 89% for the $^2F(2)_{5/2}$ level, 72% for the $^2F(2)_{7/2}$ level, 73% for the $^2F(2)_{5/2}$ level and 91% for the $^2P_{3/2}$ starting level.

In the calculations discussed above we assumed that the UV emissions of erbium do not contribute to the visible emission. If an ion can be found that converts the UV emissions of erbium into visible light, for example via a downconversion process or direct energy transfer, without interfering with the photon cascade transitions on the erbium ion,

visible quantum efficiencies between 150 and 190% are possible. This opens new routes to design efficient quantum cutting phosphors by combining Er^{3+} with another luminescent ion.

7.5 Conclusions

We calculated all reduced matrix elements for transitions involving the high energy levels of the Er^{3+} ion. A model was used to predict the maximum visible quantum efficiency for photon cascade emission originating from several (V)UV levels of erbium. For two cases in which only one of the Judd–Ofelt intensity parameters dominates, the visible quantum efficiency may exceed 100% (for emission from the $^2F(2)_{7/2}$ or the $^2P_{3/2}$ level). The maximum visible quantum efficiency is 112% and this is not sufficient for a xenon discharge lamp phosphor. However, if an ion can be found that efficiently converts the UV emissions of erbium into visible light, visible quantum efficiencies between 150 and 190% may be achieved.

References

[1] Dexter, D. L., 1957, Phys. Rev., 108, 630-633.
[2] J. L. Sommerdijk, A. Bril and A. W. de Jager, *J. Lumin.* **8** (1974), 341.
[3] J. L. Sommerdijk, A. Bril and A. W. de Jager, *J. Lumin.* **9** (1974), 288.
[4] W. W. Piper, J. A. DeLuca and F. S. Ham, *J. Lumin.* **8** (1974), 344.
[5] T. Jüstel, H. Nikol and C. Ronda, *Angew. Chem. Int. Ed.* **37** (1998), 3084.
[6] F. Pappalardo, *J. Lumin.* **14** (1976), 159.
[7] R. T. Wegh, E. V. D. van Loef, G. W. Burdick and A. Meijerink, *Mol. Phys.* **101** (2003), 1047.
[8] B. R. Judd, *Phys. Rev.* **127** (1962), 750.
[9] G. S. Ofelt, *J. Chem. Phys.* **37** (1962), 511.
[10] C. Görller-Walrand and K. Binnemans, *Handbook on the Physics and Chemistry of Rare Earths*, Elsevier, Amsterdam (1998) vol 25, p 126.
[11] W. T. Carnall, H. Crosswhite and H. M. Crosswhite, *Energy Level Structure and Transition Probabilities of the Trivalent Lanthanides in LaF_3*, Argonne National Laboratory, Argonne Illinois (1977).
[12] S. Kück, I. Sokólska, M. Henke, M. Döring and T. Scheffler, *J. Lumin.* **102–103** (2003), 176.
[13] M. J. Weber, B. H. Matsinger, V. L. Donlan and G. T. Surratt, *J. Chem. Phys.* **57** (1972), 562.

Appendix A

Table A.1 shows the experimentally observed and calculated energy levels of Gd^{3+} in LaF_3. The first column contains the state having the largest contribution for the energy level calculated. In the second column the experimentally observed energy is shown. In this column, a value in brackets indicates that it is taken from the report of Carnall [1] and was not used in the fitting of parameter values. A value in parentheses indicates that is was observed experimentally, but could not be assigned unambiguously and therefore was not used for the fit and it is assigned to the nearest energy level possible. The column labelled E_{calcVUV} contains the energy levels obtained by fitting the parameter values and the column $\Delta 1$ shows the energy difference between the calculated and observed energy levels. The last two columns contain the energy levels calculated using parameter values reported by Carnall [1] (E_{Carnall}) and the energy difference $\Delta 2$ with the experimentally observed energies. For details see chapter 4.

Table A.1: Energy levels for Gd^{3+} in LaF_3

Energy level (Major component)	E_{exp} (cm^{-1})	E_{calcVUV} (cm^{-1})	$\Delta 1$ (cm^{-1})	E_{Carnall} (cm^{-1})	$\Delta 2$ (cm^{-1})
$^8S_{7/2}$	0	–4	4	0	0
$^8S_{7/2}$	0	–4	4	0	0
$^8S_{7/2}$	0	–4	4	0	0
$^8S_{7/2}$	0	–4	4	0	0
$^6P_{7/2}$	32182	32192	–10	32148	34
$^6P_{7/2}$	32191	32199	–8	32156	35
$^6P_{7/2}$	32205	32213	–8	32174	31
$^6P_{7/2}$	32232	32239	–7	32203	29
$^6P_{5/2}$	[32771]	32797	–26	32753	18
$^6P_{5/2}$	[32791]	32806	–15	32760	31
$^6P_{5/2}$	[32808]	32833	–25	32781	27
$^6P_{3/2}$	[33352]	33398	–46	33348	4
$^6P_{3/2}$	[33370]	33417	–47	33367	3
$^6I_{7/2}$	[35923]	36001	–78	35912	11
$^6I_{7/2}$	[35945]	36019	–74	35922	23
$^6I_{7/2}$	[35968]	36042	–74	35943	25
$^6I_{7/2}$	[35996]	36065	–69	35956	40
$^6I_{9/2}$	[36274]	36347	–73	36255	19
$^6I_{9/2}$	[36285]	36356	–71	36264	21
$^6I_{17/2}$	[36305]	36365	–60	36282	23
$^6I_{17/2}$	[36313]	36366	–53	36290	23
$^6I_{17/2}$	[36332]	36367	–35	36301	31

continued on next page

Table A.1: *continued*

Energy level (Major component)	E_{exp} (cm^{-1})	$E_{calcVUV}$ (cm^{-1})	$\Delta 1$ (cm^{-1})	$E_{Carnall}$ (cm^{-1})	$\Delta 2$ (cm^{-1})
$^6I_{17/2}$	[36340]	36371	–31	36329	11
$^6I_{17/2}$	[36342]	36376	–34	36330	12
$^6I_{9/2}$	[36346]	36380	–34	36330	16
$^6I_{17/2}$	[36351]	36384	–33	36333	18
$^6I_{17/2}$	[36354]	36386	–32	36333	21
$^6I_{9/2}$	[36363]	36391	–28	36334	29
$^6I_{17/2}$	[36370]	36399	–29	36337	33
$^6I_{17/2}$	[36377]	36400	–23	36340	37
$^6I_{9/2}$	[36384]	36410	–26	36344	40
$^6I_{11/2}$	[36549]	36620	–71	36532	17
$^6I_{11/2}$	[36561]	36629	–68	36542	19
$^6I_{11/2}$	[36571]	36640	–69	36550	21
$^6I_{11/2}$	[36584]	36653	–69	36564	20
$^6I_{11/2}$	[36592]	36660	–68	36569	23
$^6I_{11/2}$	[36611]	36680	–69	36584	27
$^6I_{15/2}$	[36659]	36709	–50	36648	11
$^6I_{15/2}$	[36668]	36717	–49	36658	10
$^6I_{15/2}$	[36677]	36726	–49	36662	15
$^6I_{15/2}$	[36687]	36738	–51	36676	11
$^6I_{15/2}$	[36698]	36747	–49	36679	19
$^6I_{15/2}$	[36701]	36756	–55	36686	15
$^6I_{15/2}$	[36710]	36763	–53	36692	18
$^6I_{13/2}$	[36712]	36768	–56	36693	19
$^6I_{13/2}$	[36717]	36771	–54	36694	23
$^6I_{15/2}$	[36722]	36779	–57	36701	21
$^6I_{13/2}$	[36731]	36783	–52	36705	26
$^6I_{13/2}$	[36736]	36791	–55	36707	29
$^6I_{13/2}$	[36749]	36809	–60	36726	23
$^6I_{13/2}$	[36760]	36818	–58	36731	29
$^6I_{13/2}$	[36769]	36829	–60	36739	30
$^6D_{9/2}$	[39667]	39750	–83	39620	47
$^6D_{9/2}$	[39686]	39790	–104	39659	27
$^6D_{9/2}$	[39719]	39818	–99	39686	33
$^6D_{9/2}$	[39742]	39838	–96	39706	36
$^6D_{9/2}$	[39758]	39856	–98	39723	35

continued on next page

Table A.1: *continued*

Energy level (Major component)	E_{exp} (cm^{-1})	$E_{calcVUV}$ (cm^{-1})	$\Delta 1$ (cm^{-1})	$E_{Carnall}$ (cm^{-1})	$\Delta 2$ (cm^{-1})
$^6D_{1/2}$		40764		40598	
$^6D_{7/2}$	[40734]	40841	–107	40709	25
$^6D_{7/2}$	[40740]	40847	–107	40713	27
$^6D_{7/2}$	[40744]	40853	–109	40719	25
$^6D_{7/2}$	[40751]	40862	–111	40729	22
$^6D_{3/2}$		41016		40855	
$^6D_{3/2}$		41037		40881	
$^6D_{5/2}$		41125		40980	
$^6D_{5/2}$		41170		41023	
$^6D_{5/2}$		41182		41036	
$^6G_{7/2}$	49198	49189	9	49134	64
$^6G_{7/2}$	49259	49248	11	49199	60
$^6G_{7/2}$	49267	49261	6	49217	50
$^6G_{7/2}$	49318	49312	6	49259	59
$^6G_{11/2}$	49560	49562	–2	49519	41
$^6G_{9/2}$	49575	49583	–8	49531	44
$^6G_{9/2}$	49623	49646	–23	49601	22
$^6G_{11/2}$	49672	49675	–3	49631	41
$^6G_{9/2}$	49680	49683	–3	49638	42
$^6G_{9/2}$	49699	49707	–8	49667	32
$^6G_{5/2}$	49720	49720	0	49671	49
$^6G_{9/2}$	49746	49733	13	49688	58
$^6G_{5/2}$		49753		49708	
$^6G_{11/2}$		49774		49717	
$^6G_{11/2}$	49769	49786	–17	49733	36
$^6G_{5/2}$	49856	49849	7	49785	71
$^6G_{11/2}$		49856		49797	
$^6G_{11/2}$	49880	49897	–17	49833	47
$^6G_{3/2}$	50551	50524	27	50460	91
$^6G_{3/2}$	50628	50605	23	50543	85
$^6G_{13/2}$	51283	51290	–7	51282	1
$^6G_{13/2}$	51339	51349	–10	51330	9
$^6G_{13/2}$	51361	51365	–4	51357	4
$^6G_{13/2}$	51393	51397	–4	51377	16
$^6G_{13/2}$	51410	51406	4	51392	18

continued on next page

Table A.1: *continued*

Energy level (Major component)	E_{exp} (cm^{-1})	$E_{calcVUV}$ (cm^{-1})	$\Delta 1$ (cm^{-1})	$E_{Carnall}$ (cm^{-1})	$\Delta 2$ (cm^{-1})
$^6G_{13/2}$	51447	51437	10	51409	38
$^6G_{13/2}$	51503	51498	5	51457	46
$^4D(6)_{7/2}$	52395	52395	0	52319	76
$^4D(6)_{7/2}$	52435	52410	25	52333	102
$^4D(6)_{7/2}$	52542	52543	–1	52445	97
$^4D(6)_{7/2}$	52613	52609	4	52516	97
$^6F_{1/2}$	52835	52806	29	52717	118
$^6F_{3/2}$	53789	53801	–12	53700	89
$^6F_{3/2}$	53854	53884	–30	53790	64
$^6F_{11/2}$	54189	54195	–6	54127	62
$^6F_{11/2}$	54213	54219	–6	54151	62
$^6F_{11/2}$	(54335)	54336	–1	54260	75
$^6F_{11/2}$		54351		54278	
$^6G_{5/2}$	(54376)	54386	–10	54297	79
$^6F_{11/2}$	(54400)	54396	4	54303	97
$^6G_{5/2}$		54405		54316	
$^6G_{5/2}$	(54416)	54415	1	54331	85
$^6F_{11/2}$	54480	54479	1	54403	77
$^6F_{9/2}$		54586		54512	
$^6F_{9/2}$		54618		54539	
$^6F_{9/2}$	(54627)	54635	–8	54551	76
$^6F_{9/2}$	(54660)	54682	–22	54609	51
$^6F_{9/2}$	(54700)	54708	–8	54633	67
$^6F_{7/2}$		54775		54668	
$^6F_{5/2}$		54779		54683	
$^6F_{5/2}$	(54803)	54801	2	54692	111
$^6F_{5/2}$	(54826)	54839	–13	54726	100
$^6F_{7/2}$	(54865)	54853	12	54747	118
$^6F_{7/2}$	(54898)	54892	6	54781	117
$^6F_{7/2}$	(54954)	54970	–16	54857	97
$^6G_{9/2}$	55725	55726	–1	55625	100
$^6G_{9/2}$	55741	55732	9	55631	110
$^6G_{9/2}$	55798	55788	10	55688	110
$^6G_{9/2}$	55854	55844	10	55741	113
$^6G_{9/2}$	55888	55878	10	55773	115

continued on next page

Table A.1: *continued*

Energy level (Major component)	E_{exp} (cm^{-1})	$E_{calcVUV}$ (cm^{-1})	$\Delta 1$ (cm^{-1})	$E_{Carnall}$ (cm^{-1})	$\Delta 2$ (cm^{-1})
$^4N_{17/2}$	55997	55986	11	55895	102
$^4N_{17/2}$		55994		55900	
$^4N_{17/2}$	(56013)	55995	18	55904	109
$^4N_{17/2}$	(56020)	56022	–2	55925	95
$^4N_{17/2}$	(56036)	56047	–11	55946	90
$^4N_{17/2}$	(56058)	56052	6	55952	106
$^4N_{17/2}$	(56095)	56102	–7	55994	101
$^4N_{17/2}$		56107		56001	
$^4N_{17/2}$	56138	56137	1	56025	113
$^4H(2)_{7/2}$	(56311)	56309	2	56195	116
$^4D(6)_{3/2}$	(56323)	56330	–7	56218	105
$^4D(6)_{3/2}$	56333	56331	2	56224	109
$^4D(6)_{3/2}$	56365	56375	–10	56256	109
$^4H(2)_{7/2}$		56409		56285	
$^4H(2)_{7/2}$		56473		56343	
$^4H(2)_{13/2}$	56898	56909	–11	56786	112
$^4H(2)_{13/2}$	56921	56915	6	56805	116
$^4H(2)_{13/2}$	56932	56929	3	56814	118
$^4H(2)_{13/2}$	56947	56943	4	56826	121
$^4N_{23/2}$	56964	56957	7	56835	129
$^4H(2)_{13/2}$	56977	56966	11	56849	128
$^4H(2)_{13/2}$	57012	56997	15	56871	141
$^4N_{19/2}$	(57136)	57132	4	57030	106
$^4N_{19/2}$	(57159)	57169	–10	57061	98
$^4N_{19/2}$	(57176)	57175	1	57063	113
$^4N_{19/2}$	(57189)	57185	4	57074	115
$^4N_{19/2}$	(57195)	57192	3	57079	116
$^4N_{19/2}$		57197		57082	
$^4N_{19/2}$		57201		57092	
$^4N_{19/2}$	(57209)	57204	5	57094	115
$^4N_{23/2}$		57216		57102	
$^4N_{23/2}$	(57217)	57218	–1	57113	104
$^4N_{19/2}$	(57226)	57222	4	57115	111
$^4N_{23/2}$		57224		57128	
$^6H_{5/2}$	(57231)	57237	–6	57133	98

continued on next page

Table A.1: *continued*

Energy level (Major component)	E_{exp} (cm^{-1})	$E_{calcVUV}$ (cm^{-1})	$\Delta 1$ (cm^{-1})	$E_{Carnall}$ (cm^{-1})	$\Delta 2$ (cm^{-1})
$^4N_{23/2}$	(57240)	57238	2	57138	102
$^4N_{19/2}$		57249		57140	
$^4N_{23/2}$	(57253)	57253	0	57148	105
$^4N_{19/2}$		57255		57149	
$^6H_{5/2}$		57259		57161	
$^4N_{23/2}$		57263		57163	
$^6H_{5/2}$	(57269)	57273	–4	57169	100
$^6H_{5/2}$	(57279)	57280	–1	57181	98
$^4N_{23/2}$	(57293)	57287	6	57183	110
$^4N_{23/2}$	(57324)	57317	7	57208	116
$^4N_{23/2}$	(57338)	57339	–1	57234	104
$^4N_{23/2}$	(57348)	57354	–6	57240	108
$^4N_{23/2}$	(57363)	57366	–3	57251	112
$^4H(2)_{11/2}$		57413		57312	
$^4H(2)_{11/2}$	57438	57451	–13	57350	88
$^4N_{21/2}$	57452	57473	–21	57374	78
$^4N_{21/2}$	57493	57514	–21	57411	82
$^4N_{21/2}$	(57558)	57584	–26	57475	83
$^4N_{21/2}$	(57606)	57629	–23	57519	87
$^4N_{21/2}$		57648		57542	
$^4N_{21/2}$		57655		57547	
$^4N_{21/2}$		57662		57551	
$^4N_{21/2}$		57671		57560	
$^4N_{21/2}$		57682		57574	
$^4N_{21/2}$		57732		57604	
$^4N_{21/2}$		57732		57610	
$^4N_{21/2}$		57744		57620	
$^4N_{21/2}$		57755		57627	
$^4N_{21/2}$		57802		57671	
$^4N_{21/2}$		57818		57684	
$^6H_{7/2}$	58173	58170	3	58023	150
$^6H_{7/2}$	(58206)	58205	1	58072	134
$^6H_{15/2}$	(58237)	58232	5	58096	141
$^6H_{7/2}$	(58241)	58240	1	58123	118
$^6H_{15/2}$		58254		58125	

continued on next page

Table A.1: *continued*

Energy level (Major component)	E_{exp} (cm^{-1})	$E_{calcVUV}$ (cm^{-1})	$\Delta 1$ (cm^{-1})	$E_{Carnall}$ (cm^{-1})	$\Delta 2$ (cm^{-1})
$^6H_{7/2}$	(58264)	58266	–2	58145	119
$^6H_{15/2}$	(58276)	58274	2	58159	117
$^6H_{15/2}$	(58301)	58299	2	58192	109
$^6H_{15/2}$	(58310)	58314	–4	58194	116
$^6H_{15/2}$		58315		58198	
$^4L(2)_{13/2}$	58329	58320	9	58211	118
$^4L(2)_{13/2}$	(58337)	58333	4	58220	117
$^6H_{15/2}$	(58351)	58341	10	58224	127
$^6H_{15/2}$	(58353)	58346	7	58227	126
$^4L(2)_{13/2}$	(58360)	58363	–3	58248	112
$^6H_{15/2}$	(58370)	58374	–4	58252	118
$^6H_{15/2}$		58374		58263	
$^6H_{15/2}$		58380		58267	
$^6H_{15/2}$		58407		58287	
$^4L(2)_{13/2}$		58423		58297	
$^4N_{17/2}$	58405	58427	–22	58310	95
$^6H_{15/2}$		58437		58314	
$^4L(2)_{15/2}$	58414	58439	–25	58317	97
$^6H_{15/2}$	(58445)	58453	–8	58336	109
$^6H_{15/2}$	(58461)	58472	–11	58349	112
$^4L(2)_{15/2}$	(58480)	58475	5	58362	118
$^4L(2)_{17/2}$	(58494)	58495	–1	58371	123
$^4L(2)_{15/2}$	(58500)	58502	–2	58378	122
$^4L(2)_{15/2}$		58512		58384	
$^4L(2)_{15/2}$	(58514)	58517	–3	58396	118
$^4L(2)_{13/2}$		58526		58400	
$^4L(2)_{13/2}$	(58546)	58536	10	58408	138
$^4L(2)_{15/2}$	(58556)	58579	–23	58442	114
$^4L(2)_{13/2}$	(58582)	58597	–15	58449	133
$^4L(2)_{13/2}$	(58626)	58626	0	58476	150
$^4L(2)_{13/2}$		58637		58491	
$^6H_{11/2}$		58660		58504	
$^6H_{11/2}$	(58671)	58673	–2	58525	146
$^6H_{11/2}$		58692		58548	
$^6H_{11/2}$	(58704)	58704	0	58562	142

continued on next page

Table A.1: *continued*

Energy level (Major component)	E_{exp} (cm^{-1})	$E_{calcVUV}$ (cm^{-1})	$\Delta 1$ (cm^{-1})	$E_{Carnall}$ (cm^{-1})	$\Delta 2$ (cm^{-1})
$^6H_{11/2}$		58715		58565	
$^6H_{11/2}$		58721		58570	
$^6H_{9/2}$	58729	58744	–15	58593	136
$^6H_{9/2}$		58747		58608	
$^6H_{9/2}$	58770	58764	6	58615	155
$^6H_{9/2}$		58832		58673	
$^6H_{9/2}$	58828	58845	–17	58681	147
$^6H_{13/2}$	59781	59774	7	59654	127
$^6H_{13/2}$	59804	59793	11	59676	128
$^6H_{13/2}$	59815	59809	6	59697	118
$^6H_{13/2}$	59836	59821	15	59705	131
$^6H_{13/2}$	59849	59838	11	59717	132
$^6H_{13/2}$	59895	59882	13	59760	135
$^6H_{13/2}$	59933	59918	15	59796	137
$^4L(2)_{19/2}$	60192	60175	17	60042	150
$^4L(2)_{19/2}$	60233	60213	20	60078	155
$^4L(2)_{19/2}$		60214		60081	
$^4L(2)_{19/2}$		60220		60089	
$^4L(2)_{19/2}$		60233		60098	
$^4L(2)_{19/2}$		60239		60105	
$^4L(2)_{19/2}$		60242		60113	
$^4L(2)_{19/2}$		60255		60114	
$^4L(2)_{19/2}$		60258		60117	
$^4L(2)_{19/2}$		60260		60119	
$^4K(1)_{11/2}$		60341		60274	
$^4K(1)_{11/2}$		60354		60279	
$^4K(1)_{11/2}$		60425		60332	
$^4K(1)_{11/2}$		60443		60353	
$^4K(1)_{11/2}$		60464		60368	
$^4K(1)_{11/2}$		60498		60399	
$^4F(4)_{9/2}$	60927	60920	7	60746	181
$^4F(4)_{9/2}$	60964	60980	–16	60813	151
$^4F(4)_{9/2}$	61016	61004	12	60829	187
$^4F(4)_{9/2}$	61075	61073	2	60889	186
$^4F(4)_{9/2}$	61088	61094	–6	60912	176

continued on next page

Table A.1: *continued*

Energy level (Major component)	E_{exp} (cm^{-1})	$E_{calcVUV}$ (cm^{-1})	$\Delta 1$ (cm^{-1})	$E_{Carnall}$ (cm^{-1})	$\Delta 2$ (cm^{-1})
$^4F(4)_{7/2}$	61334	61339	–5	61178	156
$^4F(4)_{7/2}$	61344	61349	–5	61184	160
$^4F(4)_{7/2}$	61365	61365	0	61198	167
$^4F(4)_{7/2}$	61388	61388	0	61215	173
$^4F(4)_{5/2}$		62415		62287	
$^4F(4)_{5/2}$		62452		62311	
$^4F(4)_{5/2}$		62468		62337	

References

[1] W. T. Carnall, G. L. Goodman, K. Rajnak and R. S. Rana, *A Systematic Analysis of the Spectra of the Lanthanides Doped into Single Crystal LaF_3* Argonne National Laboratory, Argonne Illinois (1988).

Samenvatting

Dit proefschrift beschrijft **spectroscopie** van **lanthanide–ionen**.

Spectroscopie is de studie van de interactie tussen licht en materie. Licht kan beschreven worden als een golf (elektromagnetische golf) of als deeltjes (fotonen). Een handige maat voor de energie van de fotonen is golfgetallen (cm^{-1}). Veel inzichtelijker is echter vaak de golflengte van het licht, in nanometers (nm). Een nanometer is een miljardste meter. Energie en golflengte van licht zijn omgekeerd evenredig, dat wil zeggen dat hoe hoger de energie per foton, hoe korter de golflengte van het licht. Zichtbaar licht heeft een golflengte tussen 380 nm (violet) en 750 nm (rood). Een regenboog laat al deze kleuren zien, op volgorde van energie.

Licht met een langere golflengte dan rood heet infrarood, totdat de golflengte zo ongeveer een millimeter is. Hierna begint het gebied van de microgolven en radiogolven, met golflengtes tot duizenden meters. Infrarood licht wordt bijvoorbeeld gebruikt in afstandsbedieningen en warmtelampen. Microgolven met een golflengte van ongeveer 12 cm worden in de magnetron gebruikt om het eten op te warmen en mobiele telefoons gebruiken straling met een golflengte van een paar cm.

Licht met een kortere golflengte dan violet (en dus een hogere energie) heet ultraviolet (UV). UV-straling met een relatief lage energie, tussen 320 en 380 nm, zorgt voor de aanmaak van pigment (kleurstof) in de huid. Het golflengtegebied tussen 50 en 200 nanometer heet **vacuümultraviolet** (VUV) omdat straling met deze golflengte door zuurstof geabsorbeerd wordt. Veel van de spectroscopie beschreven in dit proefschrift is gedaan in dit golflengtegebied.

Kan de golflengte nog korter? Ja, dat kan. Dan heet het röntgenstraling, bekend van de foto's in het ziekenhuis, en als de golflengte dan nòg korter wordt, in de grootte orde van een biljoenste meter en kleiner, spreken we van gammastraling.

Spectroscopisch onderzoek kan in al deze golflengtegebieden gedaan worden. Dit proefschift beschrijft onderzoek in met name het ultraviolette en het vacuümultraviolette deel van het elektromagnetische spectrum.

Een stof die (UV–)straling absorbeert en vervolgens zichtbaar licht uitzendt wordt ook wel een fosfor genoemd. In tl–verlichting en televisieschermen worden fosforen met

lanthanide–ionen toegepast om zichtbaar licht te maken. Deze lanthanide–ionen vormen een aparte groep van elementen in het periodiek systeem en hebben bijzondere spectroscopische eigenschappen. De elementen worden afgekort met twee letters, bijvoorbeeld gadolinium met Gd. Een atoom met een lading heet een **ion** en alle lanthaniden komen als driewaardige ionen voor. Het gadoliniumion wordt dus genoteerd als Gd^{3+}.

Lanthanide–ionen komen –zoals hierboven al genoemd– voor in veel toepassingen die met licht te maken hebben. De ionen komen niet "los" voor, maar zijn ingebouwd in een kristalrooster. Een deel van de ionen in een kristal zijn dan vervangen door ionen van lanthaniden. In dit proefschrift worden die stoffen genoteerd als Rooster:Ion. LaF_3:Gd^{3+} 1% is dus lanthaanfluoride (LaF_3) met 1% van de La^{3+} ionen vervangen door Gd^{3+} ionen.

De namen van de lanthanide–ionen zijn soms eenvoudig (Ce = cerium), maar soms lastig (Pr = praseodymium). Sommige klinken bekend, zoals europium (Eu), en het is geen toeval dat de lichtgevende stoffen die de Eurobiljetten beveiligen allemaal europiumverbindingen zijn. Bij de kassa lichten deze verbindingen op onder de UV–lamp.

Een kort overzicht van de geschiedenis van de spectroscopie van lanthanide–ionen is opgenomen in hoofdstuk 1 van dit proefschrift. Door de absorptie en emissie van licht door lanthanide–ionen te meten, kom je iets te weten over de energieniveaus van de ionen. Normaal zijn alle ionen in de grondtoestand, de toestand met de laagste energie. Door licht te absorberen kan een ion vanuit de grondtoestand overgaan in een aangeslagen toestand. In figuur 1.1 staat een overzicht van de lanthanide–ionen met hun (lagere) energieniveaus aangegeven als horizontale streepjes. Alleen als een foton de energie heeft die gelijk is aan het energieverschil tussen de grondtoestand en een bepaalde aangeslagen toestand, kan het foton geabsorbeerd worden en komt het ion in die aangeslagen toestand, anders gebeurt er niets. De aangeslagen toestand is maar tijdelijk, want een ion in de aangeslagen toestand is energetisch minder gunstig dan een ion in de grondtoestand. Onder uitzending van licht keert het ion weer terug naar de grondtoestand. Het uitgezonden foton heeft dan de energie gelijk aan het verschil tussen aangeslagen toestand en eindtoestand. Die eindtoestand hoeft niet per se meteen de grondtoestand te zijn. Via een van de vele niveaus onder de aangeslagen toestand komt het ion uiteindelijk weer in de grondtoestand, onder uitzending van fotonen.

De verschillende energieniveaus van een lanthanide ion ontstaan door interacties tussen de elektronen van het ion, en dan met name de zogenaamde **4f–elektronen**. Deze elektronen doen niet mee aan de binding in een kristal en worden door andere elektronen een beetje afgeschermd van de omgeving. Dit heeft tot gevolg dat de 4f–elektronen van een ion, bijvoorbeeld europium, weinig beinvloed worden door de ionen van het kristalrooster. De energieniveaus zijn dan ook in verschillende kristallen ongeveer gelijk. Er zijn nog steeds duidelijk meetbare verschillen, maar een emissiespectrum is vaak wel herkenbaar als een typisch europium spectrum.

Energieniveaus worden aangeduid met een **termsymbool**. Zoals hierboven al vermeld werd, ontstaan de energieniveaus door interactie tussen de 4f–elektronen. Er zijn verschillende configuraties mogelijk, die allemaal met een zogeheten termsymbool kunnen worden aangegeven. Zo is de grondtoestand van Ce^{3+} bijvoorbeeld $^2F_{5/2}$. Een termsymbool ziet er altijd uit als $^{A}B_{C}$. De betekenis van A, B en C valt (helaas) buiten het bestek van deze samenvatting, maar termsymbolen zijn handige "labels" voor energieniveaus.

Door de energie te meten van de geabsorbeerde en uitgezonden fotonen (met respectievelijk een absorptie– en een emissiespectrum) kunnen de energieniveaus van de lanthanide–ionen bepaald worden. Dit is hoe figuur 1.1 tot stand is gekomen, met behulp van infrarood, zichtbaar en ultraviolet licht. Figuur 1.1 gaat tot ongeveer 40 000 cm^{-1} in energie. De energieniveaus bestudeerd in dit proefschrift liggen nog hoger, in het vacuüm–ultraviolet. Dit klinkt eenvoudiger dan het is, want lang niet alle energieniveaus kunnen emissie geven, en sommige absorpties en emissies zijn heel erg zwak. Bovendien is voor meting van VUV niveaus ook een lichtbron nodig die de VUV fotonen levert.

Metingen in het UV en zichtbare deel van het spectrum kunnen worden gedaan met xenon ontladingslampen en halogeenlampen. Voor het VUV is er wel de deuteriumlamp, maar die zendt alleen zwak VUV straling uit. **Synchrotrons** zijn deeltjesversnellers. Bij het DESY synchrotron in Hamburg worden positronen (dat zijn positief geladen elektronen) versneld en opgeslagen in een synchrotronring. Wisselende magnetische en elektrische velden zorgen ervoor dat de positronen hun snelheid behouden en iedere keer als ze "door de bocht" gaan, zenden de positronen intense straling uit, van het infrarood tot röntgenstraling, en dus ook VUV. Bij de HIGITI meetopstelling wordt deze straling gebruikt voor VUV spectroscopie. Een **monochromator** wordt gebruikt om uit een breed spectraal gebied één golflengte te selecteren.

Naast meten is het ook mogelijk energieniveaus te berekenen door de interacties tussen de 4f–elektronen te beschrijven met een model. Dit wordt beschreven in hoofdstuk 2. Moderne computers zijn snel genoeg om in een paar seconden tot een tiental minuten alle energieniveaus uit te rekenen. Dit is gedaan voor alle lanthanide–ionen in LaF_3 en het resultaat is te zien in figuur 2.2. Lang niet al deze niveaus kunnen gemeten worden, doordat er bijvoorbeeld bij hogere energieën ook andere processen plaatsvinden waardoor de absorpties niet meer goed waar te nemen zijn.

Met nauwkeurige metingen van de energieniveaus is het ook mogelijk de berekeningen te verbeteren. Het model wordt niet aangepast, maar de parameters die de invloed van de verschillende interacties tussen de elektronen beschrijven worden nauwkeuriger bepaald. Een ander gebruik van de berekeningen is het voorspellen van energieniveaus die emissie kunnen geven. Het is ook mogelijk een emissiespectrum te simuleren, gebaseerd op de berekende energieniveaus.

Een voorbeeld van een voorspelde emissie is beschreven in hoofdstuk 3. Dit hoofdstuk gaat over het ion holmium (Ho^{3+}). Uit energieniveauberekeningen bleek dat holmium een

energieniveau heeft in het VUV–gebied van het spectrum, dat emissie kan geven. Dit is het ^{3}P(1)$_2$ niveau. Emissie uit dit niveau werd waargenomen voor YF_3:Ho^{3+}, maar niet voor $LiYF_4$:Ho^{3+}. De oplettende lezer fronst nu even, want zojuist was nog te lezen dat energieniveaus ongeveer gelijk zijn in verschillende kristallen. Dat is inderdaad waar voor de 4f–energieniveaus, maar niet voor zogeheten **4f^{n-1}5d niveaus**.

Bij een bepaalde hoge energie kan een 4f–elektron naar een andere elektronenbaan (orbitaal) springen. In het geval van lanthanide–ionen is dit de 5d–orbitaal. Vanuit een configuratie met n 4f–elektronen ontstaat een configuratie met n–1 4f–elektronen en één 5d–elektron. Dit wordt genoteerd als 4f^{n-1}5d. Overgangen tussen verschillende 4f–niveaus zijn erg zwak en zijn in de spectra te zien als lijnen. Overgangen naar een 4f^{n-1}5d niveau zijn veel intenser, en in de spectra te zien als bredere banden. In $LiYF_4$ ligt de 4f^{n-1}5d band van holmium precies over het ^{3}P(1)$_2$ niveau, en in YF_3 net erboven. Daardoor kan in YF_3 wel emissie worden waargenomen vanuit het ^{3}P(1)$_2$ niveau, en in LaF_3 kan dat niet. Hoofdstuk 3 beschrijft ook andere VUV energieniveaus die gemeten zijn voor holmium met behulp van synchrotronstraling.

Een blik op figuur 1.1 laat zien dat gadolinium (Gd^{3+}) een bijzonder energieniveauschema heeft. De eerste aangeslagen toestand ligt veel hoger dan die van andere lanthanide–ionen, namelijk in het UV rond de 32 000 cm^{-1}. Gadolinium heeft geen energieniveaus in het infrarood en in het zichtbare deel van het spectrum. Vergelijking met figuur 2.2 maakt meteen duidelijk dat de meeste energieniveaus van gadolinium boven de 40 000 cm^{-1} ligt. In het verleden zijn niet veel van die hogere niveaus gemeten. In de zestiger en zeventiger jaren zijn de niveaus tot 49 000 cm^{-1} nauwkeurig gemeten. Met synchrotronstraling was het in de negentiger jaren mogelijk om de VUV niveaus te meten, tot 68 000 cm^{-1}. De meetapparatuur had wel een beperkte meetnauwkeurigheid, en alleen groepjes van energieniveaus konden worden gemeten.

De parameters voor de berekening van de energieniveaus van gadolinium zijn niet zo goed voor het berekenen van de hogere niveaus. Dit komt doordat de parameters alleen geoptimaliseerd konden worden op de lagere energieniveaus en dat waren er niet zoveel. Gadolinium heeft ongeveer 1700 energieniveaus, en slechts de 70 laagste waren nauwkeurig gemeten. Om de parameters voor gadolinium te verbeteren zouden die VUV niveaus zeer nauwkeurig gemeten moeten worden. Synchrotrons zijn zeer intens in het VUV, maar niet nauwkeurig op een energie (golflengte) afstembaar. Lasers zijn nog veel intenser, erg nauwkeurig afstembaar, alleen niet in het VUV. Twee oplossingen voor dit probleem worden beschreven in hoofdstuk 4. Door het gebruik van twee lasers, wordt de energie van twee fotonen gecombineerd om in twee stappen tot een hoge energie te komen, met behoud van de nauwkeurigheid van de laser.

Excited state absorptie is de eenvoudigste van de twee oplossingen voor het meetprobleem, hoewel de experimenten nog steeds erg lastig blijven. Door een ion in twee stappen in een aangeslagen toestand te brengen, kunnen hoge energieniveaus gemeten

worden. Door gadolinium eerst in de eerste aangeslagen toestand te brengen (het $^6P_{7/2}$–niveau), met een laser die UV–fotonen uitzendt van de juiste energie (namelijk die van het energieverschil tussen de aangeslagen toestand en de grondtoestand), kan vervolgens met een tweede laser vanuit de aangeslagen toestand een VUV niveau bereikt worden. Hiervoor is een afstembare laser nodig, een kleurstof–laser. Met behulp van verschillende kleurstoffen in het mogelijk een laser te maken die over een bepaald golflengtegebied (en dus energiegebied) is af te stemmen. Deze techniek heet excited state absorption, dat wil zeggen: absorptie uit een aangeslagen toestand. Met behulp van de excited state absorption metingen was het mogelijk om de VUV niveaus van gadolinium tussen 49 000 en 62 000 cm^{-1} nauwkeurig te meten. Met behulp van de gemeten energieniveaus werd vervolgens de set parameters voor de energieniveauberekeningen verbeterd. De nieuwe set parameter waarden geeft een betere beschrijving van de hogere energieniveaus.

De hiervoor genoemde $4f^{n-1}5d$ niveaus komen terug in hoofdstuk 5. In de kristallen $LiYF_4$ (lithiumyttriumfluoride) en YPO_4 (yttriumfosfaat) kunnen de ionen cerium, praseodymium, neodymium, erbium en thulium emissie geven uit de $4f^{n-1}5d$ niveaus. De emissies zijn intens en in de spectra te zien als brede banden. Door het berekeningsmodel voor de 4f–niveaus uit te breiden met parameters die de interacties van het 5d–elektron beschrijven, is het mogelijk ook de $4f^{n-1}5d$ energieniveaus en $4f^n \leftrightarrow 4f^{n-1}5d$ spectra te berekenen.

Voor de absorptiespectra is dit een paar jaar geleden al aangetoond, maar het was toen nog niet mogelijk om de $4f^{n-1}5d$ emissiespectra nauwkeurig te meten. Met een goede monochromator zijn deze spectra nu wel gemeten en in hoofdstuk 5 worden ze vergeleken met de berekende spectra. Het model blijkt goed te werken, want de gemeten emissiespectra worden door de berekeningen goed gereproduceerd.

Alle kennis verkregen uit de berekeningen en met name uit de experimenten is van nut voor **toepassingen van lanthanide–ionen**. De fosforen in moderne tl–buizen zijn gebaseerd op lanthanide–ionen. In een tl–buis zit een beetje kwik en door een spanning over de elektroden aan te leggen raken de kwikatomen door botsingen met elektronen in aangeslagen toestand. Een kwikatoom dat terugvalt naar de grondtoestand zendt UV fotonen uit. Slechts 3% van het uitgezonden licht is zichtbaar licht. Door nu de wand van de buis aan de binnenkant te bedekken met een laagje fosforen die het UV absorberen en zichtbaar licht uitzenden, kan een efficiënte lichtbron gemaakt worden. Tegenwoordig wordt meestal een combinatie van drie fosforen gebruikt, één voor rood, één voor groen en één voor blauw licht. Samen geeft dit wit licht.

Hoewel de tl–buis veel efficiënter is dan bijvoorbeeld een gloeilamp, wordt uit milieu–overwegingen gezocht naar een alternatief. Het kwik in de buis is schadelijk voor het milieu en bovendien duurt het soms even voordat het (vloeibare) kwik verdampt is na het aanzetten van de lamp. Deze opstarttijd maakt de tl–buis ongeschikt voor bijvoorbeeld remlichten. Een alternatief voor de kwikontlading is **xenon**. Xenon is een gas bij

kamertemperatuur en een xenonlamp gaat onmiddellijk licht geven bij inschakeling. Er is wel een nadeel: de xenonontlading zendt VUV–straling uit, bij 147 en 172 nm. De fosforen in de huidige tl–buizen zijn geoptimaliseerd voor de kwikontlading bij 254 nm. Onderzoek aan VUV niveaus van lanthaniden kan een bijdrage leveren aan de ontwikkeling van nieuwe fosforen voor de xenonlamp en ook voor plasmaschermen waarin dezelfde VUV–straling wordt omgezet in rood, groen of blauw licht.

Een ander nadeel is dat er bij het omzetten van een UV foton van de kwikontlading in een zichtbaar foton ongeveer 50% van de energie verloren gaat. Met de huidige fosforen in combinatie met de xenonontlading is het energieverlies alleen maar groter, zo'n 65%. Een mogelijke oplossing is het gebruik van **kwantumknippers**. Dit zijn fosforen die een VUV foton absorberen en vervolgens twee zichtbare fotonen uitzenden. De kwantumefficiëntie, dat is het aantal uitgezonden fotonen gedeeld door het aantal geabsorbeerde fotonen, ligt dan boven de 100%. Onderzoek gedaan in onze groep aan de VUV niveaus van lanthanide–ionen heeft in de jaren negentig tot de ontdekking van zo'n kwantumknipper geleid. De fosfor $LiGdF_4$:Eu^{3+} kan VUV fotonen omzetten in oranje/rood licht, met een kwantumefficiëntie van ongeveer 190%.

Voor de ontwikkeling van een lamp met kwantumknippende fosforen, gebaseerd op de xenon ontlading is echter nog meer nodig. Voor de meeste toepassingen is wit licht gewenst, en naast een rode is ook nog een groene en blauwe kwantumknipper nodig. En dat is nog steeds niet voldoende. De absorpties van lanthanide–ionen zijn, zoals eerder genoemd, zwak. Dit betekent dat hoewel de kwantumknipper een rendement van 190% heeft, dit alleen maar iets zegt over de efficiëntie van de omzetting van geabsorbeerde VUV fotonen. Verreweg het grootste deel van de VUV fotonen wordt niet geabsorbeerd door de fosfor. Een oplossing hiervoor is een zogenaamde **sensitizer**. Dit is een ion dat goed VUV fotonen kan absorberen en de energie vervolgens kan overdragen aan de kwantumknippende ionen.

Thulium (Tm^{3+}) is een ion dat goed absorbeert in het VUV. De $4f^{n-1}5d$ niveaus van thulium liggen in het VUV gebied van het spectrum en overgangen naar deze niveaus zijn intens. Uit voorgaand onderzoek is bekend dat thuliumionen goed energie kunnen overdragen naar gadoliniumionen. Het gebruik van thulium als een sensitizer voor de gadolinium–europium kwantumknipper wordt beschreven in hoofdstuk 6 van dit proefschrift. Thulium blijkt helaas niet geschikt, want na overdracht van de energie aan gadolinium vindt het kwantumknippen met europium niet plaats. De gadoliniumionen dragen een deel van de energie weer over aan thuliumionen, die vervolgens infrarood licht uitzenden.

Een andere vorm van kwantumknippen is het achtereenvolgens uitzenden van twee zichtbare fotonen door een en hetzelfde lanthanide ion, de zogenaamde **foton–cascade emissie**. Na absorptie van een VUV foton kan een ion een zichtbaar foton uitzenden en belandt dan in een lagere aangeslagen toestand. Door vervolgens nog een zichtbaar foton

uit te zenden kan ook een kwantumefficiëntie van boven de 100% behaald worden. Dit was is de jaren zeventig al bekend voor praseodymium (Pr^{3+}). Na absorptie van een VUV foton kan een praseodymiumion eerst een violet foton uitzenden en vervolgens een rood of een groen foton.

Een ander ion waar foton–cascade emissie mogelijk is, is het erbiumion (Er^{3+}). Erbium heeft net als praseodymium een geschikt energieniveauschema om achtereenvolgens twee zichtbare fotonen uit te kunnen zenden. Uit het bestuderen van eerder gemeten emissiespectra van erbium werd geconcludeerd dat foton–cascade emissie voor erbium geen kwantumefficiëntie voor zichtbaar licht boven de 100% zal opleveren, omdat de meest intense erbium emissies in het UV liggen. In het laatste hoofdstuk van dit proefschrift wordt met behulp van Judd–Ofelt theorie de maximale efficiëntie voor foton–cascade emissie van zichtbaar licht uitgerekend. In theorie blijkt het mogelijk om een zichtbaar rendement van 112% te halen, maar dit is te laag om, wanneer toegepast in een xenon–ontladingslamp, een lamp te maken die efficiënter is dan de huidige tl–buizen.

Publications

This thesis is based on the following publications:

- *A complete $4f^n$ energy–level diagram for all trivalent lanthanide ions*, P. S. Peijzel, A. Meijerink, R. T. Wegh, M. F. Reid and G. W. Burdick. Accepted for publication in the Journal of Solid State Chemistry. *Chapter 2.*

- *High energy levels and high–energetic emissions of the trivalent holmium ion in $LiYF_4$ and YF_3*, P. S. Peijzel, R. T. Wegh, A. Meijerink, J. Hölsä and R. J. Lamminmäki. Optics Communications **204** (2002), 195. *Chapter 3.*

- *Probing vacuum ultraviolet energy levels of trivalent gadolinium by two–photon spectroscopy*, P. S. Peijzel, W. J. M. Schrama, M. F. Reid and A. Meijerink. Journal of Luminescence **102–103** (2001), 211. *part of Chapter 4.*

- *High–resolution measurements of the vacuum ultraviolet energy levels of trivalent gadolinium by excited state absorption*, P. S. Peijzel, P. Vermeulen, W. J. M. Schrama, G. W. Burdick, M. F. Reid, and A. Meijerink. Manuscript in preparation. *Chapter 4.*

- *$4f^{n-1}5d \rightarrow 4f^n$ emission of Pr^{3+} Nd^{3+} Er^{3+} and Tm^{3+} in $LiYF_4$ and YPO_4*, P. S. Peijzel, P. Vergeer, G. W. Burdick, M. F. Reid and A. Meijerink. Manuscript in preparation. *Chapter 5.*

- *Thulium as a sensitizer for the Gd^{3+}/Eu^{3+} quantum cutting couple*, P. S. Peijzel, W. J. M. Schrama and A. Meijerink. Accepted for publication in Molecular Physics. *Chapter 6.*

- *Visible photon cascade emission from the high energy levels of Er^{3+}*, P. S. Peijzel and A. Meijerink. Manuscript in preparation. *Chapter 7.*

Other publications:

- *Luminescence of exchange coupled pairs of transition metal ions*, A. P. Vink, M. A. de Bruin, S. Roke, P. S. Peijzel and A. Meijerink. Journal of the Electrochemical Society **148** (2001), E313.
- *Site–selective laser spectroscopy of $4f^n \rightarrow 4f^{n-1}5d$ transitions in CaF_2:Pr^{3+} with F^-, D^-, H^-, Li^+, or Na^+ charge compensation*, L. van Pieterson, R. P. A. Dullens, P. S. Peijzel, A. Meijerink and G. D. Jones. Journal of Chemical Physics **115** (2001), 9393.

Patent:

- *Gas discharge lamp with down conversion luminophore*, C. Feldmann, A. Meijerink, K. Oskam and P. Peijzel, US2002185961, filed 12-12-2002.

Dankwoord

Gezien de “leesfrequentie” van het dankwoord zou het beter als hoofdstuk 1 van het proefschrift opgenomen kunnen worden, of nog beter als een uitneembare bijlage. Maar een dankwoord heeft te maken met terugkijken en dus staat het hier. Het is een van de lastigste onderdelen van een proefschrift, want iemand vergeten te noemen schijnt niet te mogen. Een naam verkeerd spellen kan echter ook verkeerd vallen en mijn achternaam leent zich daar uitstekend voor ....

Mijn promotor, Andries Meijerink, wil ik als eerste bedanken. In de afgelopen vier jaar kon ik altijd bij je langskomen, zowel met onderzoeksproblemen als met flippo's, spinners, chaps en luminescerend “speelgoed”. De experimenten waren af en toe verre van eenvoudig, maar je bent niet iemand die snel opgeeft. Lasers en electronische componenten vertoonden echter soms wel die neiging, maar je wist ze altijd snel weer tot meewerken te motiveren. Onderzoek is nooit af, en hoewel onlangs het tegendeel werd beweerd, is de puzzel van de lanthaniden ook nog niet af.

Cees Ronda wil ik bedanken voor de vele colleges, waarbij duidelijk werd dat materiaalkundig onderzoek en industriële vraagstukken onlosmakelijk met elkaar verbonden zijn. Deze combinatie levert niet alleen uitdagend onderzoek op, maar geeft ook aanleiding tot leuke discussies en niet alleen over wetenschap.

Next, I would like to thank Mike Reid from the university of Canterbury in Christchurch, New Zealand. Thank you for all your help with the computer programs, for your contribution to the articles and for the time you spent on helping me with my calculations, during your visits to Utrecht and over e–mail.

Gary Burdick from Andrews University, Berrien Springs, visited our group for ten weeks and helped me with the energy level calculations of gadolinium and simulation of f–d emission spectra. I want to thank you for giving me more insight in the calculations, for turning the library upside down in order to find valuable articles and also for the quick and thorough reading of my manuscripts.

I would like to thank Professor Jorma Hölsä and Ralf–Johan Lamminmäki (University of Turku, Finland) for performing the energy–level calculations of holmium.

Lynn Boatner from Oak Ridge National Laboratory kindly provided the YPO_4 crystals

doped with neodymium and gadolinium. These crystals were very useful and one of the resulting beautiful emission spectra can be admired in chapter 5.

Mijn onderzoek is alleen mogelijk geweest met de technische assistentie van Hans Ligthart. Hans, ik zal de kopjes koffie 's ochtends missen. Dankzij jouw inzet kreeg ik een mooie tafel voor de kryostaat en een filterhouder die lekkende fotonen geen kans gaf. Johan Keijzer, Nico Kuipers en Jan van Eijk wil ik bedanken voor de honderden liters vloeibaar helium, die jullie van mij weer in de gasfase terugkregen. Stephan Zevenhuizen was altijd bereid om computers tot functioneren te krijgen en de meetsoftware aan te passen aan nieuwe apparatuur. Ook de technici van de fysica groepen, Cees de Kok, Ger$\frac{ard}{rit}$ van Lingen en Paul Jurrius waren altijd bereid te helpen bij het klussen aan een laser of aan mijn fiets.

De overige leden van de vaste staf van de GCM/CCM groep, John Kelly, Daniël Vanmaekelbergh en Celso de Mello Donegá, wil ik bedanken voor de prettige werksfeer op de vakgroep. Recentelijk werd de sectie uitgebreid tot CMI, en de "Interface" collega's vormden geen grensvlak en maakten de groep nog gezelliger. Harold de Wijn verzorgde enthousiast colleges voor promovendi, waar ik helaas tijdens het schrijven van dit proefschrift niet meer bij kon zijn.

De afgelopen vier jaar heb ik met meerdere kamergenoten te maken gehad. Ik begon op de tweede verdieping van het Ornsteinlab bij Xinghua Xia. Na een aantal maanden ging Xinghua naar China, maar ik bleef niet alleen achter, want Sander kwam mij gezelschap houden. In vele kamers, want door de verhuizingen binnen het gebouw hebben we alle hoeken gezien, en zelfs een weekje op de röntgenkamer mocht daaraan niet ontbreken. Sander, ik wil je bedanken voor de gezelligheid, de discussies en recepten. Ook af en toe een spelletje GERM mocht niet ontbreken. We bezochten samen ook de zomerschool in Erice en de ICL in Budapest. Tijdens ons verblijf in "de pijpenla" hadden we gezelschap van Gijsbert. Gijs, je gaf een nieuwe betekenis aan de woorden "kapot" en "eraan zijn" en je zorgde altijd voor een dosis humor op de kamer.

Als AIO heb ik vier studenten begeleid. Harald Verbraak was de eerste. Je hebt een aanzienlijke bijdrage geleverd aan het twee-foton onderzoek. Voor mij was alles toen nog even nieuw als voor jou en de door jou behaalde resultaten waren een goed startpunt voor verder onderzoek. Niet al het werk gedaan door Wouter "houdoe" Schrama is in dit proefschrift beland. Je was pionier op het gebied van de excited state absorptie metingen en ook het onderzoek beschreven in hoofdstuk 6 is grotendeels jouw werk. De erbiumloze erbiummonsters begrijp ik helaas nog steeds niet .... In het afgelopen jaar had ik de "luxe" van twee studenten. Paul Vermeulen, door mij Paul2 tot en met Paul974327302732 genoemd, ging verder met de excited state absorptie metingen. Samen hebben we zo'n beetje alle laserdyes voorbij zien komen en op de moeilijke momenten was Hermine Ribbers er met een voortreffelijke appeltaart.

Freek en Marieke wil ik bedanken voor de leuke tijd zowel op de vakgroep, de

Vletweide als in Erice, Budapest, Bern en andere mooie Zwitserse plaatsen. Ook bedankt voor de LaTeX hulp, zonder jullie had mijn proefschrift er nooit zo mooi uitgezien.

Veel collega's maakten de afgelopen jaren tot een mooie tijd, ieder op zijn eigen manier. Ik zou er een boek over kunnen schrijven, maar aan het eind van je proefschrift is die behoefte niet zo groot meer. Ik heb met sommigen bijzondere en persoonlijke dingen gedeeld, en ben ook blij dat ik bij hen af en toe mijn eigen ei kwijt kon. In de hoop dat ik niemand vergeet : Aarnoud, Ageeth, Alexander, Arjan (2x), Bert, Erik, Fiona, Floris, François, Harold, Jeroen, Jessica, Koert, Laura, Liesbeth, Marcel, Monica, Peter (2x), René, Rianne, Stephen, Thijs, Willem en Zeger.

De goede sfeer op de vakgroep kwam niet alleen van collega's, maar ook van de vele studenten. Gezien hun aantal en mijn geheugencapaciteit zal ik ze niet allemaal bij naam noemen.

Van de keren dat ik naar Hamburg ben geweest voor metingen bij het synchrotron ben ik de tel kwijtgeraakt. Vaak gingen er ook studenten mee en die boden dan goede tegenstand bij de andere deeltjesversneller die in de meethal was opgesteld. Daan, Karsten, Maurice, Moniek, Panos, en Roel: dankzij jullie was het mogelijk soms 24 uur per dag door te meten en de resultaten mogen er zijn! An exception to the 24 hours in a day is Vladimir Babin. Vladimir, you were always there to assist during the measurements, probably 25 hours a day. I would also like to thank Dr. Peter Gürtler for his assistance at the HIGITI setup.

De KNCV wil ik bedanken voor de bijdrage uit het Fellingafonds. Mede dankzij deze subsidie kon ik de reis naar de DPC–conferentie in Christchrch, Nieuw–Zeeland maken in 2003.

Naast wetenschap was er de afgelopen vier jaar gelukkig ook tijd voor dingen die niets met onderzoek doen te maken hebben.

Annemieke, leuk dat je een van mijn paranimfen wil zijn. Wat begon tijdens een werkcollege thermodynamica liep uiteindelijk uit op een verhuiswedstrijd. In Zeist werd ik jouw buurman, en dat garandeerde thee op loopafstand. Een paar jaar geleden verhuisde ik naar Bunnik, maar niet lang daarna jij ook, zodat we nu weer buren zijn. Iets verder weg, maar nog steeds loopafstand. Nu mijn proefschrift af is, kunnen we misschien eens gaan werken aan dat Telemann–concert ...

Vera en Sander wil ik bedanken voor de leuke dingen die we samen de afgelopen jaren hebben gedaan en beleefd. Nu Anne twee jaar is kan ze vast mee bowlen, dan eindig ik ook eens een keertje niet als laatste.

Elke dag schrijven aan je proefschrift is niet vol te houden zonder af en toe je gedachten eens flink te kunnen verzetten. Bij zeeverkennersgroep "de Argonauten" uit Rotterdam is altijd wat te doen en ik wil de verkennersleiding, en dan met name, Hans (en Joke), Edwin (en Monique), Tom en Martijn even noemen in dit dankwoord. Of het nu schuren,

schilderen of koken is, ik was altijd welkom en dat is een goed gevoel (en goed tegen de schrijf–stress). Jullie belangstelling voor de vorderingen van mijn proefschrift was ook een goede steun, en bij sommigen van jullie kon ik dan ook af en toe even mijn hart luchten.

Aad, bedankt voor de steun, de goede gesprekken, de glazen *goede* wijn en het verzetten van je vakantie. Je enthousiasme over Sri Lanka kan ik inmiddels met je delen, na een fantastische rondreis en een gezellig verbijf in villa “Nisaladya”.

Henksemama en Wil wil ik bedanken voor de belangstelling bij het tot stand komen van dit proefschrift. Misschien kunnen we van het eten bij de Japanner een traditie maken, maar de bloemkool met de niet te vegeten bal gehakt mag er ook zijn! Wil, bedankt voor de taxi–service, het heeft me een hoop treinleed bespaard!

Mijn ouders hebben mijn studie en promotieonderzoek altijd met belangstelling gevolgd, en stonden altijd voor me klaar. Papa en mama, ik hoop dat in ieder geval de samenvatting een beetje leesbaar geworden is. Bedankt voor al jullie steun en motivatie, en voor de “ziekenboeg”.

Als allerlaatste, maar wel de belangrijkste: Henk, jij bent de afgelopen twee jaar mijn maatje door dik en dun geweest. Door de schrijfdrukte zijn we dit jaar nog niet veel aan zeilen toegekomen, maar ooit maken we de tocht naar Noorwegen! Jij bent altijd in staat problemen te relativeren en daar heb ik de afgelopen tijd veel aan gehad. Vol goede moed kijk ik nu naar de toekomst die ons vast mooie dingen brengen zal.

Curriculum Vitae

De auteur van dit proefschrift werd geboren op 2 december 1976 te Ermelo. In 1995 behaalde hij zijn VWO diploma op de Regionale Scholengemeenschap het Slingerbos te Harderwijk. In september van datzelfde jaar begon hij met zijn studie Scheikunde aan de Universiteit Utrecht, waar hij in 1996 zijn propedeuse diploma behaalde (cum laude). Zijn afstudeeronderzoek werd uitgevoerd bij de sectie Gecondenseerde Materie. Het doctoraaldiploma werd in mei 2000 behaald (cum laude).

Op 1 juni 2000 begon Paul als AIO in de groep Chemie van de Gecondenseerde Materie van het Debye Instituut van de Universiteit Utrecht onder leiding van Prof. Meijerink. Hij verrichtte daar onderzoek naar de (vacuüm) ultraviolet niveaus van lanthanide ionen in kristallen. De resultaten van dat onderzoek staan beschreven in dit proefschrift en zijn gepubliceerd in een aantal wetenschappelijke artikelen. Ook bezocht hij de International Conference on Luminescence 2002 in Budapest en de International Conference on Dynamical Processes in Excited States of Solids 2003 in Christchurch, Nieuw–Zeeland.

Naast het verrichten van onderzoek vervulde hij diverse onderwijstaken, waaronder het begeleiden van studenten bij het eerstejaars synthese practicum en bij het onderdeel luminescentie van het practicum ‘Fysisch Chemisch Meten’. Verder begeleidde hij 16 VWO–scholieren met hun profielwerkstukken en vier studenten volgden onder zijn begeleiding een bij– of hoofdvak.

Afscheid

En een zoete slaap viel over zijn oogleden,
diep, zeer verkwikkend, het meest lijkend op de dood.
Het schip legde de weg makkelijk af,
omhoog steigerend, zoals een vierspan paarden in de vlakte,
tegelijk in beweging gezet door slagen van de zweep,
zo steigerde haar steven en achter haar
kolkten de purperen grote golven van de luid bruisende zee.
Zij snelde gestaag en zeer veilig voort en zelfs een valk,
snelste der roofvogels,
zou haar niet bij hebben kunnen houden.
Zo doorkliefde zij vlot de golven van de zee,
terwijl zij een man aan boord had, in schranderheid gelijk aan de goden,
die daarvoor zeer veel verdriet geleden had in zijn hart,
zowel oorlogen van mannen als smartelijke golven doorstaand,
maar die nu rustig sliep, vergetend al wat hij had geleden.

Homeros, Odyssee 13.79–92